CENTRO DE INVESTIGACIÓN Y DE ESTUDIOS AVANZADOS
DEL INSTITUTO POLITÉCNICO NACIONAL

UNIDAD MÉRIDA
DEPARTAMENTO DE FÍSICA APLICADA

Study of transport phenomena in liquid and solid composites loaded with micro-sized particles of carbonyl iron

Thesis presented by:

Ivan Yecid Forero Sandoval

To obtain the degree of

Doctor of Science

In the speciality of

Applied Physics

Thesis Directors

Dr. Juan José Alvarado Gil

Dr. José Edilberto Ordoñez Miranda

Mérida, Yucatán, México. August, 2019

CENTRO DE INVESTIGACIÓN Y DE ESTUDIOS AVANZADOS DEL INSTITUTO POLITÉCNICO NACIONAL

UNIDAD MÉRIDA

DEPARTAMENTO DE FÍSICA APLICADA

Estudio de los fenómenos de transporte en compuestos líquidos y sólidos cargados con partículas micrométricas de carbonil de hierro

Tesis que presenta:

Ivan Yecid Forero Sandoval

Para obtener el grado de

Doctor en Ciencias

en la especialidad de

Física Aplicada

Directores de Tesis:

Dr. Juan José Alvarado Gil

Dr. José Edilberto Ordoñez Miranda

Mérida, Yucatán, México. Agosto, 2019

Acknowledgements

Esta tesis no habría sido posible sin la disponibilidad, asesoría y apoyo de mis directores de tesis: Dr. Juan José Alvarado Gil y Dr. José Ordoñez Miranda (investigador del Centre National de la Recherche Scientifique (CNRS), en el instituto Pprime en Futuroscope, Francia.)

Al Consejo Nacional de Ciencia y Tecnología (CONACyT) por el apoyo económico otorgado durante mis estudios de maestría (No. de beca 348691) y doctorado (No. de beca 396706).

Al Fondo Conacyt-SENER de energía sustentable, financiados a través del Centro Mexicano para innovación en Energía Solar (207450), dentro de los proyectos estratégicos P-10 y P-18, así como a los proyectos del programa "Fronteras de la ciencia", proyecto 192 y ciencia básica and CB2015/251882.

A mis sinodales: Rubén Medina, Gabriel Pérez, Luis Diaz Ballote y Pascual Bartolo, quienes dedicaron parte de su valioso tiempo para brindarme las observaciones.

A Helena y Alicia por su cariño y apoyo incondicional, por estar conmigo en todo momento.

A mis padres y hermanos quienes con su amor y esfuerzo me han permitido cumplir esta etapa de mi vida. Gracias por inculcar en mi el ejemplo de esfuerzo.

A mis compañeros del laboratorio de espectroscopia óptica y térmica: Alex, Nelson, Caridad, Andrés, Lorena, Adriana, Fernando, Jorge y Daniel. Por haber contribuido

directa o indirectamente en el trabajo presentado en esta tesis. A Jose Bante, por su apoyo en la parte instrumental en los arreglos experimentales. A Dora Huerta, por dedicación en la obtención de imagenes SEM.

Al personal del taller: Gaspar Euan, Ricardo Correa, Ángel Chay y Nezahualcóyotl Aguirre, por su gran ayuda en el diseño y elaboración de elementos usados en los montajes experimentales.

Abstract

Composite materials are made of two or more constituent materials, in which each component have different physical or chemical properties. Using the adequate methodology of preparation the physical properties of these materials such as mechanical, electrical and thermal ones can be tuned in a wide range of values, which is the principal advantage compared traditional materials. These features have motivated many studies of their properties, especially about the interaction of the matrix and the particles. This work explores the thermal properties of liquid and solid composites and their relationship with mechanical and electrical properties, respectively.

The liquid composites are constituted by Silicone oil filled with carbonyl iron particles (CIP). Thermal properties are obtained using the technique known as thermal wave resonator. Additionally, measurements of viscosity were performed. The results show significant changes in thermal conductivity (k) and viscosity (η) when the content of carbonyl iron particles is increased. Interestingly, when a magnetic field is applied, these properties become larger. In particular, it was possible to find a direct relationship between the thermal conductivity and the dynamic viscosity, and we have shown that using high viscosity materials we can keep, for a long time, the order induced in the particles and therefore the increase in thermal conductivity.

In order to perform a complete thermal characterization of liquid composites a simple and novel methodology based on the front-face flash method was adapted to perform measurements of liquids. It was shown that a simple one dimensional approach, based on the Fourier's heat diffusion equation for a three layer system, can be used to determine the

thermal properties of the liquid. Measurements performed on several non-metallic liquids covering a wide range of thermal properties validate the method. Good agreement is found between the retrieved values of the thermal properties and previously reported values in literature. Moreover, measurements with the front-face configuration are less time consuming than using the classical (rear-face) flash method.

The solids are composed by polyester resin filled with carbonyl iron particles. Thermal properties are obtained using the front-face flash technique. Additionally, measurements of electrical conductivity (σ) were performed. The results show high changes in thermal and electrical conductivity when the content of carbonyl iron particles is increased, and the results for both (k) and (σ) exhibit a clear percolation threshold. A shift between the thermal and electrical threshold percolation around of 20% was found.

Resumen

Los materiales compuestos están hechos de dos o más materiales constituyentes, en los que cada componente tiene diferentes propiedades físicas o químicas. Utilizando la metodología adecuada de preparación, las propiedades físicas de estos materiales, así como las mecánicas, eléctricas y térmicas, pueden ajustarse en una amplia gama de valores, que es la principal ventaja en comparación con los materiales tradicionales. Estas características han motivado muchos estudios de sus propiedades, especialmente sobre la interacción de la matriz y las partículas. Este trabajo explora las propiedades térmicas de los compuestos líquidos y sólidos y su relación con las propiedades mecánicas y eléctricas, respectivamente.

Los materiales compuestos líquidos están formados por aceite de silicona con partículas de carbonil de hierro (CIP). Las propiedades térmicas se obtienen utilizando la técnica conocida como resonador de ondas térmicas. Adicionalmente, se realizaron mediciones de viscosidad. Los resultados muestran cambios significativos en la conductividad térmica (k) y la viscosidad (η) cuando aumenta el contenido de partículas de CIP. De manera singular, cuando se aplica un campo magnético, estas propiedades crecen aún más. En particular, fue posible encontrar una relación directa entre la conductividad térmica y la viscosidad dinámica y hemos demostrado que al usar materiales de alta viscosidad podemos mantener durante mucho tiempo, el orden inducido en las partículas y, por lo tanto, el aumento de la conductividad térmica.

Para realizar una caracterización térmica completa de materiales compuestos líquidos, se adaptó una metodología simple y novedosa basada en el método de flash frontal para realizar mediciones de líquidos. Se demostró que un enfoque unidimensional simple, basado

en la ecuación de difusión de calor de Fourier para un sistema de tres capas, puede utilizarse para determinar las propiedades térmicas del líquido. Las mediciones realizadas en varios líquidos no metálicos que cubren una amplia gama de propiedades térmicas validan el método. Los valores obtenidos de las propiedades térmicas concuerdan con los valores reportados previamente en la literatura. Además, las mediciones en la configuración frontal consumen menos tiempo que el método de flash clásico (cara posterior).

Los materiales compuestos sólidos están formados por resina de poliéster rellena con partículas de CIP. Las propiedades térmicas se obtienen utilizando la técnica de flash frontal. Adicionalmente, se realizaron mediciones de conductividad eléctrica (σ). Los resultados muestran grandes cambios en la conductividad térmica y eléctrica cuando aumenta el contenido de partículas de CIP, y los resultados de (k) y (σ) muestran un umbral de percolación. Se encontró un corrimiento de alrededor del 20 % entre el umbral de percolacion térmico y eléctrico.

Table of contents

List of figures

List of tables

Chapter 1

Introductory remarks

1.1 Aims and motivation of this thesis

A composite is a combination of two or more different materials (fillers and matrix) that results in better properties with respect to some desired characteristic than those of the individuals [1]. Humans have been creating composites for thousands of years to build everything from simple shelters to elaborate electronic devices [2]. During the last decades, a topic of great interest has been to adequately controlling the changes in the properties (mechanical, electrical, thermal, among others) of the composites and extend these results to predict which will be these changes on new materials.

Currently the fillers are wide varied: ceramic, carbon, metal and hybrid fillers [3, 4]. Most commonly used materials as matrices are polymers like polyethylene, polypropylene, epoxy resin, poly vinyl chloride, polyamide, high density polyethylene, polyoxymethylene and polyestirene [5]. Usual liquid matrices are mainly mineral oil, olefine polymer oil, water or glycol. In liquid composites, a surfactant is usually used in order to prevent agglomeration and sedimentation of the particles [6].

The liquid composites have been very attractive, especially those that present a response to external stimuli. For example, magnetorheological fluids (MR) are characterized by reversible changes in viscosity, elastic limit, electrical and thermal conductivity, under the

interaction with an external magnetic field [7]. The first reported MR fluid was designed by Rabinow in 1948 by dispersing iron particles in engine oil, extending the study to the design of a magnetic clutch [8].

This has allowed a great variety of material combinations, which have become the basis for a large variety of industrial applications such as circuit breakers, motor controlers, dampers, and high voltage insulators. The use of these materials for the design of systems for energy management has taken great value, due to the possibility of reducing costs and increasing efficiency. This situation requires the use of appropriate techniques for the characterization of new materials, for possible industrial application, in which non-destructive techniques have great relevance.

In general, the composite properties (mechanical, thermal, electrical, among others) involve complex phenomena that depends on many factors, such as the properties of the matrix and the fillers, their concentration, distribution, orientation, size, and shape [9]. This has allowed a great variety of material combinations, producing a wide range of industrial applications, e.g. liquids composites are used in automobile suspensions, brakes and clutches, seismic vibration control in structures [10], precision polishing [11] and control of thermal energy transfer [12–15]. Solid composites have great relevance in the development of compact electronic devices [16], conducting adhesives [17], anti-static materials [18], electromagnetic shielding [19, 20], among others [3, 21, 22]

The reported investigations have not yet fully explored all the possible relationships between different physical properties, there being some composites in which the characterization has been incomplete or the techniques have not been really adequate. Thus, the main objective of this thesis is the non-destructive thermal characterization of solid and liquid composites composed of carbonyl-iron particles, establishing relationships with mechanical or electrical properties, using photothermal techniques.

1.2 Overview of the individual chapters

This thesis is organized into four main chapters. To avoid excessive redundancy, lengthy information that is required in a later chapter of the thesis was occasionally referred to an earlier chapter or in the case of mathematical details to the appendix.

Chapter 2 presents in the first part a brief summary of the mechanisms of heat transfer and some concepts that are used in the following chapters. In the second part, the theoretical foundations of the emission of thermal radiation by matter are presented, the characteristics of a thermography system are addressed and the most used techniques are presented.

In chapter 3, the thermal conductivity and the viscosity of magnetorheological fluids composed by carbonyl iron particles in silicon oil are studied as a function of the concentration and magnetic field strength. The thermal properties were obtained by means of the thermal wave resonator and the viscosity by means of a commercial viscometer. It was shown that both the thermal conductivity and the viscosity rises with the increase in the amount of particles and the intensity of the field. Finally, the relationship between thermal conductivity and viscosity is studied through an analytical relationship. This chapter is based on the article: *Study of thermal conductivity of magnetorheological fluids using the thermal-wave resonant cavity and its relationship with the viscosity. Forero-Sandoval, I. Y., Vega-Flick, A., Alvarado-Gil, J. J., and Medina-Esquivel, R. A. (2016). Smart Materials and Structures, 26(2), 025010.*

Chapter 4 presents the adaptation of the flash front-face method for the simultaneous measurement of thermal diffusivity and thermal effusivity in liquids. The model and theoretical analysis of the evolution of temperature is presented. Limitations are explored through a sensitivity analysis. The method is validated with common liquids and is applied to study a MR fluid. This chapter is based on the article: *Measurement of the thermal transport properties of liquids using the front-face flash method. Forero-Sandoval, I. Y., Pech-May, N. W., and Alvarado-Gil, J. J. (2018). Infrared Physics and Technology, 93, 9-15.*

In chapter 5 the thermal and electrical conductivity in composites made up of carbonyl iron microparticles randomly distributed in a polyester resin matrix are studied. Thermal

diffusivity and thermal effusivity of these composites was measured by means of the laser flash method, and the thermal conductivity and volumetric heat capacity of the composites are determined from the two measured properties. The DC electrical conductivity was also measured using a simple method. The thermal and electrical conductivity show a clear percolation threshold and the shift between both thresholds is 20%. This chapter is based on the article: *Percolation threshold shift between thermal and electric conductivities of carbonyl-iron composites. Forero-Sandoval, I. Y., Cervantez-Alvarez, F., Ramirez-Rincon, J. A., Macias, J. D., Pech-May, N. W., Ordonez-Miranda J. E., and Alvarado-Gil, J. J.*, submitted to Journal of Physics D.

Chapter 2

General aspects

In this chapter, the general concepts used in this thesis are presented. In the first part, the mechanisms of heat transfer are established; In the second part, the basic concepts of heat transport are discussed and in the last part generalities on infrared thermography are presented, which is one of the main techniques used in this thesis for performing thermal characterization.

2.1 Heat transfer mechanisms

As a result of a temperature gradient in a medium or between two bodies, heat transfer occurs. The heat transfer is given by three mechanisms: conduction, convection, and radiation [23]. The thermal energy transfer by **conduction** may be viewed as the transport of energy from the more energetic to the less energetic particles of a substance due to interactions between them [24]. In liquids and gases, the neighboring molecules collide, as they are constantly doing, and therefore the transfer of energy from the more energetic to the less energetic molecules occur. The difference between liquids and gases is that in liquids the molecules are more closely spaced and the molecular interactions are stronger and more frequent. Similarly, in a solid, conduction may be attributed to atomic activity in the form of lattice vibrations as well as by the transfer of electrons. The heat transfer by conduction can be expressed

by the Fourier law, which indicates that the rate of heat transfer per unit area in a certain direction q_{cd} ($\mathrm{Wm^{-2}}$) is proportional to the temperature gradient in that direction; in one dimension it is expressed as [25]:

$$q_{cd} = -k\frac{\partial T}{\partial x}. \tag{2.1}$$

The proportionality constant k ($\mathrm{Wm^{-1}K^{-1}}$), is called thermal conductivity, which is characteristic of each material and describes the transport of energy in the form of heat through a body as a result of a temperature gradient. The minus sign indicates that the heat transfer occurs in the direction in which the temperature decreases.

The thermal energy transfer by **convection** (q_{cv}) is the consequence of a superposition of the random molecular movement (diffusion) and the macroscopic motion of the fluid in thermal contact with a hot surface [26]. The contribution due to random molecular motion (diffusion) dominates near the surface where the fluid velocity is low. The heat transfer by convection is proportional to the difference between the surface and fluid temperatures, T_s and T_f, respectively, and can be quantified by means of Newton's law of cooling, expressed as [25]:

$$q_{cv} = h(T_s - T_f). \tag{2.2}$$

where the parameter h ($\mathrm{Wm^{-2}K^{-1}}$) is known as the convection heat transfer coefficient. It depends on conditions in the boundary layer, which are influenced by surface geometry, the nature of the fluid motion (laminar, turbulent, etc), and an assortment of fluid thermodynamic and transport properties.

Finally the heat transfer by **radiation** (q_{rd}) is due to the emission of electromagnetic waves generated by the thermal movement of charged particles in matter [27]. It occurs when the matter is at a temperature other than absolute zero and unlike the two previous mechanisms does not require means to propagate. The expression that provides the difference between thermal energy that is released due to radiation emission and that which is gained due to radiation absorption is [28]:

$$q_{rd} = \varepsilon\sigma(T_s^4 - T_{env}^4), \tag{2.3}$$

where T_s is the surface temperature, T_{env} is the temperature of the surrounding environment, ε is known as emissivity and $\sigma = 5.67 \times 10^{-8}$ ($\mathrm{Wm^{-2}K^{-4}}$) is the Stefan-Boltzmann constant.

2.2 Heat diffusion equation

On the thermal characterization of materials, the basic tool is the heat equation. It represents the distribution of heat (or variation in temperature) in a particular body, over time [29]. Once this distribution is known, it is possible that the quantities of interest, such as thermal diffusivity or thermal conductivity, can be determined. The heat transport equation for a solid with heat generation within the body is given by [23]:

$$k\nabla^2 T + \dot{g} = \rho c_p \frac{\partial T}{\partial t}, \tag{2.4}$$

where $\dot{g}$ ($\mathrm{Wm^{-3}}$) is the rate at which heat is generated per unit volume of the medium, ρ ($\mathrm{kgm^{-3}}$) is the density and c_p ($\mathrm{Jkg^{-1}K^{-1}}$) the specific heat. From equation 2.4 we can highlight four special cases [25]:

(i) If we assume that the thermal conductivity of a material is isotropic, we obtain,

$$\nabla^2 T + \frac{\dot{g}}{k} = \frac{1}{\alpha}\frac{\partial T}{\partial t} \tag{2.5}$$

where $\alpha = k/\rho c$ is known as the thermal diffusivity ($\mathrm{m^2s^{-1}}$).

(ii) For a medium with constant thermal conductivity and without internal heat generation, we obtain the Fourier diffusion equation for homogeneous systems:

$$\nabla^2 T = \frac{1}{\alpha}\frac{\partial T}{\partial t} \tag{2.6}$$

(iii) For steady-state conditions, since there cannot be any change in the amount of energy storage, we obtain the Poisson equation:

$$\nabla^2 T + \frac{\dot{g}}{k} = 0 \tag{2.7}$$

(iv) For steady-state conditions, with no energy generation, we obtain the Laplace equation:

$$\nabla^2 T = 0 \tag{2.8}$$

2.2.1 Thermal conductivity

Thermal conductivity (k) controls the rate of heat flux in a medium [23]. It is high in metals (thermal conductors) and in general in continuous bodies, it is low in polymers, and very low in some special materials such as fiberglass (thermal insulators). For thermal conduction there is a need for a medium, hence it is null in the ideal vacuum, and very low in environments with a low vacuum [30].

2.2.2 Thermal diffusivity

Thermal diffusivity (α) tells us how fast the thermal energy is distributed by the material, it can be increased with the ability to conduct the heat and can be decreased with the amount of thermal energy that is needed to increase the temperature [30]. High values of thermal diffusivity generate rapid responses to changes in the thermal conditions, that is, this amount indicates the time scale in which heat transfer occurs in the materials [23].

2.2.3 Thermal effusivity

The thermal effusivity (ϵ), referred to as the thermal inertia, is defined as the square root of the product of the thermal conductivity and the volumetric heat capacity $\epsilon = \sqrt{k\rho C}$. The thermal effusivity tells us how much the temperature of an object changes with respect to an input of thermal energy. On the other hand, the thermal effusivity (for two materials on

thermal contact with ϵ_1 and ϵ_2) characterizes the thermal behavior by means of the thermal contrast factor Γ [30]:

$$\Gamma = \frac{\epsilon_1 - \epsilon_2}{\epsilon_1 + \epsilon_2}. \tag{2.9}$$

In the case of equal effusivities $\Gamma = 0$, there is no thermal mismatch, for this reason, the interface between the two materials cannot be detected by means of a measurement in the surface temperature.

2.2.4 Thermal diffusion length

By assuming a harmonic heating (equation A.1) the solution of the Fourier equation (equation 2.6) gives us a field of harmonic temperatures with the same frequency f of warming but with different amplitude and phase. The main characteristic is the strong fall of the amplitude with the penetration in the object. This decay is known as thermal diffusion length [25], given by:

$$\mu = \sqrt{\frac{\alpha}{\pi f}}. \tag{2.10}$$

The dependence of the thermal diffusion length with the frequency tell us that at low frequencies the thermal waves can penetrate deeper into a material than at higher frequencies. On the other hand, the penetration of the thermal wave also increases with the thermal diffusivity.

2.3 Infrared thermography

Infrared thermography (IRT) is a non-destructive technique that allows the visualization of heat patterns of an object both spatially and in time by means of an infrared sensor such as a thermal camera [31]. In this section, the principal aspects of infrared thermography are presented. The first part discusses the thermal emission by the matter; the second part the basis of an infrared system and finally the most popular methods in active thermography.

2.3.1 Thermal emission by matter: Planck's law

Every object at a temperature above 0 K emits thermal radiation, whose intensity depends on the wavelength λ and the temperature T [32]. Thermal radiation occurs in a range of the electromagnetic spectrum of energy emission. Accordingly, it exhibits the same wave-like properties as light or radio waves [30]. The full electromagnetic spectrum includes an enormous range of energy-bearing waves, of which heat is only a small part (see table 2.1).

Characterization	Wavelength λ	
Cosmic rays	<0.3 pm	
Gamma rays	0.3-100 pm	
X rays	0.01-30 nm	
Ultraviolet light	30-400 nm	Thermal Radiation 0.1-1000 μm
Visible light	0.4-0.7 μm	
Near infrared radiation	0.7-30 μm	
Far infrared radiation	30-1000 μm	
Millimeter waves	1-10 mm	
Microwaves	10-300 mm	
Shortwave radio TV	300 mm-100 m	
Longwave radio	100 m-30 km	

Table 2.1: Forms of the electromagnetic wave spectrum.

Thermal radiation emitted by solids is generally approached through the concept of black body. This concept represents an object perfectly capable of absorbing and emitting radiation and has the following three characteristics [30]:

1) A blackbody absorbs all incident radiation, regardless of wavelength or direction.

2) For any given temperature and wavelength value, no surface can emit more energy than a black body.

3) The radiation emitted by a black body depends on the wavelength, however this radi-

ance does not depend on the direction, that is, it behaves like a Lambertian radiator.

The emission of radiation by a black body is described by Planck's law, which is based on concepts of statistical thermodynamics, but with the quantum nature of the emission and absorption of the radiation taken into account, and is given by [33],

$$\frac{dR_{bb}(\lambda,T)}{d\lambda} = \frac{2\pi hc^2\lambda^{-5}}{\exp(hc/\lambda k_B T) - 1}. \tag{2.11}$$

Where $dR_{bb}(\lambda,T)/d\lambda$ is the power emitted per unit area per unit wavelength, which is called the spectral emittance (Wm^{-3}), $h = 6.625 \times 10^{-34}$ Js is the Planck constant, $k_B = 1.380 \times 10^{-23}$ JK^{-1} is the Boltzman constant, $c = 2.998 \times 10^{8}$ ms^{-1} is the speed of light and T(K) is the absolute temperature of the black body given in Kelvin.

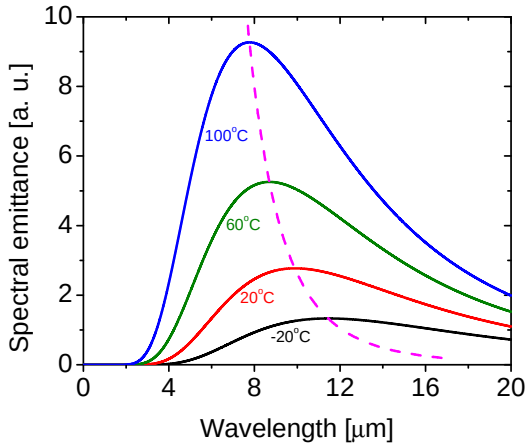

Figure 2.1: Spectral emittance $dR_{bb}(\lambda,T)/d\lambda$ of a black body according to Planck's law (equation 2.11). The continuous lines represent different temperatures and the dashed line shows the maximum emission.

Figure 2.1 shows a series of blackbody spectra as a function of the wavelength for different temperatures. The black line represents the spectral emittance for $-20\,^{\circ}\mathrm{C}$, the red line for $20\,^{\circ}\mathrm{C}$, the green line for $60\,^{\circ}\mathrm{C}$ and the blue line for $100\,^{\circ}\mathrm{C}$. Note that the spectrum is continuous unlike the spectral lamps, for a given wavelength the emittance increases with the temperature and also the region of emission depends on the temperature: at low temperatures the emission occurs in regions of long wavelength and for high temperatures in regions of

short wavelengths. The dashed magenta line represents the peaks of maximum emission as a function of the wavelength, which are obtained by means of Wien's displacement law: $\lambda_{max}\, T = 2897.8\,\mu\text{mK}$ [34].

2.3.2 Emissivity

One of the main characteristics that affects the amount of energy radiated in stationary thermal conditions is emissivity. For a black body at a fixed temperature, it is possible to determine the spectral emittance by means of Planck's law, but under real conditions Planck's law can only estimate the maximum flow. The spectral exitance of a surface can be related to the spectral exitance of a blackbody ($dR_{bb}/d\lambda$) by means of the spectral emissivity [32].

$$\frac{dR(\lambda, T)}{d\lambda} = \varepsilon(\lambda)\frac{dR_{bb}(\lambda, T)}{d\lambda} \tag{2.12}$$

In general, the spectral emissivity varies very little with the wavelength for solid objects, this favorably affects the most practical applications of thermography. However, in the case of liquids and gases, it fluctuates rapidly, due to the absorption and emission bands in the infrared range. Although the emissivity is a feature that depends on the intrinsic properties of each material: type of material (metal, insulator, etc) [30], surface structure (rough, bright) [35, 36] and geometry (grooves, cavity, etc) [37, 38], there are variations due to other parameters: angle of observation [39–41], wavelength and temperature [24, 42].

2.3.3 Infrared detectors

Infrared thermography basically includes a camera, equipped with a series of changeable optics and a computer. For some applications a external stimulus is required in order to produce a thermal contrast (flash lamps, lasers, etc). The core of the camera is the infrared detector, which absorbs the IR energy emitted by the object (whose surface temperature is measured) and converts it into electrical voltage or current. Infrared (IR) radiation was discovered in 1800 by Sir William Herschel. In his experiments, he dispersed solar radiation by means of a prism and located thermometers with blackened bulbs throughout the spectrum.

He found that the temperature measured by the thermometers was higher in those regions of the spectrum which that were not illuminated by visible light and positioned after the red line. These experiments proved that solar radiation is composed of other forms of radiation outside the visible range and found that one form of detection is through of a heating effect [43, 44].

The first step in the development of detectors more sensitive to infrared radiation was given with the discovery of the Seebeck effect in 1821 [45]. This consists in the observation of a small electric current in a closed circuit of two different metallic conductors, when their junctions are maintained at different temperatures. In order to increase sensitivity, arrangements of thermocouples called thermopile have been built. Nobili made the first thermocouple and improved the electric thermometer based on the thermoelectric effect in 1829 and the first thermopile was designed by Melloni in 1834 [46].

The period between World Wars I and II was marked by the development of photon detectors. The detection process on the photoconducting or photovoltaic detectors are based on the direct conversion of radiation into an electrical signal and have much shorter response times and higher sensitivities [32]. Between 1930 and 1944 lead sulfide (PbS) detectors were developed, specifically for military needs. These detectors were sensitive in the 1.3-3 μm band. Then the spectral range was extended to mid infrared, i.e., 3-5 μm between 1940 and 1950 by the use of indium antimonide (InSb). Finally, the mercury-tellurium-cadmium detectors (HgTeCd) made posible the exploration of the far infrared, 8-14 μm, by the 1960's. These sensitivity ranges have been extended due to doping techniques and at different cooling temperatures [47].

The invention of charge coupled devices (CCDs) in 1969 was the first step to obtain thermal images [48]. In 1975 the first CCD TV camera was developed and this allowed in the 1990's, with the birth of IR detectors, to build a large 2D arrays with the number of pixels up to many hundreds of thousands, thanks to hybrid integration of HgCdTe bidimensional arrays in silicon substrate with CCD devices. In general, radiation detectors are characterized by a large number of parameters [49]. Figures of merit allowing the characterization of the detectors and their comparison with others are described.

The **responsivity** [V/W] of an IR detector is defined as the ratio of the detector signal voltage or current to the incident monochromatic radiant flux on the detector area at wavelength λ. The **noise equivalent power** (NEP) [$V/Hz^{1/2}$] gives the lower limit of the detectable radiant power difference. In other words, this is the quantity of incident light when the signal to noise ratio is 1 [50].

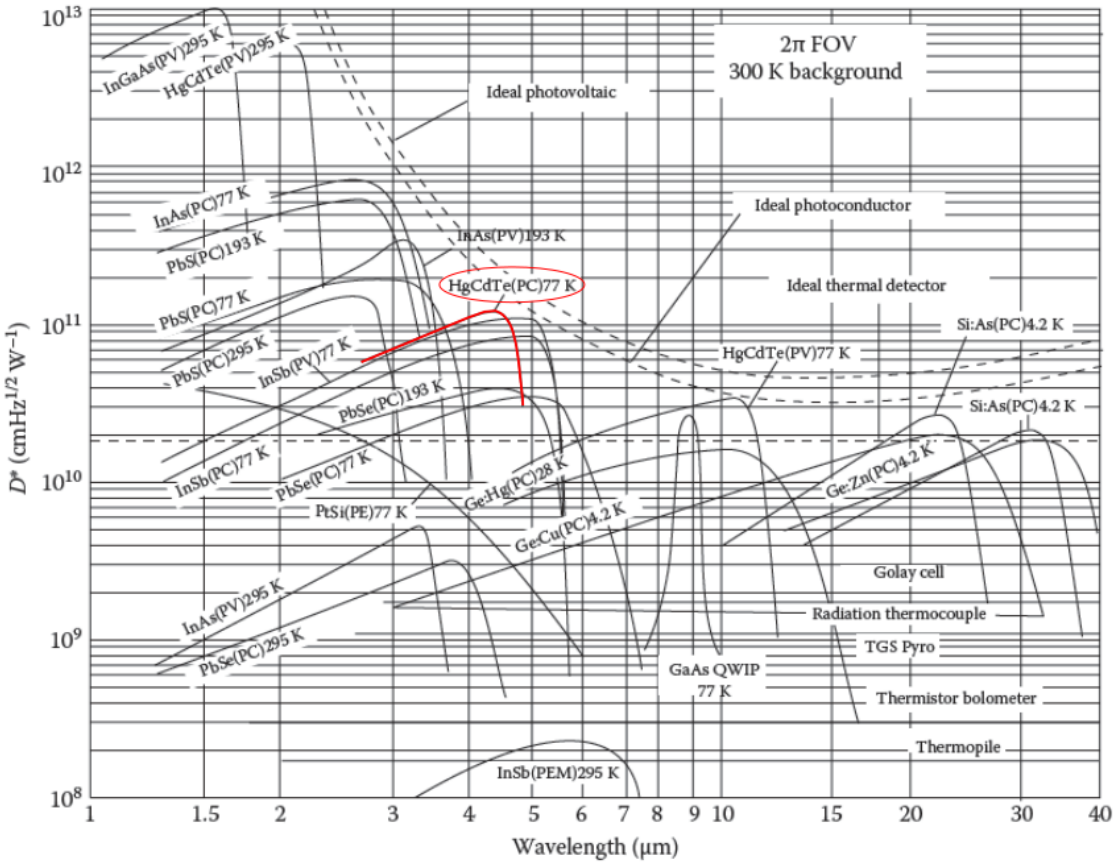

Figure 2.2: Comparison of the D* of various available detectors when operated at the indicated temperature. Theoretical curves for D* (dashed lines) for ideal photovoltaic and photoconductive detectors and thermal detectors are also shown. The red line shows the detectivity of the sensor used on the experimental part. Adapted from Rogalski (2000)

Finally, the main characteristic of infrared detectors is the **normalized detectivity** denoted D* (Levinstein 1965). This quantity is defined as the signal to noise ratio (SNR) per watt of incident power and is normalized both for an 1 cm^2 detector sensitive surface and 1

Hz bandwidth [51]. Figure 2.2 shows the sensitivity ranges of a wide variety of detectors and their corresponding cooling temperature.

2.3.4 Atmospheric transmissivity

The energy detected depends not only on the emissivity coefficient of the surface under measurement but also on the environment. In fact, a fraction of this energy may be absorbed by the atmosphere between the object and the camera. If there is any absorption of thermal radiation by the air, this causes errors in thermographic measurements [33, 34]. In order to keep these errors small, the wavelength range of a thermal camera has to be chosen so to avoid the dominant absorption regions. Figure 2.3 shows the transmission of a typical wet atmosphere as a function of the wavelength.

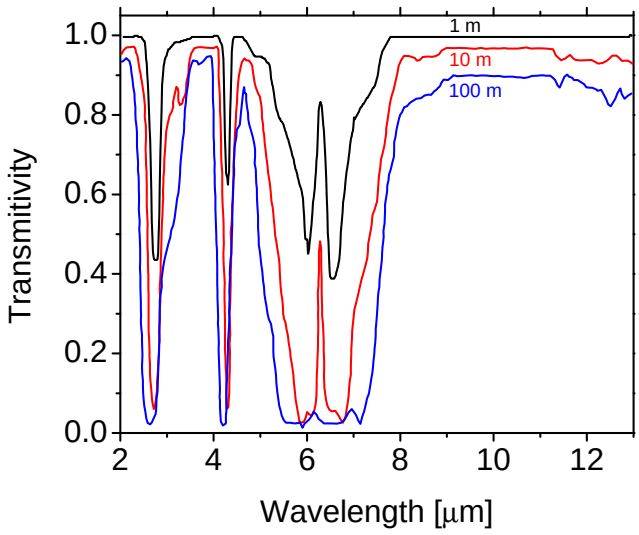

Figure 2.3: Atmospheric transmissivity for different values of camera-to-object distance. The blue line represents the transmittance at 100 m, the black line represents the transmittance at 10 m and the red line represents the transmittance at 1 m. Adapted from Minkina (2009).

Most of the infrared commercial systems match the atmospheric transmission windows and operate in bands between 3 and 5 μm, often called short wavelength (SW) band or between 8 and 12 μm, often called long wavelength (LW). In the other hand, the region of

the near infrared (0.8 to 1.1 μm) is easily covered by standard ambient operation temperature silicon detectors [52, 53].

2.3.5 Important camera characteristics

Parameters such as thermal response, detector and electronic noise, geometric resolution, accuracy, spectral detectivity, frame rate and integration time characterize the performance of an infrared system [30, 54]. Below we will discuss in more detail its meaning and influence in practical applications.

Temperature accuracy gives the absolute value of the temperature measurement error for a blackbody temperature measurements. For most cameras, the absolute temperature accuracy is specified to be 2 K or 2% of the temperature measured [30].

Temperature resolution is given by the NETD (Noise equivalent temperature difference), which represents the difference of temperature, at two points of the image, which corresponds to a signal equal to the background noise of the camera. Some new FPA systems are able to detect temperature differences of less than 20 mK at ambient temperature [54].

Spatial resolution is given by IFOV (Instantaneous field of view) and SRF (Slit response function). The IFOV represents the capability of a system to measure the surface temperature of small objects, and is generally defined as the angle over which one detector element of the focal plane array senses the object radiation. The SRF represents the diffraction of the optics, is defined as a dependence of the system response to a slit size object with a variable slit width [34].

Time resolution is given by frame rate and integration time. The first one describes how many thermal images per second the IR camera can collect. The second is referred to the amount of time necessary to capture a single thermal image, which is similar to shutter speed on a traditional visible light camera. Shorter integration times allows faster frame rates [34].

2.3.6 Thermal imaging methods

Due to the radiation detected by the thermal camera comes from the object and the environment, it is necessary that there be a temperature difference between the object and the environment so that the temperature patterns of the object are different from those of the background [55]. The case in which the objects or structures to be studied naturally have a temperature different from the background is known as passive thermography, for example, the human body is easily detectable without additional stimulation. The case in which an external stimulus is necessary to produce a thermal contrast on the surface of the object to be analyzed is called active thermography, for example, an object with imperfections such as fractures or holes require a thermal imbalance to produce detectable thermal patterns by the thermal camera [31].

The active and passive methods are complemented with different elements which depend on the main objective of the analysis. These elements take into account factors such as: if the camera or the object is moving, if the area that is stimulated is the same as the one of the acquisition of data, the region of the object from which the signal is to be acquired, the type of energy used to heat and the way in which the energy is delivered to the object [51]. These elements are shown in figure 2.4 and explained below:

Configurations: Camera, object and source for heating are the three fundamental elements in an experimental arrangement. In the case that these three elements are fixed, it is said that we have a *static configuration*; if any of them is in motion, we talk about *dynamic configuration* [56, 57].

Modes: There are three inspection modes which depend on the way in which the energy delivered to the object with respect to the location of the camera. In the *reflection mode* (front-face), the energy is delivered to the object on the same side in which data is collected. In the *transmission mode* (rear-face), the energy is delivered to the object on one side and the experimental data is collected on the opposite side. In the *internal mode*, the heating is generated internally and the data is acquired on any face of the

object [51].

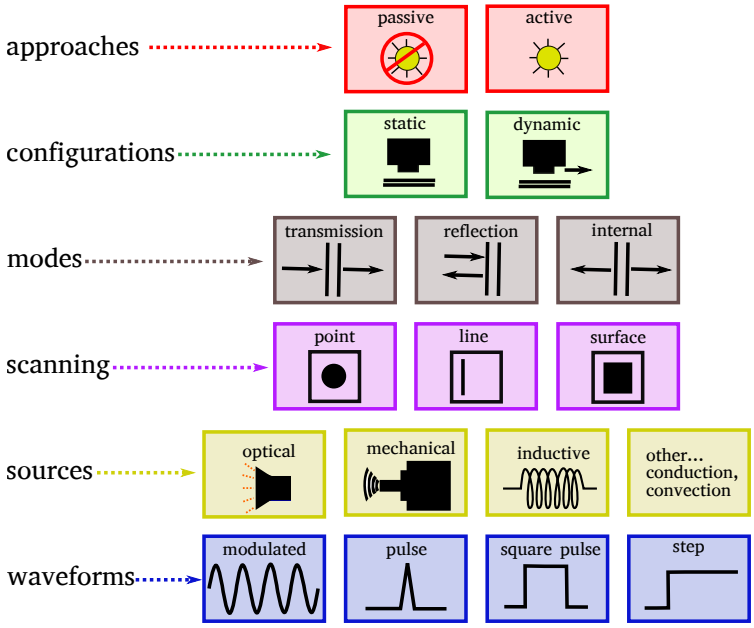

Figure 2.4: Thermography inspection scenarios: diagram of different elements to take into account in a experimental design.

Scanning: The transferred energy allows one to scan the surface in three different ways: point, line and surface. In *point scanning*, only one point of the surface of the object is heated each time. In *linear scanning*, the region that is heated is a vertical or horizontal line of the entire surface to be inspected. In *surface scanning*, the entire surface of the object is heated simultaneously [51].

Sources: In order to produce a thermal contrast between the object and the background and/or generate a transient of temperature is necessary to heat or cool the object. Due to the advantages of the control, a heat source is preferred. Generally, they are: optical, mechanical, inductive or conductive [31]. In the type of *optical* heating, sources are usually lasers, photographic flash or IR lamps. As for the *mechanical* sources, the most common are acoustic waves or ultrasound. *Inductive* sources use Eddy currents [58, 59] and in some applications, thermal blankets are usually used as *conduction* sources.

Waveforms: The last element refers basically to the time in which the object of study is heated, that is if the source delivers heat periodically or a pulse for a few seconds or minutes. In the case of *modulated* heating, thermal waves whose frequency is optimized taking into account the thermal properties of the object are used [60,61]. When energy delivered is given in the order of milliseconds, it is known as *pulsed*. When the heating is for a few seconds, it is known as *step* and if the heating is for a few seconds to minutes, is called a *square pulse* [62,63].

2.3.7 Pulsed thermography

One of the most popular methods in active thermography is pulsed thermography (PT) [62]. The surface of the sample is heated by means of a pulsed laser beam or a flash lamp. The thermograms are collected and analyzed to study the evolution of surface temperature during the heating or cooling process. Figure 2.5 shows a typical pulsed thermography set-up. If the sample under study is completely homogeneous, that is, it has no defects, the changes in temperature will also be homogeneous. In the case of defects such as holes, embedded particles or delaminations, regions will appear in which high-temperatures will be observed compared to their environment due to the isolation effect. The location, shape, and size of these defects can be estimated by means of the temperature distribution on the surface of the sample [64]. The PT technique is affected by local variation of the emissivity coefficient and non-uniform heating that can mask the defect visibility. The emissivity problem may be overcome by painting the surface, but this could be a solution only for parts where this surface finish is adequate.

The pulsed technique was proposed by Parker in 1961 [62]. The analytical model had many simplifications regarding the sample: uniform, homogeneous and opaque; and to the conditions of the experiment: adiabatic conditions, homogeneous heating and infinitely short heating time, which although were difficult to put into practice. However, gradually more appropriate considerations are included for the theoretical models, and experimental systems that were being developed with the objective of obtaining more reliable results being ap-

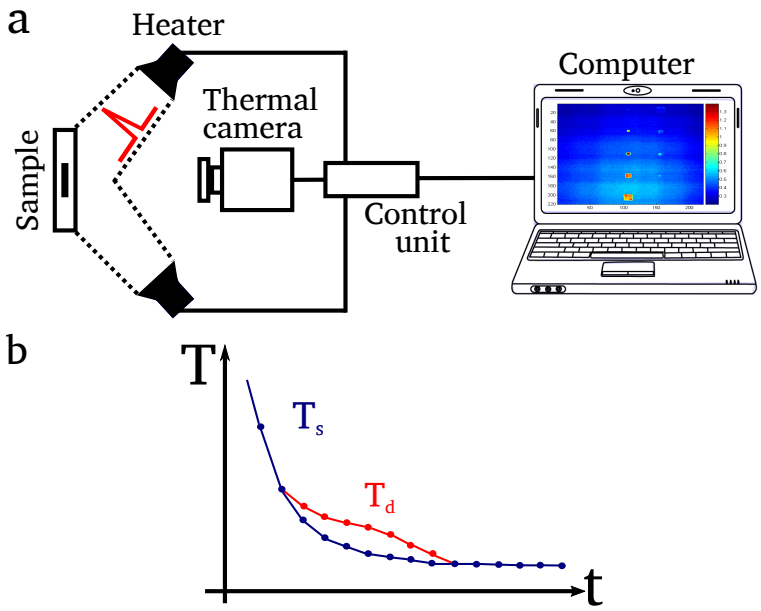

Figure 2.5: a) Typical pulsed thermography front-face configuration. b) Temperature evolution. The temperature profile for a defective (red line) and non-defective (blue line) samples are showed.

plicable to a great variety of materials [65]. Then the effects of radiation [66], finite pulse duration [63], non-uniform heating [67,68], the transparency effect of the sample [69] and non-linearity effects of the detectors [70], among others, have been studied and included. These advances have allowed the thermal characterization of a great variety of materials with different characteristics: semitransparent [69], anisotropic [71], multilayered materials [72], thin films [73], composite materials [74] and materials with a dependence of the thermophysical properties with temperature [75].

2.3.8 Modulated thermography or lock-in thermography

The experimental arrangement is very similar to that of pulsed thermography, in this case the thermal excitation pulse is replaced by a sinusoidal source of thermal energy [60, 61]. The source of heating send periodic waves at a given modulation frequency, ideally until a steady state is achieved. This harmonic heating produces a harmonic variation at the surface temperature of the object, which generates harmonic variations of temperature inside the material at certain depth. Figure 2.6 shows a typical lock-in thermography set-up. Inside of

the material the amplitude is strongly attenuated as a function of the depth, as described by the length of thermal diffusion. The length of thermal diffusion depends on the thermal diffusivity and the frequency of the thermal wave, as it will be shown in the section 2.2.4. An important aspect is the fact that at low frequencies the thermal waves can penetrate deeper into the material than at high frequencies, or something that also happens increasing its thermal diffusivity. The use of sinusoidal heating has the advantage that the frequency and the shape of the response are preserved, only the amplitude and phase delay of the wave may change.

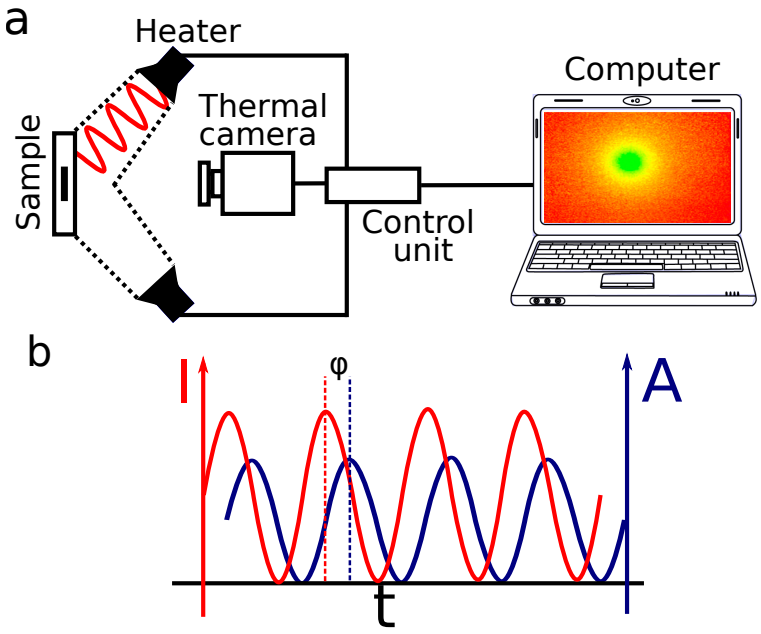

Figure 2.6: Experimental set-up for lock-in thermography

The basic idea of using modulated heat was first used by Angstrom in 1863. In his experiment, thermal waves were generated by means of a mechanical contact with a water flow. The basic concept of modulated temography or lock-in was described by Carlomagno and Berardi (1976) [76] and then investigated by Beaudoin *et al.* (1985) [77], Kuo *et al.* (1987) [78] and Busse *et al.* (1992) [79].

Chapter 3

Magnetorheological fluids: thermal conductivity and its relationship with the viscosity

In this chapter, the thermal conductivity and viscosity of a magnetorheological suspension composed of carbonyl iron particles dispersed in silicone oil were studied. Thermal wave resonant cavity was employed to measure the thermal diffusivity of the magnetorheological fluid as a function of an externally applied magnetic field. The dynamic viscosity was also measured and its relationship with the concentration of the particles and the magnetic field strength was investigated. The relationship between thermal conductivity and the dynamic viscosity was explored. Our measurements were examined using an analytical relation between the thermal conductivity and the dynamic viscosity.

3.1 Introduction

A smart fluid is a suspension of micrometer-sized particles in a dielectric carrier liquid in which changes on their properties (thermal, mechanical, electrical) can be tuned by means of an external or internal stimulus (Magnetic and electric fields, stress, strain, light) and this

changes can be revered by removing the external stimulus [7, 80, 81]. In particular, it is well established that Magnetorheological (MR) materials can change their physical properties by applying an external magnetic field. The field induces ordering and/or agglomeration of the magnetic microparticles in the fluid, leading to significant changes in the mechanical, rheological, thermal, optical and electrical properties [8]. A variety of industrial and scientific applications [82] have been developed that take advantage of MR properties, such as automobile suspensions, brakes and clutches, seismic vibration control in structures [10], precision polishing [11] and control of thermal energy transfer [12–15] among many others.

MR materials were discovered in 1948 by Jacob Rabinow [8] and in 1949 the first studies of MR and electrorheological materials were made by W. M. Winslow [83]; he found that the viscosity has a square dependence with the applied field and that a possible reason for the observed phenomena is the formation of chain-like structures due to the interaction of the magnetic particles with the magnetic field lines [84]. It has also been found that the viscosity depends on the size of the particles, the suspension concentration, the magnetic properties of the microparticles and, the characteristics of the applied magnetic field [85]. In a similar way, the dependence of the thermal conductivity of MR suspensions on the applied magnetic field is related to the formation of particle chains. Due to this, MR fluids are ideal systems to explore the relationship between viscosity and thermal conductivity, which has been observed in nanofluids, carbon nanotubes dispersions, and photopolymerizing resins [86–90]. The central idea of these studies is to show the importance of finding the ideal conditions for the thermal conductivity and viscosity for the development of practical heat transfer fluids using fillers, in order to fulfill the needs of specific applications.

Different theoretical schemes have been devised to understand the relationship between the externally applied magnetic field and the formation of particle chains in the MR suspension [91, 92]. This leads to a functional dependence of both the thermal conductivity and viscosity on the applied magnetic field [93, 94].

In the present work we study heat transfer and rheology for high viscosity MR fluids. The fluids are formed by carbonyl iron microparticles in silicone oil. The dependence of the

thermal conductivity and viscosity is studied as a function of the microparticles concentration and the intensity of the applied magnetic field. It is shown that the application of a magnetic field induces a considerable increment of the thermal conductivity of the MR fluids.

The relationship between the viscosity and the thermal conductivity is explored using a simple theoretical analytical approach, which shows that the increase of viscosity is related to the growth of the thermal conductivity. Additionally the response of the MR fluid to successive on/off cycles of the magnetic field is studied, which shows that the changes in heat transfer induced by the magnetic field, remain even after the field is turned off for a considerable large time interval.

3.2 Experimental setup

3.2.1 Samples:

The MR suspensions were prepared using silicone oil as nonmagnetic matrix and carbonyl iron powder (CIP) as the magnetic filler particles. The MR fluid was divided into groups of 5, 10, 15 and 20 vol % of CIP. A representative histogram of size distribution of CIP is presented in figure 3.1. Note that the particles exhibit an average diameter of 1.67 $\pm$ 0.87 μm.

3.2.2 Thermal diffusivity measurements:

Measurements of the thermal diffusivity (α) were done using a photothermal technique called thermal wave resonant cavity (TWRC) [95, 96]. The experimental setup is shown in figure 3.2. The setup consists of a cylindrical container, which at its bottom has a pyroelectric film of lead zirconate titanate (PZT). The liquid sample is contained in this cylinder in contact with the PZT. A second cylinder, concentric with the first one, has its bottom closed with a silicon crystal (500 μm). It is introduced inside the fluid and can be displaced vertically, removing or introducing the liquid in the gap which separates the silicon wafer and the pyroelectric sensor depending on the direction in which the displacement is performed, as

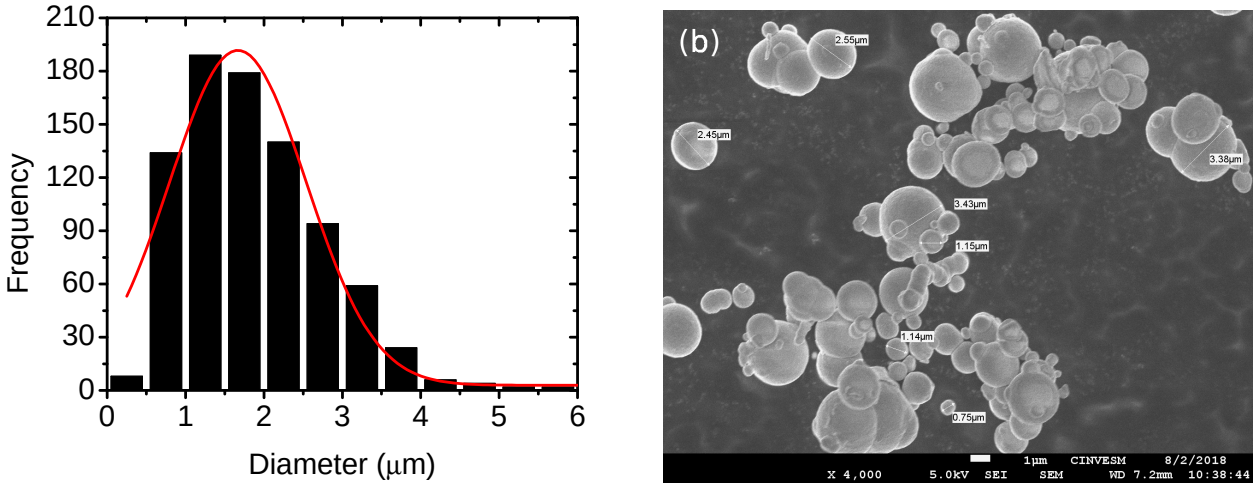

Figure 3.1: a) Histogram showing the size distributions of particles of CIP. b) SEM image of a particles of CIP at 4000X

shown in figure 3.2. The upper face of the silicon wafer is illuminated with a laser of 660 nm, with a power of 120 mW and modulated at a frequency $f = 0.5$ Hz. The silicon wafer absorbs the incident laser light, creating a temporal sinusoidal temperature profile, generally known as thermal wave [97]. The thermal wave is transmitted through the sample and it is detected by the pyroelectric sensor. The voltage of this detector is preamplified (SR560) and sent into a lock-in amplifier (SR830) and stored in a computer.

The magnetic field was generated by a pair of Helmholtz coils, and the TWRC is positioned at its center in such a way that the magnetic field reaches its maximum uniformity in the zone in which the sample is positioned. Before each measurement, each sample was previously sonicated. The intensities of the magnetic fields were 25, 50, 75, 100 and 150 Gauss and the measurements were performed at room temperature ($\sim 25°$C).

In section 2.2.4, it has been shown that the thermal diffusion length of a thermal wave is given by $\mu = \sqrt{\alpha/\pi f}$, in such a way that for a given material, the wave penetrates less when the frequency is higher and vice versa, allowing us to perform thermal depth profiles in materials [25]. When the thermal diffusion length of a sample with thermal diffusivity α is much lower than the cavity length (L), the diffusion regime is called thermally thick ($\mu \ll L$). In this case, the signal response of the system is given by equation A.14 and is

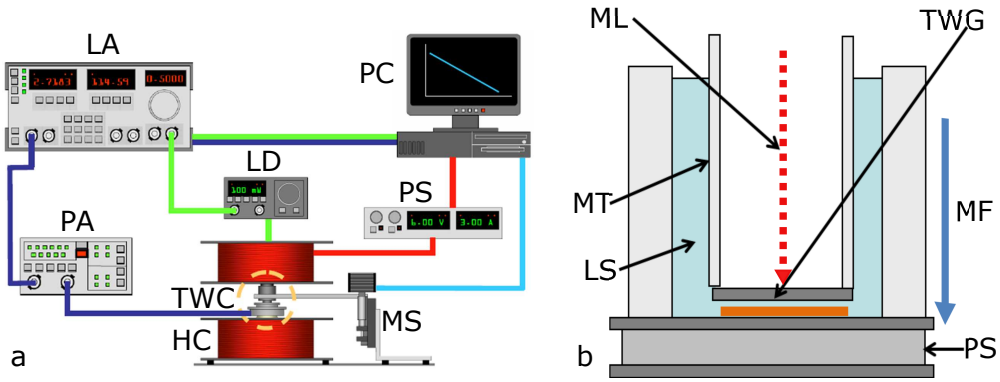

Figure 3.2: a) Schematic representation of the experimental setup. LA: Lock-in amplifier; PA: Preamplifier; HC: Helmholtz coils; TWRC: Thermal wave resonant cavity; LD: Laser driver; PC: Computer; PS: Programmable DC Power Supply; MS: Micrometer stage. b) TWRC in detail. ML: Modulated laser beam; MT: Moving Tube; LS: Sample; TWG: Thermal wave generator; MF: Magnetic Field; PS: Pyroelectric sensor.

presented below for convenience [95],

$$V(L,\alpha,f) = M(f)\exp\Big[-L(1+i)\sqrt{\pi f/\alpha}\Big] \tag{3.1}$$

where $M(f)$ is related with the frequency response of the pyroelectric sensor and with the efficiency of the light-into-heat conversion of the thermal wave generator (silicon wafer). The mathematical details for the derivation of the equation 3.1 are presented on section A.1.1.

Experimentally, in this work, the signal (V) is studied as a function of the thickness (L) of the sample. Since the frequency was fixed at 0.5 Hz, M(f) takes a constant value. From equation 3.1, we can obtain the amplitude and the phase of the signal, which are given by $\ln|V| = -a_{fv}L + B_v$ and $\phi = -a_{f\phi}L + B_\phi$ respectively, where $a_{fv} = a_{f\phi} = \sqrt{\pi f/\alpha}$, taking a constant value. The experimental amplitude and phase data obtained from the lock-in amplifier can be used to determinate the thermal diffusivity using simple linear functions. Figure 3.3 shows the experimental data and its fitting for amplitude and phase for the silicon-oil based fluid. It can be seen that the predictions for the thermal diffusivity obtained by means of the amplitude ($\alpha = 1.04 \times 10^{-3}$ cm^2/s) and phase ($\alpha = 1.03 \times 10^{-3}$ cm^2/s) measurements are very close, showing the versatility and accuracy of the methodology.

In order to obtain the thermal conductivity at a given concentration of microparticles (ϕ), the relationship between the thermal conductivity (k) and thermal diffusivity, $k = \alpha\rho c$ was used, where ρ is the density and c is the specific heat. For the effective heat capacity per unit volume $(\rho c)_{eff}$ we used the additive relationship typical of extensive quantities:

$$(\rho c)_{eff} = (\rho c)_{CIP}\phi + (\rho c)_{OIL}(1-\phi), \tag{3.2}$$

where the heat capacity per unit volume of the carbonyl iron particles is $(\rho c)_{CIP}$ and of the liquid matrix is $(\rho c)_{OIL}$ respectively. In the case of the effective thermal conductivity (k_{eff}) a simple linear relation, can be assumed as a working useful approximation,

$$k_{eff} = \alpha_{exp}[(\rho c)_{CIP}\phi + (\rho c)_{OIL}(1-\phi)] \tag{3.3}$$

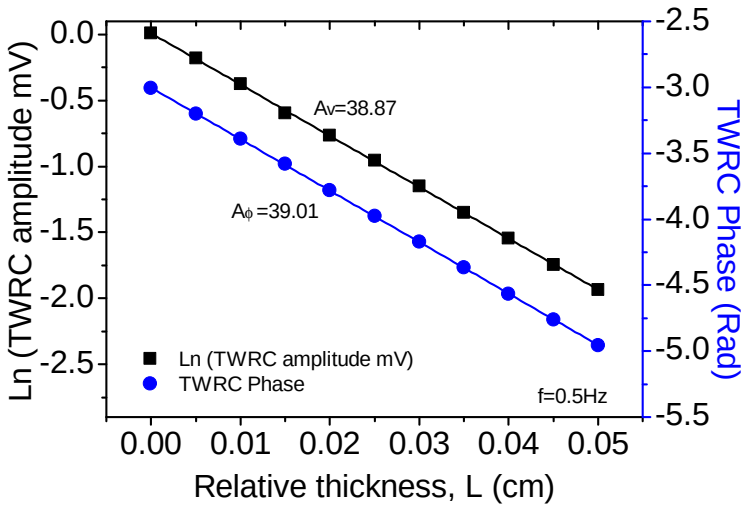

Figure 3.3: Thermal-wave signal for amplitude (black square dots) and phase (blue circular dots) for silicon oil. The dots represent the experimental data and the continuous line the best fitting as discussed in the text.

The values of the product $(\rho c)_{CIP} = 3.620$ Jcm^{-3}K^{-1} for carbonyl iron was taken from the literature [98]. For silicone oil $(\rho c)_{AS} = 1.398$ Jcm^{-3}K^{-1} was obtained from the value of the thermal effusivity (e), measured by a photoacoustic technique [99], using the relationship between the thermal difussivity and thermal effusivity ($\rho c = \epsilon/\sqrt{\alpha}$) and the value of the

thermal diffusivity for the liquid matrix measured with the TWRC as mentioned before (See figure 3.3).

3.2.3 Rheological measurements:

Viscosity measurements were performed with a SNB-1 Multi-speed Digital Viscometer/Rotational Viscometer, which employs a rotating cylinder [100]. This allows the determination of the viscosity by means of measuring the applied torque ψ and controlling the angular speed ω. The viscosity is given by the expression,

$$\eta = \left(\frac{1}{r_i^2} - \frac{1}{r_o^2}\right)\frac{\psi}{8\pi^4\omega h}, \tag{3.4}$$

where r_i is the radius of the cylinder, h is the height of immersion of the cylinder in the liquid and r_o the radius of a cavity containing the fluid. The system was placed in a magnetic field generated by the same pair of coils used in the TWRC.

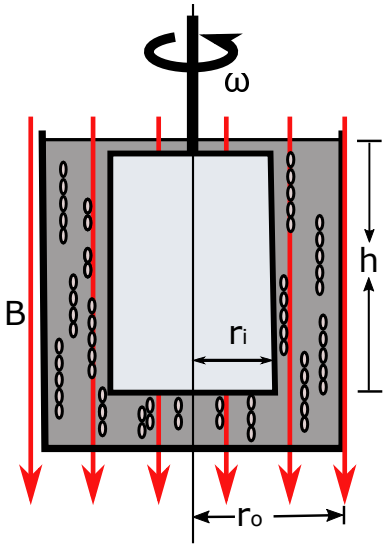

Figure 3.4: Diagram of a rotating cylinder viscometer. The case in which the magnetic field is parallel to the axis of rotation of the cylinder is illustrated.

It was considered that the changes induced in the MR fluid by the magnetic field have uniaxial symmetry as shown in figure 3.4. The viscosity was measured with three different

magnetic field directions: parallel to the cylinder and two orthogonal directions in the plane perpendicular to the cylinder. According to the configuration indicated by Beens and De Jeu [101], the reported viscosity is the average of the three viscosity coefficients obtained. Before each viscosity measurement, each sample was previously sonicated. The intensities of the magnetic fields were 25, 50, 75 and 100 Gauss and the measurements were performed at room temperature ($\sim 25°C$).

3.3 Results and discussion

Figure 3.5 shows the thermal conductivity in the direction of the magnetic field as a function of its strength. It is important to note that the simple presence of the particles increases the thermal conductivity. At the highest concentration of CIP (20%), the thermal conductivity increases to 3 times the conductivity of the matrix. Additionally, the thermal conductivity displays a significant increase as a function of the applied magnetic field, even for the lowest CIP concentration. The effect of the magnetic field becomes larger as the concentration of CIP grows.

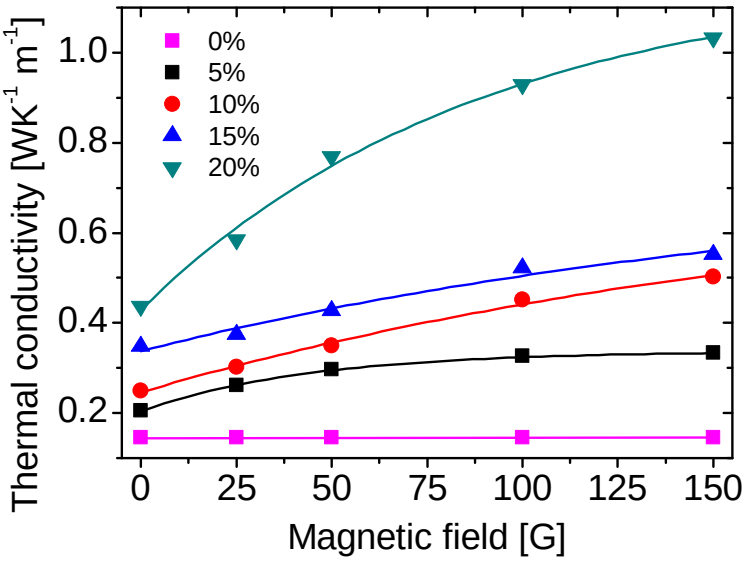

Figure 3.5: Thermal conductivity versus magnetic field for different concentrations of CIP. The dots represent the experimental data and the continuous line the best fitting to equation 3.6.

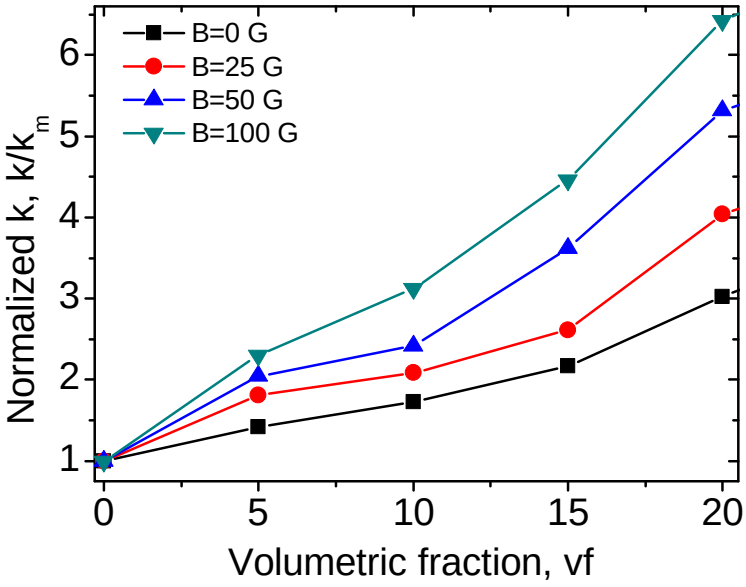

Figure 3.6: Thermal conductivity normalized to the thermal conductivity of silicone oil versus volumetric fraction for different magnetic fields. Lines are given only as a guide to the eye.

Figure 3.6 shows the thermal conductivity, normalized with respect to that of the matrix. In the case of 20% CIP concentration, the addition of CIP increases thermal conductivity by a factor of 3, and reaches a maximum of 6.4 times with a 100G magnetic field.

The increase in the thermal conductivity is consistent with that reported by Shulman *et al.* [85]. They found, using CIP in oil at 20 wt.%, that the thermal conductivity increased up to 1.4 times compared to the sample without magnetic field. Reinecke *et al.* [13], using the hot wire technique, reported increments of more than 1.4 times (20 Vol%) compared to the sample without a magnetic field. For samples of CIP in light mineral oil, Yildirim and Genc [14], using a steady state thermal resistance technique to analyze suspensions of iron powder with silicone oil at different temperatures, found that the fluids showed an increase in the thermal conductivity (20 Vol %) from 1.4 to 2 times the value for the matrix. In this work the increase of the thermal conductivity is consistent with the previous reports even though it is difficult to do proper comparisons, due to the differences in the characteristics of the matrices and the filler particles.

Figure 3.7a shows that the viscosity increases with the addition of CIP, for example,

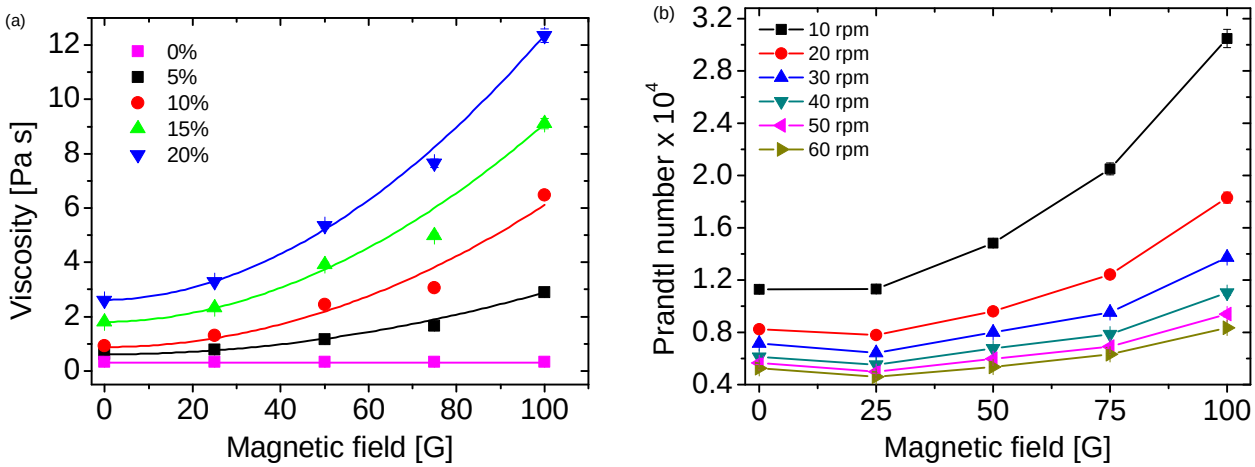

Figure 3.7: a) MR Suspension viscosity as a function of magnetic field at different volumetric concentration of CIP, for 20 rpm. The markers represent the experimental results and the solid lines are best fit of equation 3.5 to the measured data. b) Prandtl number as a function of magnetic field at different shear rates for volumetric concentration of 20%. Lines are given only as a guide to the eye.

by adding 20% of the CIP the viscosity increases from 0.61 to 2.20 Pas. Furthermore, the interaction with the magnetic field leads to an additional increment in the viscosity. For example with 10% CIP the viscosity increases from 0.86 to 6.4 Pas (measurements were carried out at 20 RPM). Figure 3.8a shows the decrease of viscosity with increasing shear rate. These two characteristics of the MR have been well documented [102–104], an explanation of this behavior is based on the assumption that the chain structures induced by the magnetic field are larger and more numerous as the amount of particles increase. This induces an increase in the viscosity as the chain structures encounter a greater resistance as they move. On the other hand when these chains are subjected to shear stress they are partially destroyed, reducing the viscosity.

Dynamic viscosity and thermal conductivity can be related through the non-dimentionalized quantity referred to as the Prandtl number, $Pr = \mu c_p/k$. Figures 3.7b and 3.8b show Pr as a function of magnetic field and shear rate respectively. The figures show that the Prandtl number attains higher values as the magnetic field and concentration increases and

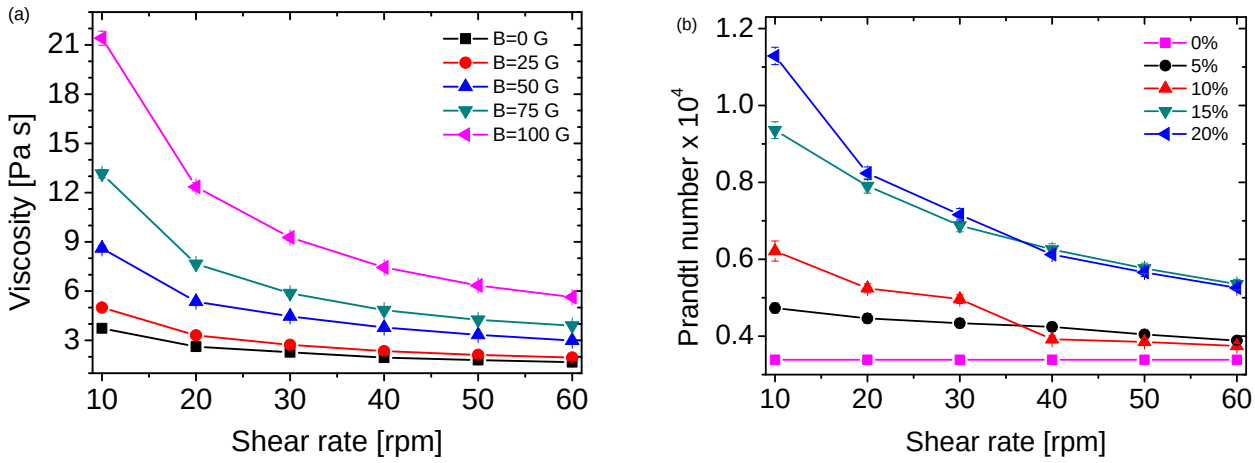

Figure 3.8: a) Suspension viscosity as a function of shear rates at different magnetic field for volumetric concentration of 20%. b) Prandtl number as a function of shear rates magnetic field at different volumetric concentration of CIP, without magnetic field. In both plots, the lines are given only as a guide to the eye.

lower values as the shear rate increases. We obtained a high Pr number between 10^3 and 10^4, compared to water which is ∼7 and air ∼0.7 [105]. High values of Pr from 10^3 to 10^5 were also found in experiments with polybutylene [106]. Measurements of carbopol [107] report values of Pr between 7 to 10^3. This shows that highs values of Pr denote the predominance of viscous effects over thermal.

3.3.1 Relationship between the thermal conductivity and viscosity

In order to analyze the relationship between the thermal conductivity and viscosity, we use the functional dependence that has been found between viscosity and the magnetic field [103]

$$\eta = \eta_0 + AB^N \tag{3.5}$$

where, η_0 is the viscosity of the suspension of particles, A is a constant, B the magnetic field and N is an exponent ranging between 1 to 2.

Using regression analysis, the coefficients A and N can be determined for each sample as shown in figure 3.7. For all volume concentrations the average value of the coefficient N

was 1.92, the maximum value was 2 and the minimum 1.68, which is consistent with the model assumptions. Figure 3.9 shows the parameter A as a function of shear rate. It can be seen that the value for the factor A decreases with increasing shear rate. This type of fluid behavior can be modeled by Herschel-Bulkley's power law formula [108].

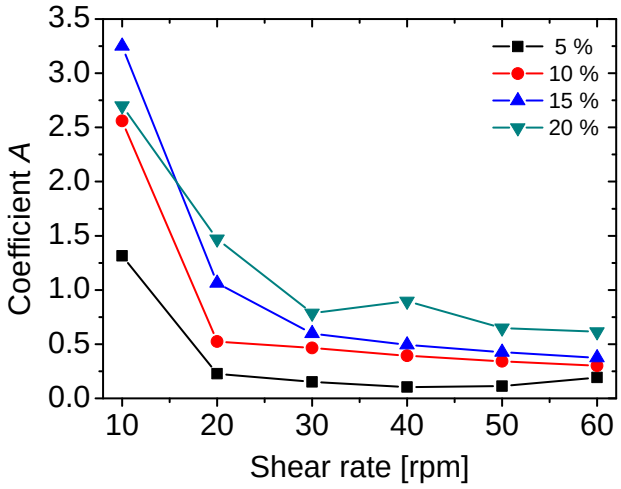

Figure 3.9: Coefficient A as a function of shear rate. Lines are given only as a guide to the eye.

The model for the behavior of the thermal conductivity and magnetic field, was proposed based on the model suggested Shulman [85], which includes the dependence on the filler concentration and the magnetic field.

$$k(\phi, B) = \alpha[(\rho c)_{CIP} + (\rho c)_{OIL}(1-\phi)] + D\phi(1 - \exp[-C(1-\phi)B]) \tag{3.6}$$

We can identify the first term as the effective thermal conductivity at zero magnetic field, which will be named k_0. The second term provides the contribution of the magnetic field, D and C are fitting parameters. The information of the D and C parameters (see table 3.1) was obtained by fitting the experimental data using equation 7 (See figure 3.5).

Substituting equation 3.5 into equation 3.6 we can establish an equation for the thermal conductivity in terms of concentration and viscosity in the form,

$$k = k_0 + D\phi\left(1 - \exp\left(-C(1-\phi)\sqrt[N]{\frac{\eta - \eta_0}{A}}\right)\right) \tag{3.7}$$

Sample	C	D
5%	0.023	26.6
10%	0.006	48.3
15%	0.005	26.8
20%	0.013	37.1

Table 3.1: C and D parameters obtained by fitting of the experimental values of thermal conductivity and magnetic field with equation 3.6.

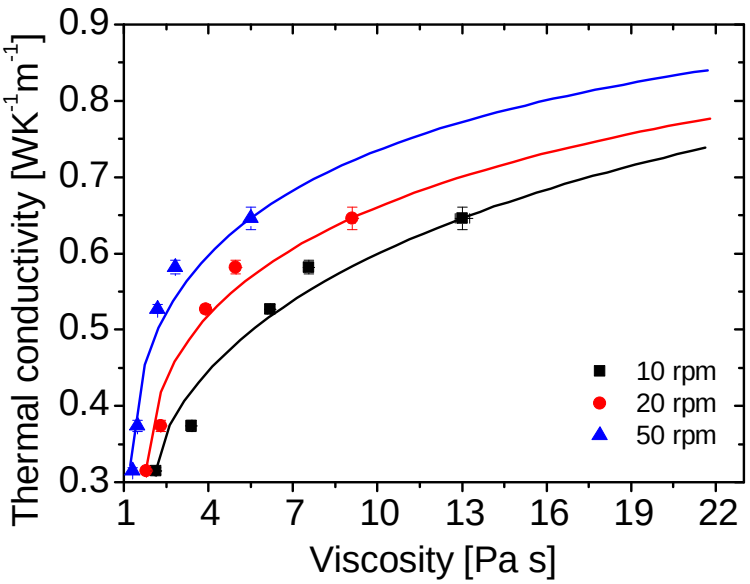

Figure 3.10: Thermal conductivity for the MR suspension as function of viscosity, for 15% and different values of shear rate. The dots represent the experimental results and the solid lines correspond to the model (equation 3.7).

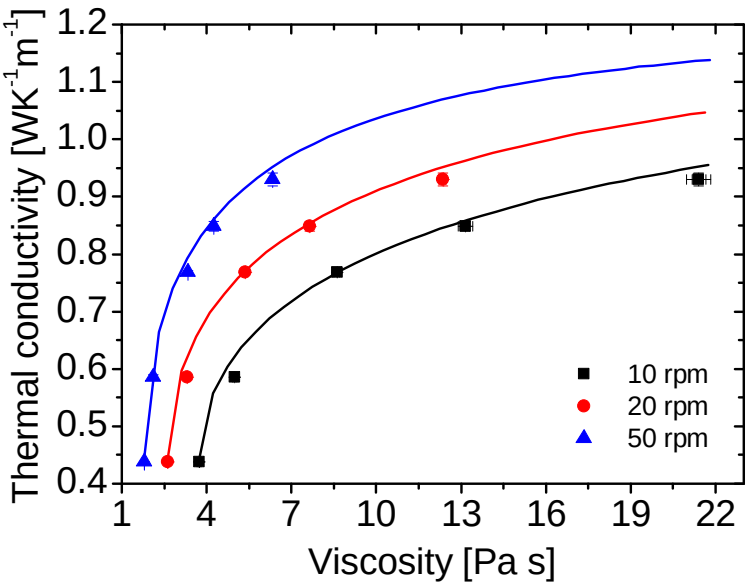

Figure 3.11: Thermal conductivity for the MR suspension as function of viscosity, for 20% and different values of shear rate. The dots represent the experimental results and the solid lines correspond to the model (equation 3.7).

Figures 3.10 and 3.11 show the thermal conductivity as a function of the viscosity. As the MR suspension becomes more viscous it becomes a better transporter of heat, in such a way that for values above 12 Pa s the thermal conductivity reaches an asymptotic behavior and heat transfer stays stable even if the viscosity continues increasing. This behavior indicates that thermal conductivity would become nearly insensitive at high viscosities. In other words if the magnetic field is increased, the viscosity would continue growing but the thermal conductivity will remain constant. Increase of thermal conductivity with viscosity is an interesting relationship which has been previously found in various systems. Ding *et al.* [86] performed the analyses of the experimental data of viscosity and thermal conductivity of (different already published) experimental data for nanofluids with nanoparticles made from different types of materials. From their studies they inferred that the structuring by aggregation of nanoparticles affects both the thermal conductivity and viscosity of nanofluids indicating how the two transport properties are related through the nanoparticle structuring.

Colla *et al.* [88] studied Fe_2O_3 water-based nanofluids, finding that the increment in

thermal conductivity is accompanied with a rising in dynamic viscosity. They discussed the role of type of flow on the effect on the thermal conductivity. Yang *et al.* [87] studied the effects of dispersant concentration, of carbon nanotubes in oil dispersions on thermal conductivity and steady shear viscosity. They showed that the thermal conductivity and viscosity are correlated with the size of large scale agglomerates, or clustered nanotubes.

Similarly in photopolymerization of resins [89, 90], a relationship between the thermal conductivity and polymerization was found, which involves an increase in viscosity. In these cases the linking of the polymers results in an increase of both the thermal conductivity and viscosity.

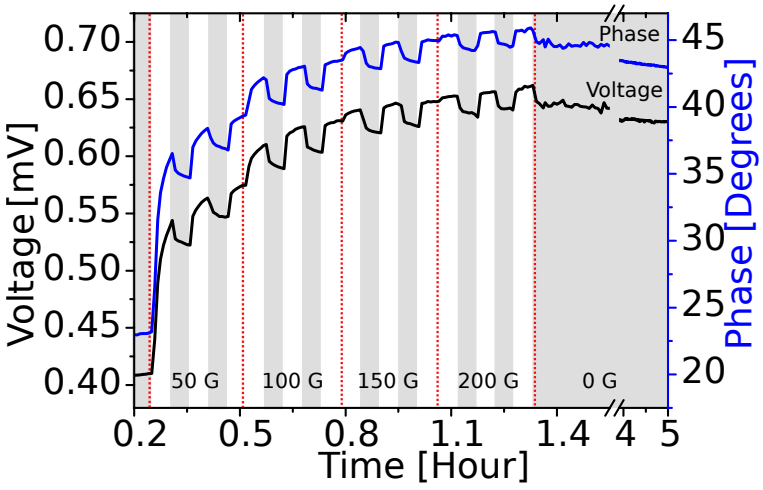

Figure 3.12: Curves of amplitude and phase as function of time, at frequency of 0.5 Hz, for the silicon rubber with CIP to 10%.

In order to analyze the MR fluid heat transfer response as well its stability in time, the thermal wave resonant cavity (TWRC) signal was recorded while turning on and off the magnetic field. The results of these experiments are shown in Figure 3.12 for a MR fluid with 10% of CIP. Note that an increasing magnetic field with values of 50, 100, 150 and 200 Gauss have been applied. The time intervals, at which field is turned on, correspond to the white strips and when the field is off correspond to the gray strips. In the first stage, as soon as the 50 Gauss is applied, the signal grows rapidly, and when the field is turned off the signal does not fall to the initial value, but decreases slowly. Again another 50 Gauss field is

applied and the signal grows slowly. This process is continued by changing the intensity of the magnetic field, which is indicated with the red vertical dotted lines. It can be observed that the changes of the TWRC signal, when the field is turned on and off become smaller when the magnetic field intensity increases. Note that after 1.3 hours, when the field was turned off definitely the TWRC signal does not go to zero but decreases very slowly, in such a way that after 3.5 hours this signal have only decreased in 3.5%.

All this process can be understood in terms of the microstructuring of the CIP. At the beginning, when the magnetic field is turned on, the CIP become aligned forming a chain structure and making the signal of the TWRC to grow very fast. However, given that the liquid matrix is viscous, the structuring of the particles is not complete, some particles have not taken their position in the alignment or the formed chains are not completely aligned along the magnetic field direction. When the field is turned off, the particles start to move out of their nearly fixed position in the structured arrangement, however, given that the liquids are viscous, this process is very slow. When turning on the field again, the particles start to become restructured, but given that they are partially ordered, they are more easily realigned and the chain structure also improves, in consequence a larger TWRC signal can be reached. This process of partial disordering and ordering continues, up to a maximum which depends on the viscosity of the liquid matrix. At the last part, when the field is turned off definitely, the particles begin to become disordered, however given that our matrix are very viscous, this can take a very long time. This is an interesting characteristic of our MR fluids, which could be useful in devising applications of smart thermal windows. Let us assume that the development of a window is desired, with the ability to become a good thermal conductor for a specific application. This could be done using a window containing a magnetic fluid and applying a magnetic field, as discussed before. However, for ferrofluids or MR Fluids in a low viscosity matrix, as soon as the field is turned off, the windows turns back to a nearly original value of its thermal conductivity. Therefore in order to keep constant the thermal conductivity of the window for a long period of time, the field cannot be turned off, at least not for long periods of time, which generates a high expense of energy. In contrast using our

MR suspension we can turn on the magnetic field for a few minutes and then turn it off, and we are certain that the thermal window will have a nearly constant thermal conductivity for a long time, expending in consequence less energy.

3.4 Summary

This study investigated the thermal and rheological behavior of a MR suspension composed of silicon oil and carbonyl iron powder. It was found that the addition of CIP combined with a magnetic field induce the formation of chains that increases significantly the thermal conductivity and viscosity. Although the dynamic viscosity increases with concentration and with the magnetic field, this effect can be reduced by increasing the shear stress, which is typical of non-Newtonian fluids. The viscosity plays an important role in the formation of chains, in such a way that the formation of ordered chains of magnetic particles becomes slower, due to the fact that we are working with a high viscosity fluid. A functional dependence between the thermal conductivity and viscosity was found, showing that when the viscosity keeps growing the thermal conductivity reaches a maximum stable value. The magnetic fluids obtained can be helpful when requiring changes of the thermal conductivity which can be kept for long periods of time, which could be used in the development and design of thermal windows.

Chapter 4

Complete thermal characterization of liquids using the front-face flash method

In the previous chapter, the thermal properties of the fluid were determined by measuring the thermal diffusivity and by the theoretical calculation of the heat capacity per unit volume. In this chapter, the aim is developing a methodology that allows the complete thermal characterization of fluids, that is to say, obtain experimentally two independent thermal properties and can be extended to study controllable fluids with external magnetic or electric fields.

4.1 Introduction

Heat transfer in liquids has attracted the attention of the scientific community in the last decades due to its important role in industry. Particularly, in the design and operation of heat exchangers, for power generation, air-conditioning, cooling devices in microelectronics, among many others. [109,110]. The three most relevant parameters for these applications are: thermal conductivity K, thermal diffusivity α and thermal effusivity ϵ (or the heat capacity c) which are linked [29] by the relationship $K = \rho c \alpha = \epsilon\sqrt{\alpha}$, where ρ is the density of the

material. Consequently, only two thermal transport properties have to be measured in order to perform a complete characterization of a given material.

There are several methods to measure the thermal properties of liquids [110–118]. However, methods like hot wire or 3ω are invasive to the liquid and they may be more sensitive to convective heat transfer than to heat conduction [117, 119]. Nevertheless, the photopyroelectric method (which is also contact based) has shown to be very accurate for determination of thermal properties [114, 120, 121]. On the other hand, non-contact methods present an advantage for studying the thermal properties of fluids under the action of magnetic or electric fields. This is a challenging and interesting research topic in complex fluids. Accordingly, there have also been several investigations focused in the rear-face (classical) flash method [122] for measuring the thermal properties of liquids. However, some limitations have been found, for example, when using a laser flash apparatus, the presence of air bubbles in a required closed cell induces errors in the measurements wich are difficult to account for [123]. Additionally, when using a measurement cell, made of two thin metallic cylindrical walls enclosing a liquid, it was found that the thermal diffusivity and thermal effusivity of liquids cannot be retrieved simultaneously [117]. However, when using this methodology α and ρc could be estimated.

In this chapter, the front-face flash method [124] is successfully used for the first time to retrieve simultaneously α and ϵ of liquids. The measurement cell consists of two metallic slabs enclosing a liquid layer. One-dimensional heat conduction is considered through this three-layer system. The effect of the liquid thermophysical properties on the front surface temperature, after applying a uniform heating pulse, is explored. Sensitivity analysis[1] of the illuminated surface temperature evolution to the changes of thermal diffusivity and thermal effusivity is done. This provides information about the optimum layers' properties, which allows us to obtain both thermal properties from a single measurement. Several common

[1]Local sensitivity analysis is the assessment of the local impact of input factors' variation on the model response by concentrating on the sensitivity in the vicinity of a set of factor values. Such sensitivity is often evaluated through gradients or partial derivatives of the output functions at these factor values, i.e., the values of other input factors are kept constant when studying the local sensitivity of an input factor [125].

non-metallic liquids and a thermal compound based on silicone (silicone grease), covering a wide range of thermal effusivities, are studied. Finally, the method is applied to study the thermal properties of a magnetorheological fluid.

4.2 Theoretical model

Figure 4.1 shows the geometry of a three-layer system made of two metallic slabs of thickness L_1 each and a liquid layer of thickness L_2. One metallic surface is illuminated uniformly by a flash lamp pulse, and the corresponding Laplace transform of the temperature rise at the front surface ($z = 0$) was calculated in the section A.2.6 (equation A.48) and is presented again below

$$\theta(0) = \frac{\bar{I}_0 \chi S \left(A_{3L} + B_{3L} h S\right)}{C_{3L} + (A_{3L} + D_{3L}) h S + B_{3L} h^2 S^2}, \tag{4.1}$$

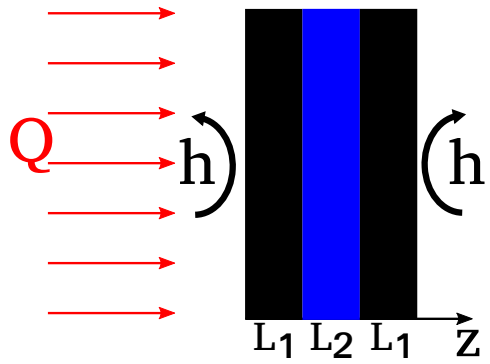

Figure 4.1: Diagram of a three-layer system consisting of a solid slab, a fluid layer and another solid slab. The surface $z = 0$ is uniformly illuminated by a brief flash lamp pulse.

which was obtained considering adiabatic boundary conditions: $\phi(0, s) = \bar{I}_0 \chi S$ and $\phi(L, s) = 0$. The factor χ is the energy fraction absorbed by the front surface. $\bar{I}_0$ represents the Laplace transform of the light pulse. If a Dirac delta intensity pulse $I_0 = Q\delta(t)$ is considered, its Laplace transform is $\bar{I}_0 = Q$, where Q is the energy per unit area ($\mathrm{Jm^{-1}}$) delivered by the pulse. The quadrupole coefficients A_{3L}, B_{3L}, C_{3L} and D_{3L} given in equations A.47 can be

written in terms of the following five parameters: $Q\chi/\epsilon_1$, $x_1 = L_1/\sqrt{\alpha_1}$, $x_2 = L_2/\sqrt{\alpha_2}$, $b_{21} = \epsilon_2/\epsilon_1$ (the ratio between the thermal effusivity of the liquid to that of the solid) and h/ϵ_1. Consequently, the Laplace transform of the front-face temperature $\theta(0)$ and the corresponding surface temperature evolution $T(0)$ depends on those five parameters. We assume that x_1 is known and it can be fixed during the evaluation of $T(0)$. Accordingly, a fit of $T(0)$ as a function of time, involving the other four parameters, may allow to retrieve α_2 and ϵ_2 simultaneously, as long as the thickness of the fluid layer L_2 and the thermal effusivity of the solid layer ϵ_1 are also known.

No analytical solution has been found for the inverse Laplace transform of $\theta(0)$. Consequently, the temperature evolution of the front surface has been obtained by applying a numerical inverse Laplace transform algorithm to equation A.48. In this case, the well-known Euler algorithm [126] has been used (see section A.2.2, in the appendix A), which provides accurate results for smooth functions. This condition is fulfilled by $\theta(0)$ given in equation A.48.

4.3 Simulations

Simulations of the surface temperature evolution $T(0)$ of a three layer system, after applying a short heating pulse, are shown in Fig. 4.2. The modeled system consists of two stainless steel AISI-316 ($\alpha_1 = 3.6$ mm^{2}s^{-1} and $\epsilon_1 = 7188$ Ws$^{1/2}$m^{-2}K^{-1}) slabs, and water ($\alpha_2 = 1.43$ mm^{2}s^{-1} and $\epsilon_2 = 1588$ Ws$^{1/2}$m^{-2}K^{-1}). The effect of the metallic slabs thicknesses on the surface temperature $T(0)$ is explored in Fig. 4.2a. An ideal Dirac pulse of intensity 1 kJm^{-2} and a typical heat convection coefficient [127] ($h = 10$ Wm^{-2}K^{-1}) are considered. Moreover, a dimensionless time t/τ_2 is introduced, in such a way that simulations are valid for any α_2 and L_2 values. The characteristic time $\tau_2 = L_2^2/(\pi\alpha_2)$, gives a measure of the time that it takes for the heat to propagate through a slab (liquid layer 'alone') after exciting with a Dirac like pulse [122]. The thickness of the liquid layer has been fixed to $L_2 = 1.0$ mm in all simulations. The first 'elbow' appears around $\tau_1 = L_1^2/(\pi\alpha_1)$ and indicates the time at which heat reaches the solid-fluid interface. This is shown with the blue vertical arrow, for

the case of $L_1 = 1$ mm. The second 'elbow' indicates the time when heat reaches to the non-illuminated slab backing surface and it depends on both τ_1 and τ_2. This is shown by the blue dashed arrow, also for $L_1 = 1$ mm. Moreover, as the thickness of the slab is increased, both elbows shift to later times. On the other hand, the dashed curve represents the case of no heat losses ($h = 0$). Note that the effect of heat losses is important only for long times after the heating pulse.

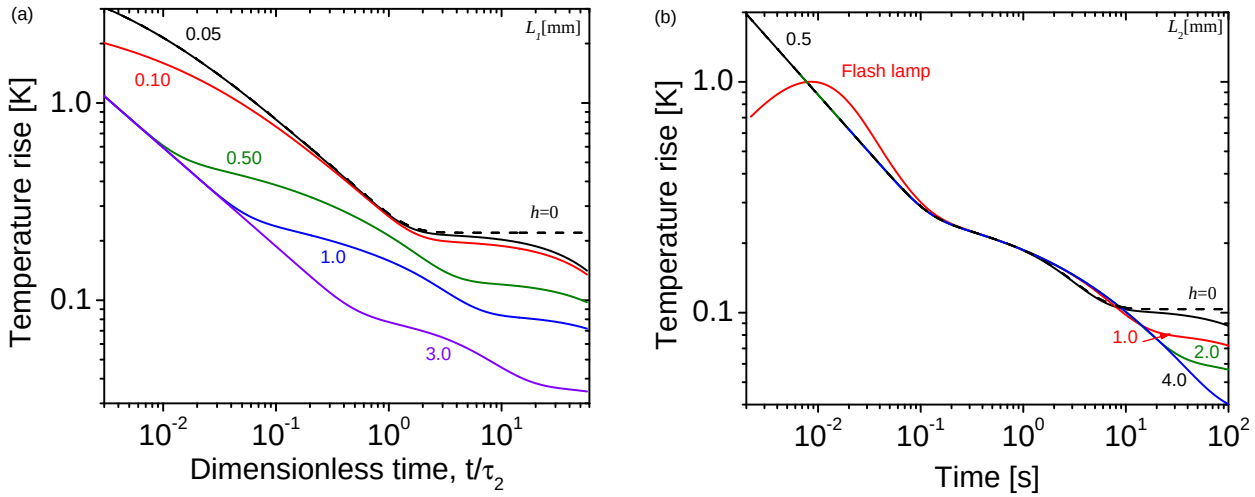

Figure 4.2: Surface temperature evolution $T(0)$ of a three-layer system consisting of two AISI-316 slabs and a water layer in the middle: (a) the effect of the solid thickness L_1 is explored and (b) the effect of the liquid layer thickness L_2 is shown.

For thin metallic slabs (50 and 100 μm in Fig. 4.2a), heat diffuses from the illuminated surface to the solid-fluid interface very fast. For example, $\tau_1 \approx 0.2$ ms for $L_1 = 50$ μm. This event can not be monitored by recording $T(0)$ with an infrared (IR) camera. Therefore, the use of thin metallic slabs would only allow to monitor heat conduction through the fluid and at the fluid-solid interface. Unfortunately, this is not enough for the simultaneous determination of the thermal diffusivity and thermal effusivity of the fluid [117]. Nevertheless, by increasing the slabs thicknesses it is possible to study the heat conduction through the whole three layer system. This is shown in Fig. 4.2a for the surface temperature evolution $T(0)$ for $L_1 = 0.50$, 1.0 and 3.0 mm. However, if a flash lamp pulse is used, then slabs with thickness $L_1 > 0.50$ mm are recommended. The use of thicker slabs help to reduce the

temperature rise at the solid-liquid interface, which prevents heat convection in the liquid. Nevertheless, it is necessary to fulfill the condition $L \ll \sqrt{A_{slab}}$ in order to keep valid the assumption of one-dimensional heat transfer through the three-layer system, where A_{slab} stands for the surface area of the slab.

Figure 4.2b shows the evolution of $T(0)$ induced by changing the thickness of the fluid layer (L_2). The thickness of each AISI-316 slab has been set to 1.0 mm for all simulations. The same thermal parameters of Fig. 4.2a has been used. Notice that, increasing L_2 only shifts the second elbow to later times, but the first one remains fixed by L_1, as expected. Accordingly, as the fluid layer gets thicker, the surface temperature evolution $T(0)$ is similar to that of a two-layer system, consisting of a metallic slab and a semi-infinite backing fluid (see Fig. 2 in Ref. [128]). Similarly to Fig. 4.2a, the case of no heat losses is represented by the dashed curve.

In general, the thermal diffusivity of non-metallic liquids is around 0.1 mm^2s^{-1} and covers a wide range of thermal effusivity values [120]. In order to study simultaneously the thermal diffusivity and thermal effusivity of these liquids, a measurement cell consisting of a couple of parallel stainless steel AISI-316 slabs separated by a liquid layer, has been considered, with $L_1 = L_2 = 1.0$ mm. Figure 4.3 shows the effect of several thermal effusivity ϵ_2 values corresponding to non-metallic and metallic liquids on the surface temperature evolution $T(0)$. An ideal Dirac pulse of intensity 1 kJm^{-2} and $h = 10$ $Wm^{-2}K^{-1}$ is considered. If the thermal effusivity of the slab equals the one of the fluid ($\epsilon_1 = \epsilon_2 = 7188$ $Ws^{1/2}m^{-2}K^{-1}$), there is no thermal mismatch at their interface and heat flows as in a semi-infinite sample ($T(0)$ is a straight line with $-1/2$ slope) until it reaches the backing surface $z = L$. For liquids with thermal effusivity lower than that of the metallic slab ($\epsilon_2 < \epsilon_1$), the thermal energy transfered to the liquid is smaller than that delivered by the metallic surface. This explains the temperature rise above the line of $-1/2$ slope for $t > \tau_1$. The time $t = \tau_1$ is represented by the dashed vertical line. The opposite occurs for $\epsilon_2 > \epsilon_1$, $T(0)$ shows a downwards displacement from the line of $-1/2$ slope for $t > \tau_1$. Moreover, for low values of ϵ_2, longer times are required for the heat to reach the rear surface $z = L$.

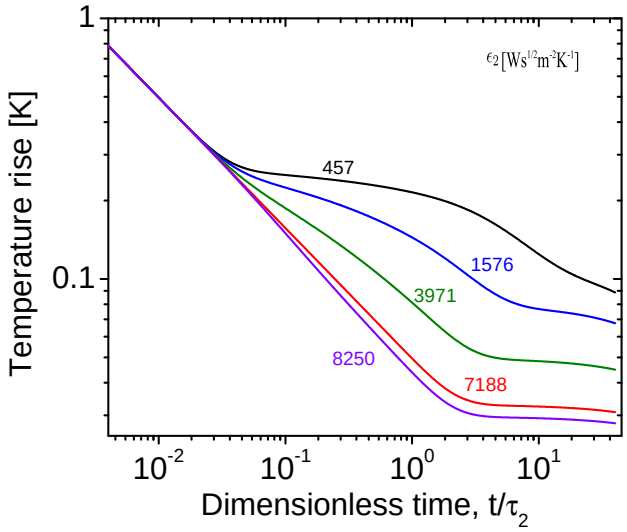

Figure 4.3: Surface temperature evolution $T(0)$ of a three-layer system consisting of two AISI-316 slabs and a liquid layer with a thermal diffusivity of 0.1 mm^2s^{-1}. The effect of several values of the fluid thermal effusivity is shown.

A local sensitivity analysis has been used to explore the usability of a three-layer system for estimation of both the thermal diffusivity and thermal effusivity of liquids from a single measurement. The local sensitivity of $T(0)$ to a given parameter $\beta = \{x_2, b_{21}\}$ is defined as [129]

$$Sy(\beta) = \frac{\beta}{T_1(0)} \frac{\partial T_1(0)}{\partial \beta}. \tag{4.2}$$

Simulations shown in Fig. 4.4 have been performed considering a 1 kJm^{-2} Dirac like pulse and $h = 10$ $Wm^{-2}K^{-1}$. Two parallel metallic slabs of stainless steel AISI-316 separated by a liquid layer with thermal diffusivity $\alpha_2 = 0.1$ mm^2s^{-1} are considered. The thicknesses of the layers ($L_1 = L_2 = 1.0$ mm) have been chosen according to simulations in Fig. 4.2. The dashed vertical lines show the maximum time accessible with our experimental setup.

Figure 4.4a shows the sensitivity of $T(0)$ to the parameter $x_2 = L_2/\sqrt{\alpha_2}$ as a function of the dimensionless time t/τ_2. The maximum sensitivity to x_2 is reached at $t \approx 4\tau_2$ for $\epsilon_2 = 8250$ $Ws^{1/2}m^{-2}K^{-1}$, but it shifts to longer times as the thermal effusivity decreases. In

particular, for $\epsilon_2 = 1576$ $Ws^{1/2}m^{-2}K^{-1}$ the maximum sensitivity is about $10\tau_2$. However, for lower thermal effusivities the maximum may shift to shorter times: $t \approx 6\tau_2$ for $\epsilon_2 = 457$ $Ws^{1/2}m^{-2}K^{-1}$. Additionally, there is no sensitivity to x_2 at times $t \lesssim \tau_2$, because at these times, heat has not reached yet the fluid-solid interface.

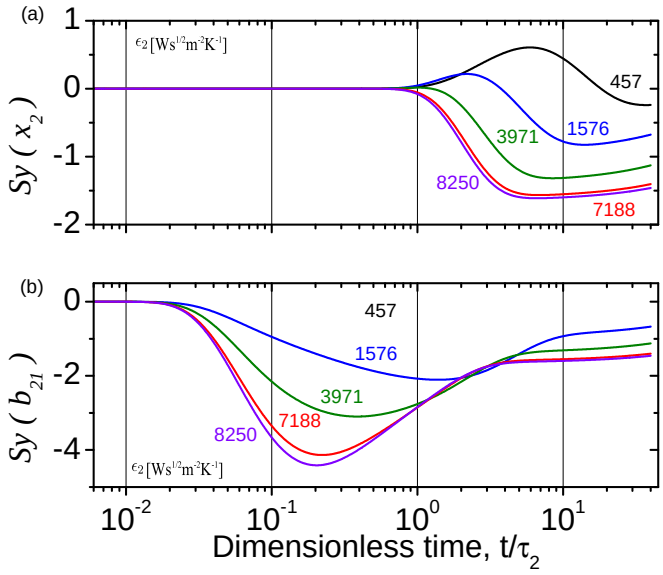

Figure 4.4: Sensitivity curves of the surface temperature $T(0)$ evolution to (a) x_2 and (b) b_{21}. Several values of the thermal effusivity ϵ_2 have been analyzed in order to explore the applicability of the method. Thermal diffusivity has been fixed to 0.1 mm^2s^{-1} in all simulations.

Sensitivity to the ratio of thermal effusivities $b_{21} = \epsilon_2/\epsilon_1$ for several values of ϵ_2 is shown in Fig. 4.4b. Notice that the maximum sensitivity to b_{21} always shifts to longer times as ϵ_2 decreases. For $\epsilon_2 = 8250$ $Ws^{1/2}m^{-2}K^{-1}$, the maximum sensitivity to b_{21} is about $t \approx 0.2\tau_2$. Accordingly, this parameter and x_2 (whose maximum is at $t \approx 4\tau_2$) can be retrieved simultaneously, from a single measurement of $T(0)$. On the other hand, for $\epsilon_2 = 457$ $Ws^{1/2}m^{-2}K^{-1}$ the maximum sensitivity to both b_{21} and x_2 is about $t \approx 6\tau_2$. If the maxima on the sensitivity to x_2 and b_{21} are close or overlap, then the retrieved values depend on the initial values provided to the fitting algorithm [129]. Nevertheless, notice that if the thermal effusivity of the metallic slab equals that of the studied fluid ($\epsilon_1 = \epsilon_2$), both the thermal diffusivity and thermal effusivity can be retrieved simultaneously, since the maxima of x_2 and b_{21} occurs at

different times (see the curves with $\epsilon_2 = 7188$ $Ws^{1/2}m^{-2}K^{-1}$ in Fig. 4.4).

According to these simulations, a three-layer system consisting of two parallel AISI-316 slabs and a liquid layer, is a good choice for simultaneous determination of the thermal diffusivity and thermal effusivity of liquids, by monitoring the surface temperature evolution $T(0)$. If each layer is 1.0 mm thick, then it is possible to study liquids covering a wide range of thermal effusivities. However, this configuration might provide low precision results for low thermal effusivity liquids $\epsilon \lesssim 500$ $Ws^{1/2}m^{-2}K^{-1}$. Nevertheless, it is possible to avoid this limitation by tuning the characteristics of the measurement cell (changing the slabs to attain different thermal properties and/or their thicknesses).

4.4 Experimental setup

Measurements on several reference liquids have been performed in order to validate the proposed method. The studied liquids cover a wide range of thermal transport properties: alcohols, oils, an oleic acid, water and silicone based fluids.

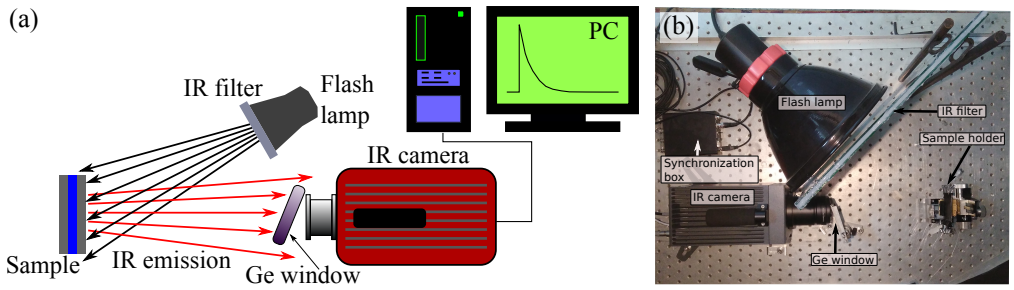

Figure 4.5: (a) Diagram of the experimental setup used in this work. A Ge window is used to protect the camera lens. The IR filter blocks the IR radiation emitted by the flash lamp. (b) Picture of our experimental setup.

The experimental setup, shown in Fig. 4.5, is used for measuring the temperature rise evolution of the heated surface. This allows simultaneous determination of α_2 and ϵ_2.

A flash lamp (Speedotron 206VF) working at 4.8 kJ per pulse is used as the heating source. The pulse duration extends up to 20 ms and its temporal shape is included in the

model, as described below. A home-made infrared (IR) filter, composed of a water layer of 6.7 mm thickness between two soda-lime glass slabs of 3 mm thickness each, is placed in front of the sample in order to prevent the IR radiation, emitted by the flash lamp during a pulse, to reach the sample surface. This IR radiation extends to 0.1 s and it would affect the measurements if it is not blocked. Accordingly, in this work, only visible radiation of the flash lamp is available for exciting the sample surface. Moreover, a Ge window, which is transparent to mid infrared wavelengths, has been also used to prevent the flash lamp radiation from reaching the camera lens.

The IR radiation emitted by the sample surface is recorded with an IR camera (InfraTec 8320 working in the spectral range from 3 to 5 μm). Each pixel in the detector averages the IR emission coming from a square with dimensions 0.135×0.135 mm in the sample. Images are recorded at a rate of 200 frames per second.

The noise equivalent temperature difference (NETD) [130] of our IR camera is below 35 mK. The temperature detected by the IR camera is not the real surface temperature rise, because its emissivity is not known. However, the "apparent" temperature rise ΔT measured by the IR detectors is proportional to the real temperature from the sample front surface.

The measurement cell is a three-layer system which consists of two parallel stainless steel AISI-316 slabs (0.820 mm thick, 30 mm lateral and 40 mm vertical dimensions) separated by a three-sided homogeneous glass frame (0.930 mm thick). The space left between both metallic slabs and the glass frame is filled (from the top) with a liquid, as shown in Fig. 4.5. The dimensions of this cell, in the case of short duration light pulses, allow fulfilling the condition of one-dimensional heat conduction indicated in Sec. 4.3.

Although all simulations in Sec. 4.3 were done assuming a Dirac-like pulses, for the actual measurements, we used a flash lamp. The light intensity of the flash lamp pulse follows an exponential model of the form $I_0(t) = (Qt^\gamma/N\tau^{1+\gamma})\exp(-t/\tau)$, for which the Laplace transform is $\bar{I}_0 = Q/(1+s\tau)^{1+\gamma}$. The parameters γ and τ depend on the pulse temporal shape. N is a normalization constant which is used to satisfy the condition $\int I_0(t)\,\mathrm{d}t = Q$. The light intensity of the flash lamp used in this work fits the exponential model with $\gamma = 0.117$ and

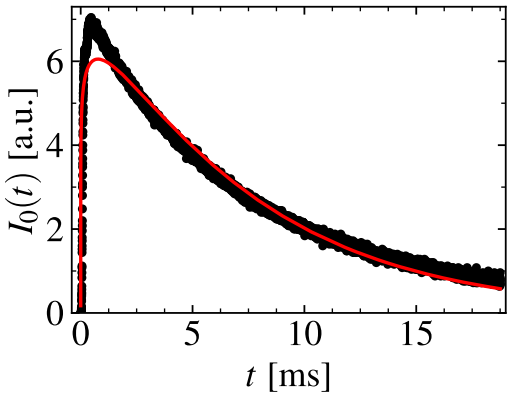

Figure 4.6: Intensity distribution of the flash lamp pulse. Dots represent the experimental data and the continuous line is the fitting to the exponential model.

$\tau = 6.6$ ms, both values are in good agreement with those of a typical flash lamp [131].

4.5 Results and discussion

Figure 4.7 shows the temporal evolution of the surface temperature for three liquids up to 50 seconds: (a) water, (b) silicone grease, and (c) silicone oil. The maximum temperature increases due to the flash lamp excitation is indicated for each liquid. Below each time trace, five thermograms (thermal images) corresponding to: 20 ms before the pulse, at the maximum intensity of the pulse, 0.5 s, 5 s and 30 s after the pulse, are included. A yellow rectangle in the thermograms indicates the corresponding area used to obtain the average temperature of each thermogram.

Note that the spatial variations of the temperature are small in the averaged area of each thermogram, i.e., homogeneous cooling occurs. Consequently, it can be inferred that the heat transfer is one-dimensional, which supports the fulfillment of one-dimensional heat transport condition given in Sec. 4.3.

Figures 4.8a and 4.8b show typical temperature evolution curves obtained for: distilled water, ethylene glycol (EG), a silicone grease (sil-glyde from AGS) and silicone oil (Polisil from POLIFORMAS). Experimental data is represented by dots and continuous lines are used for the curve fittings. Only one point out of ten is plotted. However, all data points

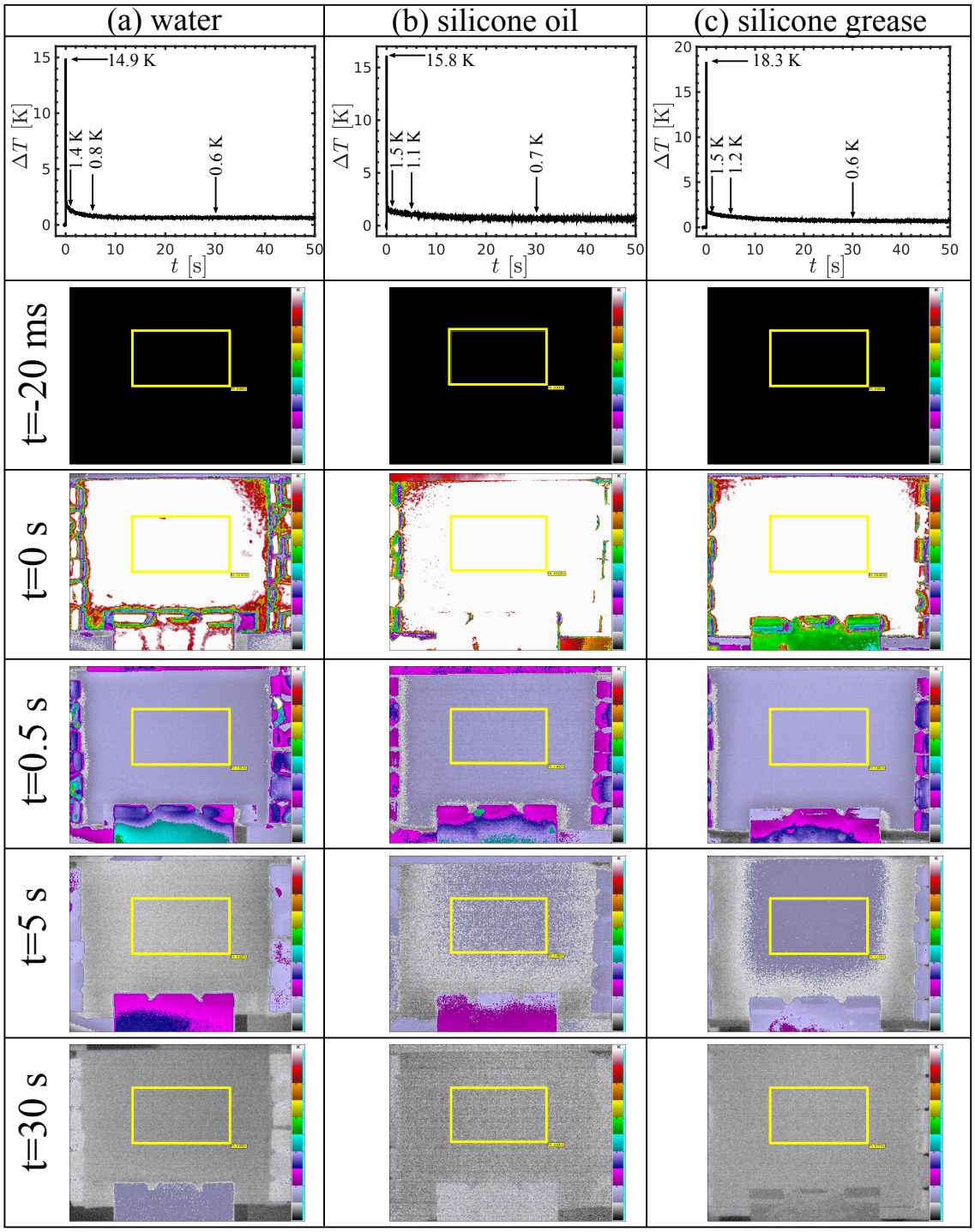

Figure 4.7: Surface temperature evolution and matrix of thermograms at five different times for three different liquids: (a) water, (b) silicone grease and (c) silicone oil.

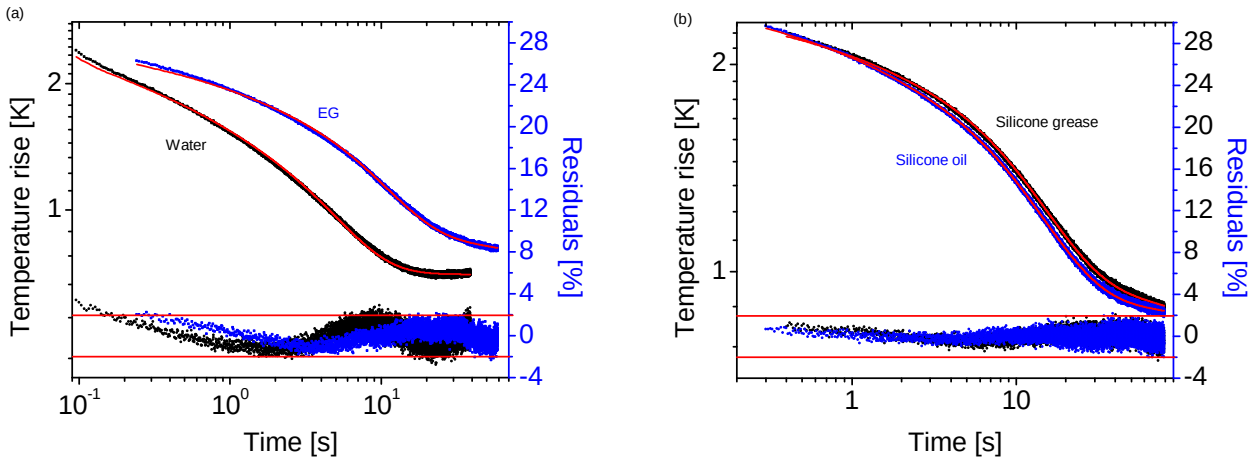

Figure 4.8: Results of the "apparent" temperature rise for (a) water and ethylene glycol and (b) silicone grease and silicone oil. Dots represent the experimental data and continuous lines are used for the fittings. Residuals are also presented. Horizontal red lines indicate the $\pm 2\%$ residuals.

have been included in the fittings. A least-squares fitting procedure based on the Levenberg-Marquardt algorithm [132,133] has been implemented for the fittings. The numerical inverse Laplace transform of equation A.48 has been fitted to the obtained experimental results. Four free parameters have been used in the fittings: $Q\chi/\epsilon_1$, $x_2 = L_2/\sqrt{\alpha_2}$, $b_{21} = \epsilon_2/\epsilon_1$ and h/ϵ_1. The residuals, i.e. the normalized difference between experimental data and fitted values, $(T_{exp} - T_{fit})/T_{exp} \times 100$, are also shown. The two horizontal red lines in Figures 4.8a and 4.8b indicate the $\pm 2\%$ residuals, showing the goodness of the fits. On the other hand, it is confirmed that measurements performed with the front-face configuration are less time consuming (around 90 s) than measurements using the classical (rear-face) flash method (more than 200 s) [117].

Table 4.1 shows the results obtained for α_2 and ϵ_2 of eight different liquids. Additionally, the thermal conductivity is calculated using $K_2 = \epsilon_2\sqrt{\alpha_2}$. Results are ordered from the highest thermal effusivity value to the lowest one. The uncertainties of α_2 and ϵ_2 are calculated from the standard deviation of five measurements. Error propagation [139] is also taken into account for the uncertainty of K_2. Good agreement between the values obtained in this work and previously reported ones in literature is found (see Table 4.1). For the thermal diffusiv-

Liquid	α_2 [mm^2s^{-1}] this work	α_2 [mm^2s^{-1}] literature	ϵ_2 [$Ws^{1/2}m^{-2}K^{-1}$] this work	ϵ_2 [$Ws^{1/2}m^{-2}K^{-1}$] literature	K_2 [$Wm^{-1}K^{-1}$] this work	K_2 [$Wm^{-1}K^{-1}$] literature
Distilled water	0.147 ±0.011	0.142 [134]	1524 ±36	1576.5 [134]	0.58 ±0.03	0.59 [134]
Glycerin	0.108 ±0.007	0.099 [115]	1002 ±26	920-970 [114, 120]	0.33 ±0.01	0.28 [120, 135]
Ethylene glycol	0.099 ±0.003	0.096 [120]	858 ±7	840 [120]	0.27 ±0.05	0.25 [135]
Oleic acid	0.101 ±0.005	0.103 [136]	656 ±25	554-682 [136, 137]	0.21 ±0.01	0.18-0.23 [136, 137]
Silicone grease	0.085 ±0.008	0.088 [112]	630 ±37	575 [112]	0.18 ±0.01	0.17 [112]
Mineral oil	0.104 ±0.005	0.065-0.10 [114, 120]	572 ±7	515-575 [114, 120]	0.18 ±0.01	0.12-0.18 [114, 120]
Engine oil	0.095 ±0.002	0.089-0.148 [134, 138]	537 ±8	460-543 [134, 138]	0.17 ±0.01	0.13-0.21 [134, 138]
Silicone oil	0.104 ±0.005	0.104 [112]	491 ±10	457 [112]	0.16 ±0.01	0.15 [112]

Table 4.1: Thermal diffusivity (α_2) and thermal effusivity (ϵ_2) of the liquids studied in this work. The thermal conductivity is calculated using $K_2 = \epsilon_2\sqrt{\alpha_2}$.

ity, the difference between the literature values and those obtained in this work are: 9% for glycerin, 6.7% for engine oil and below 4% for the other liquids. For thermal effusivity, the difference between the literature values and those obtained in this work are: 9.5% for silicone grease, 7.4% for engine oil and below 3.3% for the other liquids. Note that for some of the studied liquids, their thermal properties are extended over a range of values. This can be attributed to the purity grade, chemical composition and/or the fabrication method used to obtain the liquid.

4.6 Application for magnetorheological fluids

In this last part, the method is extended to retrieve the thermal properties of a fluid composed by silicon rubber and carbonyl iron powder, under the interaction of an external magnetic field. Since there is a time for chains formation, the time for the interaction of the sample-

field was set at 3 minutes. The magnetic field was generated by a pair of Helmholtz coils, and the sample is positioned at its center in such a way that the magnetic field reaches its maximum uniformity in the area where the sample is placed. The cell used to characterize the fluid is the same used in the last section. The fluid was divided into groups of 0, 1.7, 3.8, 6.4 and 13.5 vol % of CIP. The magnetic field intensity was set 0, 50, 150 and 250 G and the measurements were performed at room temperature ($\sim$ 25°C).

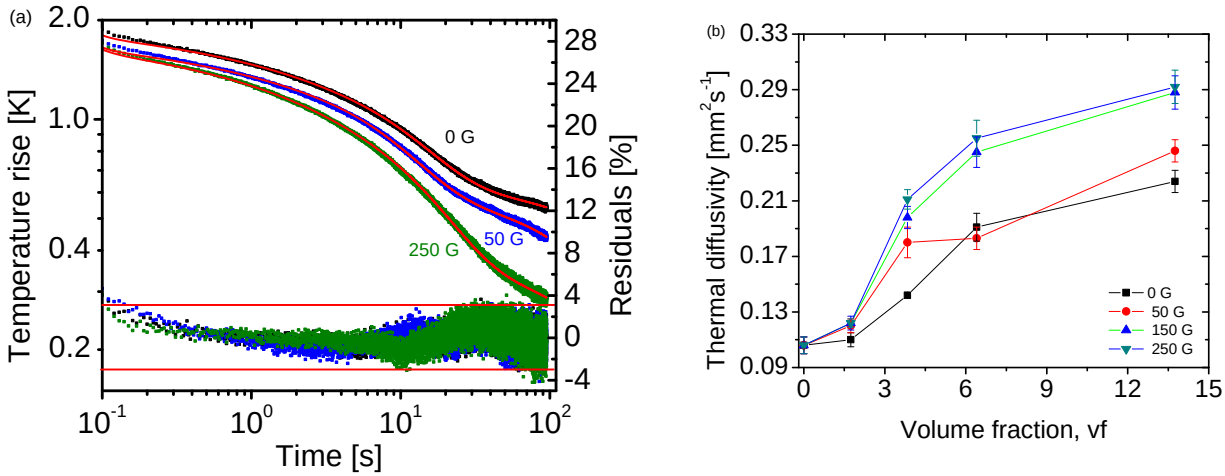

Figure 4.9: Temperature evolution and thermal diffusivity of silicon rubber with particles of CIP on the direction of the magnetic field. Dots represent the experimental data and continuous lines are used for the fittings. Residuals are also presented. (a) Temperature as a function of time at 13.5 vf, for 0, 50 and 250 G intensities of magnetic field. (b) Thermal diffusivity as a function of the volume fraction for several magnetic field intensities.

Figure 4.9 shows the temperature evolution and thermal diffusivity of silicon rubber with particles of CIP on the direction of the magnetic field. Figure 4.9a show typical temperature evolution curves obtained for silicon rubber filled with CIP at 50 vf, for 0, 50, 250 G. Experimental data is represented by dots and continuous lines are used for the curve fittings. Only one point out of ten is plotted. However, all data points have been included in the fittings. Figure 4.9b shows the experimental values of the thermal diffusivity on the direction of the magnetic field as a function of the volume fraction vf of CIP, for several magnetic field intensities. Each experimental point has been obtained from the average of five measure-

ments. Before each measurement, each sample was previously agitated. The dependence of the thermal diffusivity with the concentration for different field strengths shows that increasing the concentration and/or increasing the magnetic field an increase on thermal diffusivity is presented. The maximum thermal diffusivity value measured at the highest concentration considered in this work (13.5 vf) is 2.7 times that of the matrix for a magnetic field of at 150 and 250 G.

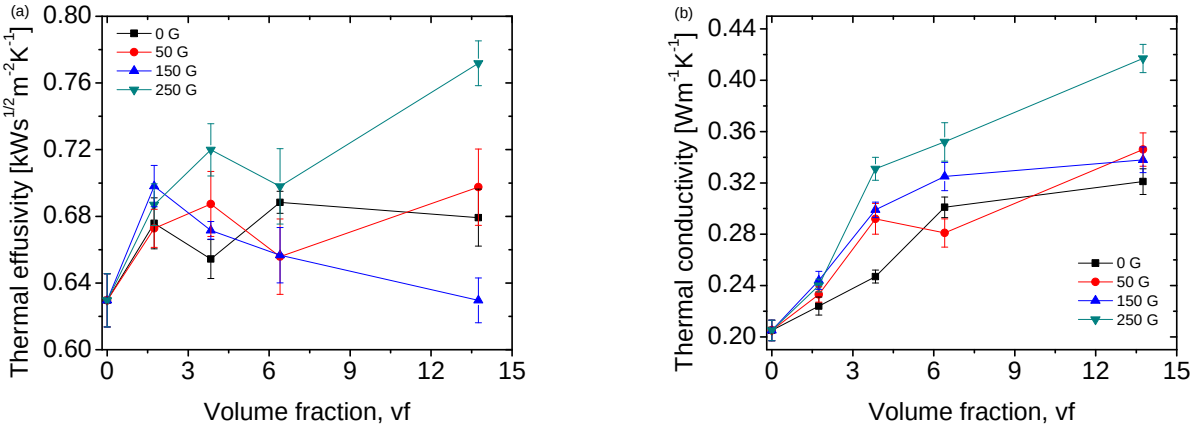

Figure 4.10: Thermal effusivity and thermal conductivity of silicon rubber with particles of CIP on the direction of the magnetic field. (a) Thermal effusivity as a function of the volume fraction and (b) Thermal conductivity as a function of the volume fraction, for several magnetic field intensities.

Figure 4.10 shows the experimental values for thermal effusivity and thermal conductivity of silicon rubber with particles of CIP on the direction of the magnetic field. Each experimental point has been obtained from the average of five measurements. Figure 4.10a shows the thermal diffusivity on the direction of the magnetic field as a function of the volume fraction vf of CIP, for several magnetic field intensities. Figure 4.10b shows the values of the thermal diffusivity on the direction of the magnetic field as a function of the volume fraction vf of CIP, for several magnetic field intensities. The thermal conductivity was calculated using $K_2 = \epsilon_2\sqrt{\alpha_2}$. The uncertainties of α_2 and ϵ_2 are calculated from the standard deviation of five measurements. Error propagation [139] is also taken into account for the uncertainty of K_2. The dependence of the thermal conductivity shows that increasing the

concentration and/or increasing the magnetic field, an enhancement on thermal conductivity appears. This behavior is in fairly good agreement with the results presented in chapter 3, especially in section 3.3. The maximum thermal conductivity value measured at the highest concentration consider in this work (13.55 vf) is 2 times that of the matrix for a 250 G of magnetic field strength.

On the other hand, the thermal properties of liquid metals could be studied with the front-face flash method taking into account that there must be a thermal mismatch at the fluid-solid interfaces. Accordingly, a thermal resistance at each interface should be included in the model. This method may also be applied to study the temperature dependence of the thermal transport properties of liquids. However, in this case, heat transfer by convection in the liquid cannot be neglected and has to be included into the model. Nevertheless, heat convection to the liquid may be reduced by placing the measurement cell in a horizontal position.

4.7 Summary

It has been shown that the front-face flash method provides non-contact, fast, simultaneous and accurate measurements of the thermal diffusivity and thermal effusivity of liquids. The estimated thermal conductivity is in good agreement with literature values, confirming the applicability of the proposed method. We have shown that the thermal characterization of liquids can be performed using a simple approach based on a one-dimensional heat diffusion equation for a three layer system illuminated by a short heat pulse. The time evolution of the illuminated surface temperature has been shown to be sensitive to both the thermal diffusivity and thermal effusivity of most liquids. However, for 1.0 mm thick stainless steel AISI-316 slabs and 1.0 mm thick liquid layer, both properties cannot be retrieved simultaneously for low thermal effusivity $\epsilon_2 \lesssim 500$ $\mathrm{Ws^{1/2}m^{-2}K^{-1}}$ values. In summary, it has been shown that our methodology, based on IR thermography, can provide a complete thermal characterization of most common liquids used in science and technology.

Chapter 5

Thermal and electric percolation in random in microparticles composites

In this work, the thermal and electrical percolation at room-temperature for composites made up of carbonyl-iron spherical particles randomly dispersed in a polyester resin matrix is studied, for volume fractions (vf) ranging from 0 to 0.55. A complete thermal characterization was done by measuring the thermal diffusivity α and thermal effusivity ϵ of samples through the front-face flash method, and determining the thermal conductivity $k = \epsilon\sqrt{\alpha}$ and volumetric heat capacity $C_v = \epsilon/\sqrt{\alpha}$. Our results for both k and α exhibit a clear percolation threshold at v_{pT}=0.38. On the other hand, the DC electrical conductivity was measured, showing an increment of 6 orders of magnitude with respect to the matrix and the electrical percolation threshold located in v_{pE}=0.46; this means a shift between the thermal and electrical percolation around 20%. Finally, the relationship between the electrical and thermal conductivity is presented.

5.1 Introduction

The incorporation of fillers with relatively high thermal or electrical conductivity into the polymeric matrix can enhance their thermal and electric performance. This characteristic,

and the ability to be molded and adapted has rapidly increased their use over the last decades, having applications in compact electronic devices [16], conducting adhesives [17], anti-static materials [18], electromagnetic shielding [19,20], among others [3,21,22]. Heat and electronic transport in these systems are complex phenomena that depend on many factors, such as the thermal properties of the matrix and the fillers, their concentration, distribution, orientation, size, and shape, as well as on the matrix-filler thermal resistance [9].

As the concentration of fillers increases and reaches a threshold, the physical properties of composites can exhibit significant changes due to the formation of conducting networks [140]. This connectivity of the composite fillers is described as percolation, which usually shows up for sizeable differences between the physical properties of the matrix and fillers [141]. For instance, when a composite with an insulating matrix is progressively filled with conductive fillers, there will be a certain volume fraction of fillers, known as percolation threshold (v_p), at which the composite will become conductive [142].

Several studies have been carried out to investigate the thermal and electrical properties of composites, in order to establish the percolation threshold dependence [142–146]. The electric percolation threshold (v_{pE}), can be found more easily compared with the thermal percolation threshold (v_{pT}), the principal reason is due to the variations on the increase of the electrical conductivity are much larger compared to the thermal conductivity, due to the greater contrast between the conductivity values of the matrix and the fillers [147, 148]. Theoretically, the threshold percolation can be estimated by means of the excluded volume percolation theory [149], as follows:

$$v_p(AR) = \frac{v_{ex}}{\frac{4\pi}{3} + 2\pi(AR) + \frac{\pi}{2}(AR)^2}\left[\frac{\pi}{6} + \frac{\pi}{4}(AR)\right] \tag{5.1}$$

Where v_{ex} is the excluded volume and AR is defined as the ratio between length and aspect ratio [144], in the case of spheres $v_{ex} = 2.8$, AR=1 and $v_p(AR) = 0.30$. Experimentally, it has been found that the threshold of percolation in some cases does not take the same value for the electrical and thermal conductivity, as predicted by equation (5.1). Yin *et al.* found a difference of 1.5% between the percolation threshold electrical and thermal on composites

sintered of graphene platelets and aluminum nitride [143]. Kim *et al.* in 2013 reported a difference of 4% (in-plane) for anisotropic composites of CNTs dispersed on reactive ethylene terpolymer (RET) [150]. Kim *et al.* in 2011 dispersed MWCNTs on RET found a difference of 10% [144]. Kwon *et al.* reported for composites of MWCNTs and poly(dimethylsiloxane) a difference of 25% [145].Finally, Sun *et al.* studied dispersed copper particles (Cu) inside an ytirium iron garnet (YIG) matrix, in this case the difference was around 27% [146].

5.2 Samples preparation

The composites were prepared by gently dispersing carbonyl-iron particles (CIP) in a polyester resin matrix (RP RESINMEX). The liquid composite was then mechanically mixed for 15 minutes, in order to obtain a homogeneous mixture, which was afterwards sonicated with an ultrasonic tip (Sonics Vibra-Cell at 65 W, 20 KHz) for 2 minutes. To accelerate the polymerization, a catalyst was next added and mixed slowly for 30 seconds. Finally, the sample was deposited in a cylindrical plastic cast. After polymerization, the samples were cut in plates and polished until their diameters and thicknesses were reduced to about 2 cm and 1 mm, respectively. These dimensions are suitable for the thermal characterization in our experimental set-up. In order to improve the light absorption and the IR emissivity, each sample was painted with a thin layer (around 50 μm) of matte black paint.

Twelve particles concentrations were prepared and tested: 0, 0.05, 0.12. 0.27, 0.30. 0.33, 0.36, 0.38, 0.41, 0.45, 0.50 and 0.55 vf of CIP. Figure 5.1(a)-(e) shows SEM images of some structures formed by the CIP particles, along with a representative histogram of their size distribution. Note that the particles exhibit a random spatial distribution inside the matrix, and an average diameter of 1.67 $\pm$ 0.87 μm.

5.3 Theoretical models

It has been demonstrated that the thermal diffusivity and thermal effusivity can be determined simultaneously in solids by assembling and analyzing the heat transport of a two-layer

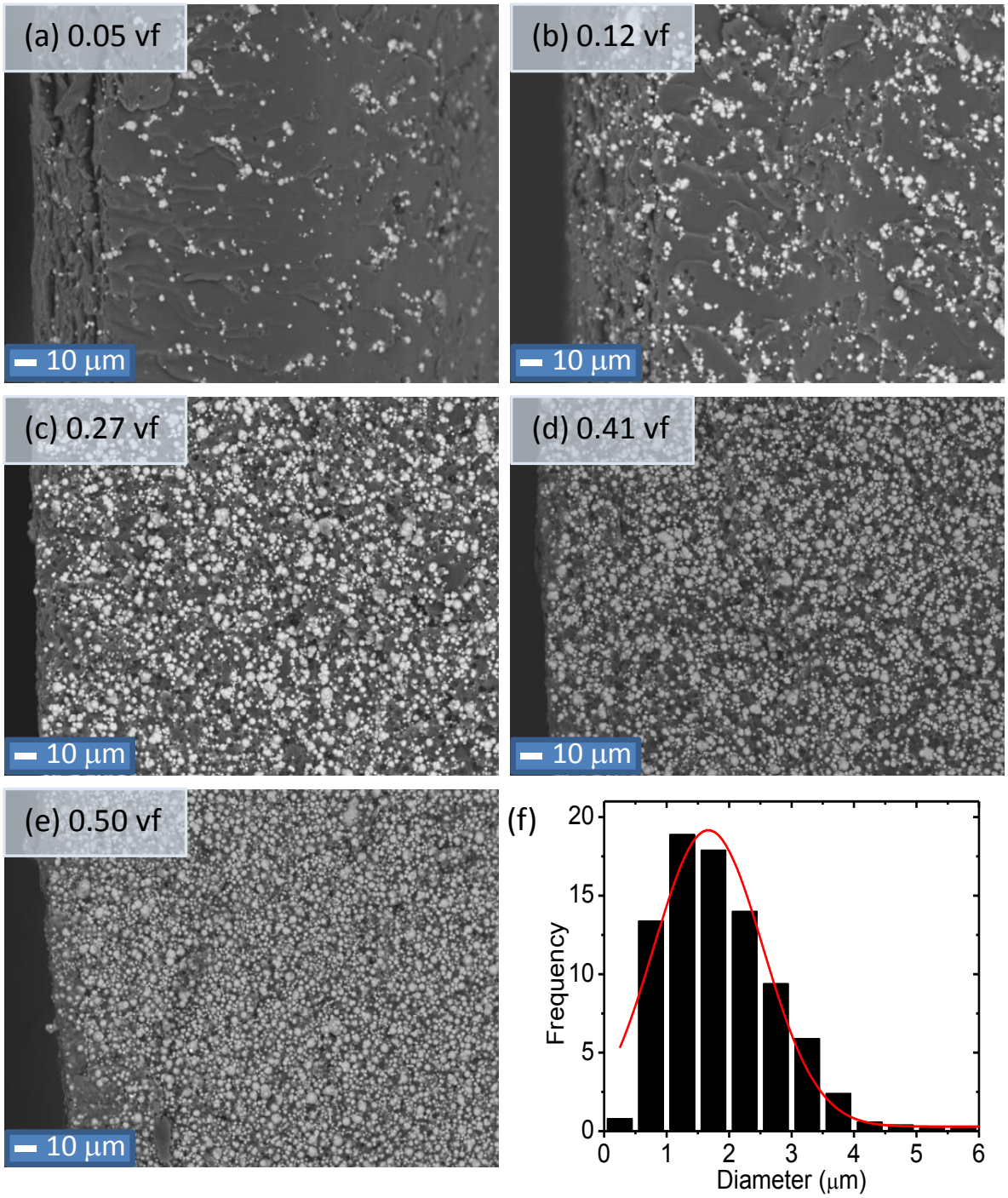

Figure 5.1: SEM images of a composite with a particles concentration of (a) 0.05 (b) 0.12, (c) 0.27, (d) 0.41, and (e) 0.50 vf. All the SEM images were presented at 500X. f) Histogram showing the size distributions of particles.

system [128]. The system consists of a solid of thickness L with a semi-infinite liquid backing, heated by a homogeneous light pulse of intensity Q at $z = 0$ (the details will be discussed below). However, a major restriction is always the lack of contrast between the thermal effusivity of the two materials [128]. The liquids used to make the thermal contrast have thermal effusivities between 500 and 1750 $\mathrm{Ws^{1/2}m^{-2}K^{-1}}$ and for the polyester resin thermal effusivity values of 550 $\mathrm{Ws^{1/2}m^{-2}K^{-1}}$ have been reported [74]. Because the thermal effusivity increases when CIP particles are inserted, for some concentration the thermal effusivity of both the solid and the liquid will coincide, which does not allow to obtain simultaneously the thermal diffusivity and thermal effusivity as it will be shown in section 5.3.3. To avoid this restriction, we opted to measure first the thermal diffusivity using a model of a slab A.2.4 and then the thermal effusivity was determined by means a two-layer system with a semi-infinite fluid backing A.2.5, using the value of thermal diffusivity previously obtain. The behavior of the temperature as a function of time and its dependence on the thermal properties of the polymer and backing fluid will be explored below.

5.3.1 Measurement of the thermal diffusivity

Figure 5.2 shows the geometry of an opaque slab of thickness L, illuminated by a uniform heating pulse Q for a short time, with thermal diffusivity α and thermal effusivity ϵ_s, as shown in figure A.5. The corresponding Laplace transform of the temperature rise at the front surface ($z = 0$) was calculated in the section A.2.4 (equation A.38) and is presented again below

$$\theta(0) = \frac{\bar{I}_0 \chi}{\epsilon_s} \frac{\sqrt{s} + h_p \tanh(x\sqrt{s})}{2h_p\sqrt{s} + (s + h_p^2)\tanh(x\sqrt{s})}, \tag{5.2}$$

which was obtained considering adiabatic boundary conditions: $\phi(0, s) = \bar{I}_0 \chi S$ and $\phi(L, s) = 0$. Here χ is the energy fraction absorbed by the front surface, s is the Laplace parameter, $x = L/\sqrt{\alpha}$, $h_p = h/\epsilon_s$, and h is the heat transfer coefficient by convection from the solid surfaces in contact with air. $\bar{I}_0$ represents the Laplace transform of the light pulse. Its Laplace transform is $\bar{I}_0 = Q$, being Q the energy per unit area ($\mathrm{Jm^{-2}}$) delivered by the pulse.

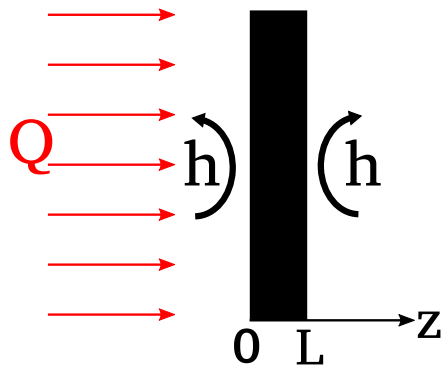

Figure 5.2: Schemes of the configuration used for performing the thermal diffusivity characterization of our composites. The composite of thickness L is subjected to a short pulse of light of intensity Q, at $z = 0$, whose temperature evolution with time is recorded. The factor h represents the heat losses by convection.

Equation (5.2) depends on the three parameters $Q\chi/\epsilon_s$, x and h_p, which can therefore be determined by numerically fitting the obtained inverse Laplace transform of equation (5.2) to its corresponding experimental data. The thermal diffusivity $\alpha = L^2/x^2$ is then calculated for a sample of known thickness L and x.

Figure 5.3 shows the evolution of the temperature after a heat pulse. For the simulations a typical value for convection heat losses of 10 $\mathrm{Wm^{-2}K^{-1}}$ and a heat pulse of $1{\times}10^3$ $\mathrm{Jm^{-2}}$ has been used. The thickness of the sample has been set to 800 μm. The effect of the thermal diffusivity is explored on the figure 5.3a. The characteristic time $\tau = L^2/(\pi\alpha)$, gives a measure of the time that it takes for the heat to propagate through a slab after exciting with a Dirac like pulse, which appears in the form of an elbow. Three values of diffusivity have been plotted: 0.1, 0.2 and 0.3 $\mathrm{mm^2s^{-1}}$, and it can be seen that as the thermal diffusivity increases, the time in which the pulse of heat reaches the other side of the sample decreases. The thermal effusivity was fixed in 1200 $\mathrm{Ws^{1/2}m^{-2}K^{-1}}$. On the other hand, the effect of the thermal effusivity is presented on figure 5.3b. Three values of thermal effusivity have been plotted: 600, 1200 and 2000 $\mathrm{Ws^{1/2}m^{-2}K^{-1}}$, and it can be seen that as the thermal effusivity increases, the surface temperature reached in the sample is lower. The thermal diffusivity

was fixed in 0.2 mm^2s^{-1}.

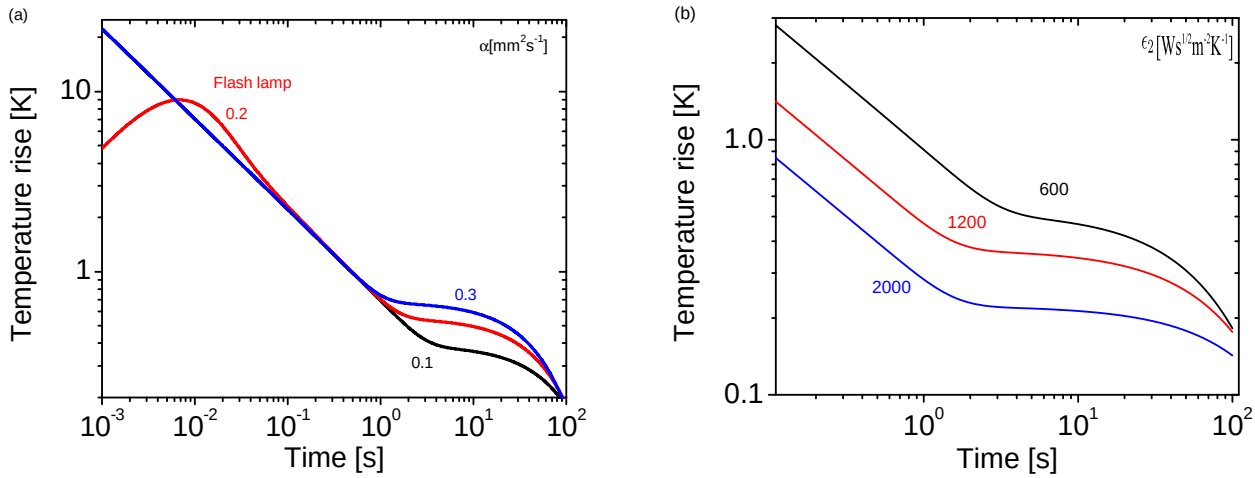

Figure 5.3: Surface temperature evolution of a slab. a) The effect of the thermal diffusivity is explored. The thermal effusivity was fixed in 1200 $Ws^{1/2}m^{-2}K^{-1}$. The effect of the flash lamp is shown with a red line. b) Effect of the thermal effusivity on the temperature. The thermal diffusivity was fixed in 0.2 mm^2s^{-1}

5.3.2 Measurement of the thermal effusivity

Consider a sample that is now in contact with a semi-infinite liquid backing of thermal effusivity ϵ_f. The surface at $z = 0$ is uniformly heated up by a light pulse of intensity Q, as shown in figure 5.4. The corresponding Laplace transform of the temperature rise at the front surface ($z = 0$) was calculated in the section A.2.5 (equation A.44) and is presented again below

$$\theta(0) = \frac{\bar{I}_0\chi}{\epsilon_s\sqrt{s}} \frac{\cosh(x\sqrt{s}) + b_{21}\sinh(x\sqrt{s})}{\left(b_{21} + \frac{h_p}{\sqrt{s}}\right)\cosh(x\sqrt{s}) + \left(1 + \frac{h_p b_{21}}{\sqrt{s}}\right)\sinh(x\sqrt{s})}, \tag{5.3}$$

which was obtained considering adiabatic boundary conditions: $\phi(0,s) = \bar{I}_0\chi S$ and $\phi(L,s) = 0$; here χ is the energy fraction absorbed by the front surface, $b_{21} = \epsilon_f/\epsilon_s$, and h is the heat transfer coefficient by convection from the illuminated surface to air. $\bar{I}_0$ represents the Laplace transform of the light pulse. Taking into account that x is a known parameter, the values of

the other three unknown ones $Q\chi/\epsilon_s$, b_{21} and h_p in equation (5.3) can be extracted by fitting the inverse Laplace transform of equation (5.3) to the corresponding experimental data. The sample thermal effusivity $\epsilon_s = \epsilon_f/b_{21}$ is then determined, provided that the thermal effusivity of the backing liquid is known. Note that equation 5.3 does not reduce to equation 5.2 when the liquid backing is replaced by air, because of the different convection contributions, as shown in figures 5.2 and 5.4. The inverse Laplace transforms of equations 5.2 and 5.3 were numerically calculated by means of the well-known Euler algorithm and fitted to the measured experimental data [151]. The fittings were done by using the least-squares fitting procedure based on the Levenberg-Marquardt algorithm [132, 133].

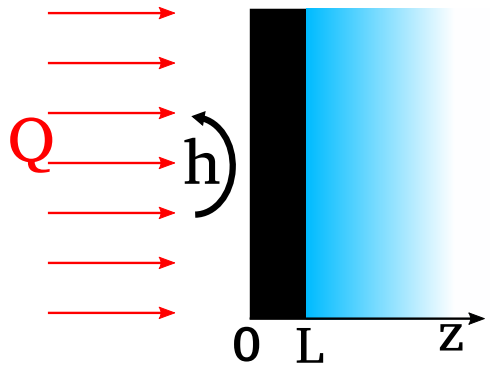

Figure 5.4: Diagram representing an opaque solid of thickness L with a semi-infinite liquid backing.

Figure 5.5 shows the effect of thermal diffusivity and thermal effusivity on temperature after a heat pulse. For the simulations a typical value for convection heat losses of 10 $\mathrm{Wm^{-2}K^{-1}}$, a 1 $\mathrm{kJm^{-2}}$ Dirac like pulse and $h = 10$ $\mathrm{Wm^{-2}K^{-1}}$, and the thickness of the sample has been set to 800 μm. Figure 5.5a shows the effect of the thermal diffusivity on the temperature evolution. Three values of α have been considered: 0.1, 0.3 and 0.6 $\mathrm{mm^2s^{-1}}$. The time that the heat takes to propagate through a slab after exciting with a Dirac like pulse ($\tau_1 = L^2/(\pi\alpha)$) decreases as the thermal diffusivity increases. The thermal effusivity was fixed in 800 and 1500 $\mathrm{Ws^{1/2}m^{-2}K^{-1}}$ for the solid and the backing fluid respectively. From elsewhere, figure 5.5b shows the effect of thermal effusivity. If the thermal effusivity of the slab equals to one of the fluid ($\epsilon_f = \epsilon_s = 900$ $\mathrm{Ws^{1/2}m^{-2}K^{-1}}$), there is no thermal mismatch

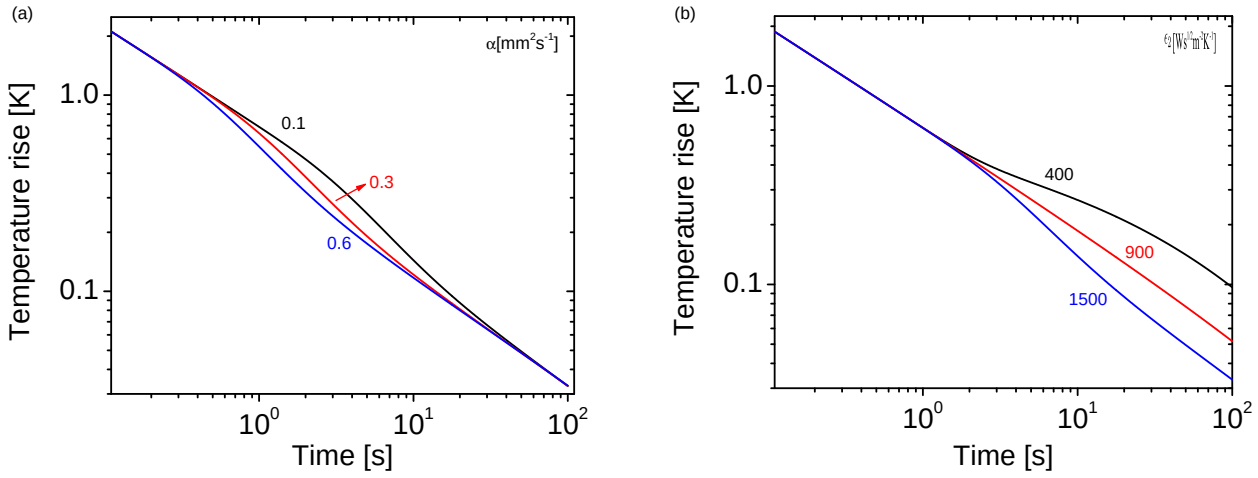

Figure 5.5: Surface temperature evolution of a two-layer system as a function of time. a) The effect of the thermal diffusivity of sample is explored. The thermal effusivity was fixed in 800 and 1500 $\mathrm{Ws^{1/2}m^{-2}K^{-1}}$ for the solid and the backing fluid, respectively. b) Effect of the thermal effusivity of the backing fluid. The thermal effusivity and thermal diffusivity of the solid sample was fixed in 0.1 $\mathrm{mm^2s^{-1}}$ and 900 $\mathrm{Ws^{1/2}m^{-2}K^{-1}}$ respectively.

at their interface and heat flows as in a semi-infinite sample (T is a straight line with $-1/2$ slope) until it reaches the backing surface $z = L$. For liquids with thermal effusivity lower than that of the slab ($\epsilon_f < \epsilon_s$), the thermal energy transferred to the liquid is smaller than that delivered by the solid sample. This explains the temperature rise above the line of $-1/2$ slope for $t > \tau_1$. The opposite occurs for $\epsilon_f > \epsilon_s$, $T(0)$ shows a downwards displacement from the line of $-1/2$ slope for $t > \tau_1$. Three values of effusivity have been plotted: 400, 900 and 1500 $\mathrm{Ws^{1/2}m^{-2}K^{-1}}$. The thermal diffusivity was fixed in 0.1 $\mathrm{mm^2s^{-1}}$.

5.3.3 Sensitivity analysis

In section 2 was indicated that thermal effusivity and conductivity cannot be extracted simultaneously from the two-layer system, then a sensitivity analysis will be made to show the restriction occurs when there is no contrast in the effusivities. The local sensitivity of T to a given parameter $\beta = \{x, b_{21}\}$ is defined as [129]:

$$Sy(\beta) = \frac{\beta}{T}\frac{\partial T}{\partial \beta}. \tag{5.4}$$

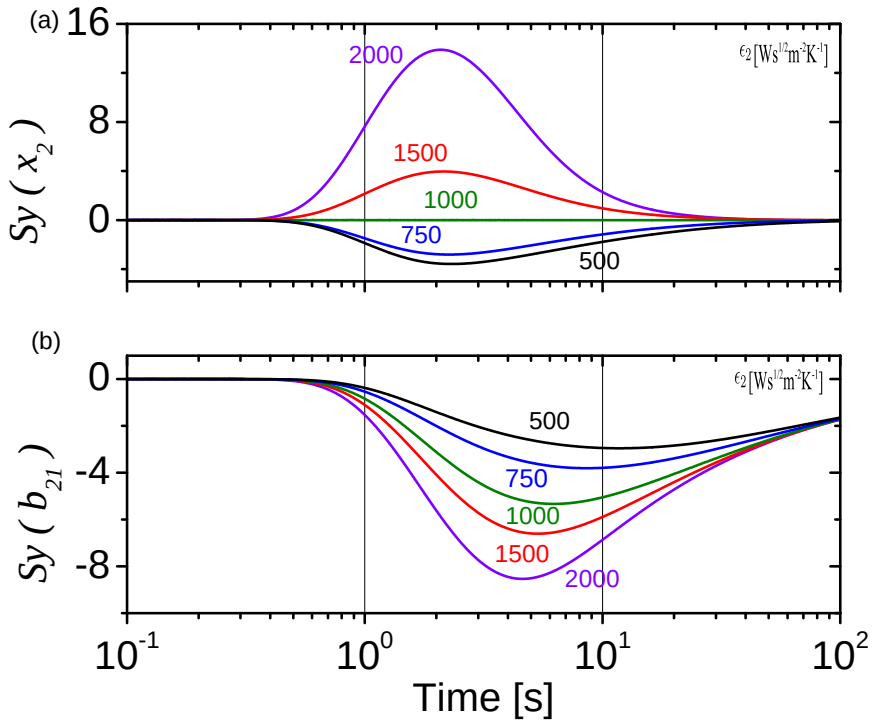

Figure 5.6: Sensitivity curves of the surface temperature $T(0)$ evolution to (a) x and (b) b_{21}. Several values of the thermal effusivity ϵ_f have been analyzed in order to explore the applicability of the method. Thermal diffusivity has been fixed to 0.3 mm^2s^{-1} in all simulations.

Simulations shown in figure 5.6 have been performed considering a 1 kJm^{-2} Dirac like pulse and $h = 10$ $Wm^{-2}K^{-1}$. The thermal diffusivity, thermal effusivity and the thickness of the sample has been fixed in 0.3 mm^2s^{-1}, 1000 $Ws^{1/2}m^{-2}K^{-1}$ and 1 mm, respectively. Simulations in figure 5.6a shows the sensitivity of temperature to the parameter x as a function of time. The maximum sensitivity shifts to earlier times as the thermal effusivity decreases. Additionally, there is no sensitivity when the thermal effusivity of the slab equals the one of the fluid ($\epsilon_s = \epsilon_f = 1000$ $Ws^{1/2}m^{-2}K^{-1}$). Sensitivity to the ratio of thermal effusivities b_{21} for several values of is shown in 5.6b. Notice that the maximum sensitivity to b_{21} always shifts to earlier times as ϵ_f increases. In conclusion, since for some concentrations of particles the

thermal effusivities will coincide, it is necessary first to measure the thermal diffusivity using a model of a slab and then determine the thermal effusivity by means of a two-layer system with a semi-infinite fluid backing. During the fittings, the parameter corresponding to the thermal diffusivity was fixed to the experimentally value obtained previously.

5.4 Experimental setup

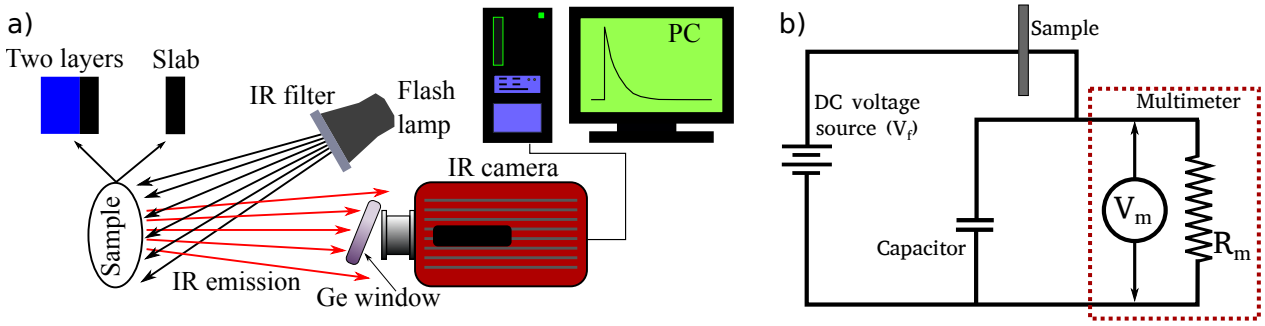

Figure 5.7: Experimental setup used in our measurements. a) Scheme of the experimental setup used to obtain the thermal conductivity. Samples are heated up by a flash lamp and the temporal evolution of the temperature is recorded by means of an infrared camera. An infrared filter is placed between the flash lamp and the sample to prevent that the IR radiation of the lamp reaches the sample surface. Furthermore, the camera lens is protected with a Ge window placed in front of the camera. b) Scheme of the experimental setup used to obtain the electrical conductivity. Samples are placed in series with a voltmeter of high impedance. A capacitor (0.2μF) in parallel with the voltmeter is placed, in order to filter out any interference that may affect the high impedance of the voltmeter.

The experimental setup used to measure the thermal and electrical properties of our composites is shown in figure 5.7. The only differences in the experimental setup used for the thermal characterization (figure 5.7b), with respect to the previous chapter (see section 4.5), consist of the type of samples and that images are recorded at a rate of 250 frames per second. The experimental setup used to measure the electrical conductivity of our composites is shown in figure 5.7(b). On each composite, of resistance R, a pair of electrodes are attached

by means of colloidal silver paint (SPI Supplies), in order to have good contact. Then the composite is placed in series with a multimeter (Fluke 79 series III), which must be connected as a voltmeter mode, in order to measure voltage. The DC source voltage (Keithley 2231A-30-3) V_f drops in the internal resistance R_m=11.11 MΩ of the multimeter and in the sample of resistance R. The voltage V_m is read from the voltmeter and correspond to the internal resistance. The resistance of the sample R is obtained by means of,

$$R = R_m \frac{V_f - V_m}{V_m}. \tag{5.5}$$

The DC source voltage (V_f) was operated in a range from 30 to 40 V and a capacitor of 0.2μF was used. The value of the electrical conductivity is determined by means of the size of the sample and the resistivity measured, namely $\sigma = L/(RA)$, where L is the thickness of the sample and A is the cross-sectional area.

5.5 Results and discussion

5.5.1 Thermal diffusivity

Figure 5.8(a) shows the experimental cooling curves of three representative samples along with their corresponding fitting curves established by equation 5.2. One out of ten experimental data points are plotted. The residuals obtained for the fitting of the parameters $Q\chi/e_s$, $x = L^2/\alpha^2$ and $h_p = h/e_s$ are smaller than 2%, which indicates that the fits are highly accurate, confirming the good agreement between the experimental and theoretical results. The time evolution of temperature exhibits a clear change of slope at earlier times for higher volume fractions. The time at which this "characteristic elbow" occurs, represents the time required by the heat flux to propagate through the whole sample of thickness L, and is given by $\tau = L^2/(\pi\alpha)$ [62]. Given that all measured samples have the same thickness, the thermal diffusivity α is thus expected to increase with the volume fraction of particles.

Figure 5.8(b) shows the experimental values of the thermal diffusivity as a function of the volume fraction vf of CIP. Each experimental point has been obtained from the average of five

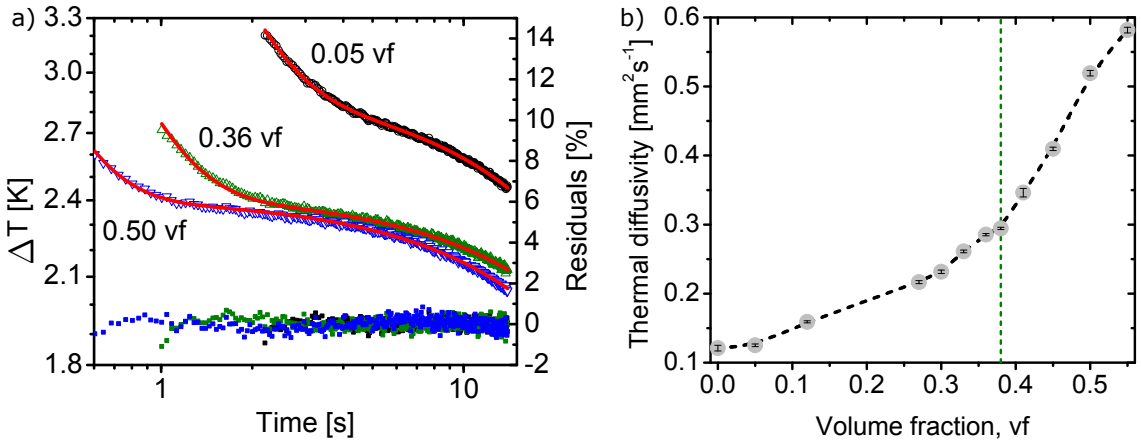

Figure 5.8: a) Experimental and fitted cooling curves used to measure the thermal diffusivity of three representative samples. Markers represent the experimental data and continuous lines the best fittings. The corresponding residuals of each fit are plotted using dots in the secondary scale. b) Thermal diffusivity of polyester resin/CIP composites as a function of the fillers volume fraction. Dots represent the experimental data, the dashed black line is a visual guide and the vertical line at vf = 0.38 stands for the thermal percolation threshold.

measurements. For low concentrations of CIP (vf < 0.38), the expected increase of α with vf is in fairly good agreement with those reported by Sofian *et al.* [152] and Rusu *et al.* [153], such as an increase of 1.2 times that is reached with a 0.12 vf. For high concentrations (vf > 0.38), on the other hand, the values of α are smaller than those reported by these latter authors, maybe due to the differences on the particles sizes, whose impact on α is expected to strengthen as vf increases. The maximum thermal diffusivity value measured at the highest concentration consider in this work (0.55 vf) is 4.8 times that of the matrix. More over, the rate of change of α for vf > 0.38 is higher than for vf < 0.38, which indicates that the thermal percolation of our composites appears at vf $= 0.38$.

5.5.2 Thermal effusivity

The typical cooling curves obtained for our samples in contact with a semi-infinite liquid backing are shown in figure 5.9(a), for the three representative volume fractions of 0.05, 0.36 and 0.50. One out of ten experimental data points is plotted along with their fitting curves.

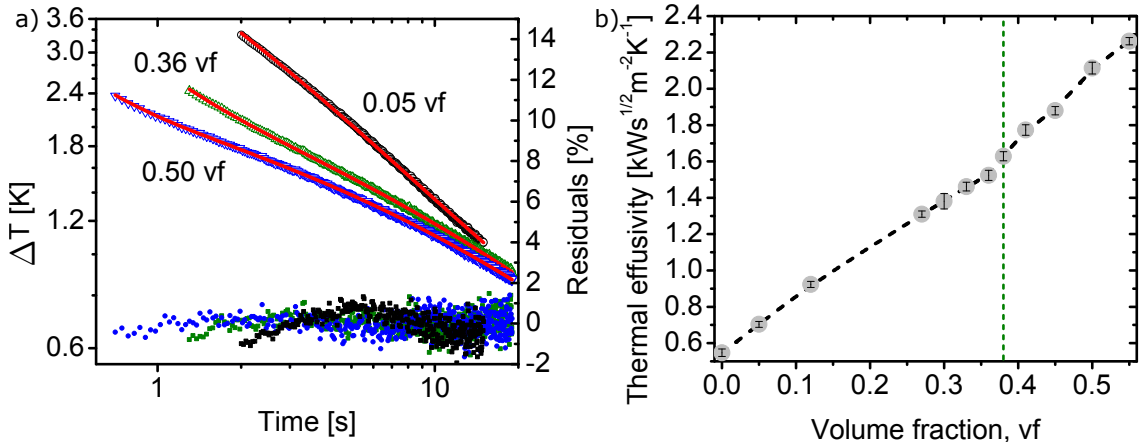

Figure 5.9: a) Cooling curves used to measure the thermal effusivity of composites with concentrations of 0.05, 0.36 and 0.50. Symbols represent the experimental data and continuous lines their best fittings. Fitting residuals are also plotted in dots. b) Thermal effusivity of polyester resin/CIP composites as a function of the volume fraction of fillers. Dots represent the experimental data, the dashed black line is a visual guide, and the vertical green line stands for the thermal percolation threshold.

The residuals obtained for the fitting of the parameters $Q\chi/e_s$, $b_{21} = e_f/e_s$ and $h_p = h/e_s$ are smaller than 2%, which indicates that retrieved values are highly accurate. The backing fluid was ethylene glycol with a thermal effusivity of 858 $\mathrm{Ws^{1/2}m^{-2}K^{-1}}$ [72]. For times smaller than the diffusion one ($t < \tau = L^2/(\pi\alpha)$), the logarithmic plot of the surface temperature evolution exhibits a slope $m = -0.5$, in agreement with previous reported works [62, 128]. For long times ($t > \tau = L^2/(\pi\alpha)$), on the other hand, the temperature behavior becomes sensitive to the interface between the sample and backing, and therefore its slope is driven by the ratio of their thermal effusivities. For $e_s < e_f$ ($e_s > e_f$), the slope $m < -0.5$ ($m > -0.5$), such that $m = -0.5$ for $e_s = e_f$. This fact along with figure 5.9(a) indicate that the sample with 0.05 vf (0.50 vf) has a thermal effusivity smaller (greater) than that of ethylene glycol, while the sample with 0.36 vf has an intermediate thermal effusivity, as expected.

Figure 5.9(b) shows the experimental values of the thermal effusivity as a function of the volume fraction of CIP. Each experimental point has been obtained from the average of five measurements. The increase of the thermal effusivity with the fillers concentration

is fairly linear for concentrations lower and higher than the thermal percolation threshold (v_{pT}=0.38) of the thermal diffusivity shown in figure 5.8(b). The maximum enhancement of the thermal effusivity reached in this work was 4.1 times that of the matrix, for the maximum concentration consider (0.55 vf). Given that the thermal effusivity is an indicator of the amount of heat that the polymeric composite can transfer to the environment, its obtained variations is paramount for the design and operation of heat exchangers.

5.5.3 Volumetric heat capacity

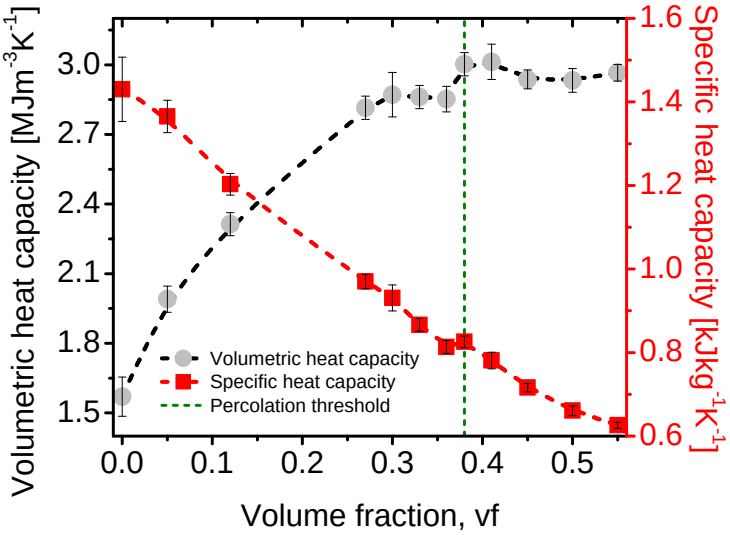

Figure 5.10: Volumetric heat capacity (gray dots) and the specific heat capacity (red squares) versus volume fraction concentration of filler. Gray dots represent the experimental data for volumetric heat capacity. In both cases, the dashed line is only a visual guide. The green dashed vertical line represents the thermal percolation threshold.

The dependence of the volumetric heat capacity C_v and the specific heat capacity C as a function of volume fraction are shown in figure 5.10. The values of C_v (represented by gray dots) are determined by means of the experimental data of ϵ and α and the relationship $C_v = \epsilon/\sqrt{\alpha}$. The values of C (represented by red squares) are obtained from the values of C_v and the density ρ of the composite and the relationship $C = C_v/\rho$. The composite density

is determined through the relationship $\rho = \rho_m(1 - \text{vf}) + \rho_f \text{vf}$, with $\rho_m = 1160$ kgm^{-3} and $\rho_f = 7870$ kgm^{-3} [154]. The uncertainty of C_v was properly determined by using the ones of ϵ and α [139]. Note that the values of C_v increases rapidly at low concentrations and saturate for high enough ones. The maximum enhancement of C_v was around 1.9 times that of the matrix, for vf > 0.30. On the other hand, C decreases as the fillers concentration increases, as was reported for similar fillers [152, 153]. The maximum reduction of C_v found in this work was about 0.42 times the one of the matrix at 0.55 vf.

5.5.4 Thermal conductivity

Figure 5.11 shows the thermal conductivity $k = \epsilon\sqrt{\alpha}$ (gray points) of our composites as a function of concentration of CIP. The red line represents the second derivate of k and its maximum determines the thermal percolation threshold $v_{pT} = 0.38$, which is represented by the green dashed line and coincides with that of α shown in Fig.5. For vf $> v_{pT}$, k increases faster than for vf $< v_{pT}$, due to the formation of heat transmission networks among the particles, at high concentrations, as shown in figure 5.1. Note that the experimental values are well predicted by the Zhang model [155], which establishes that the effective thermal conductivity of composites with a percolation threshold v_{pT} is given by

$$k = k_f \left[\frac{k_p}{k_f}\right]^{\left[\frac{1-\text{vf}}{1-v_{pT}}\right]^n}. \tag{5.6}$$

where $k_p = k(v_{pT})$, k_f is the thermal conductivity of the fillers, which in our case is $k_f = 80.2$ Wm^{-1}K^{-1} [25], and $n = 0.54$ is a percolation exponent determined by fitting. This parameter depends on the filler size, shape, and distribution on the composites and the range studied. The maximum enhancement of k was 9.1 times that of the matrix, for a 0.55 vf.

In contrast to the behavior of C (figure 5.10), the experimental values of k showed in figure 5.11 do not display a saturation, as was reported by Elimat *et al.* [156], but rather it tends to increase exponentially, after crossing the percolation threshold, which is consistent with the data reported by Sofian *et al.* [152] and Rusu *et al.* [153]. For a concentration of 0.12 vf, the thermal conductivity increases 1.9 times that of the matrix. Although greater

increments of k would be expected for fillers with a thermal conductivity higher than the CIP used in this work, the effects of their shape and size should also be taken into account. For instance, by using aluminum fillers with a thermal conductivity 3 times greater than iron and an average diameter of 44 μm, Boudenne *et al.* [157] obtained similar increments than the ones reported in this work, involving CIP with a mean diameter of 1.67 μm.

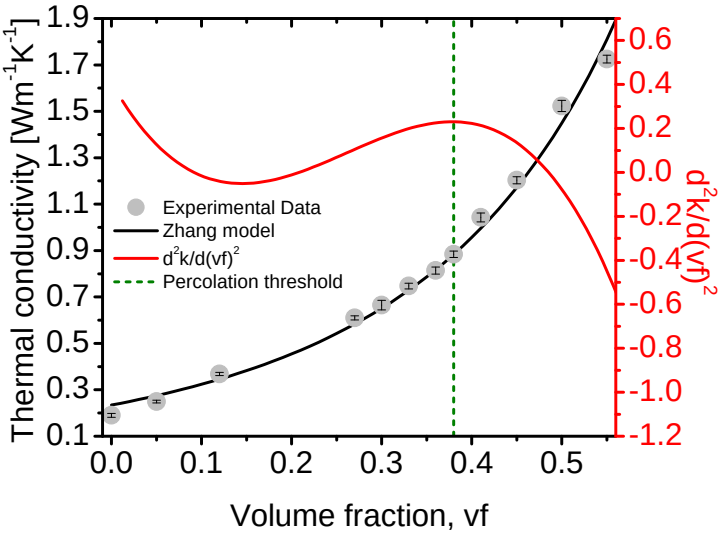

Figure 5.11: Thermal conductivity k and its second derivate as functions of the volume fraction of fillers. The gray points represent the experimental data, while the predictions of Zhang model (equation (5.6)) are represented by the black line. The maximum of the second derivative stands for the thermal percolation threshold of k.

5.5.5 Electrical conductivity

Figure 5.12 shows the electrical conductivity as a function of the concentration of CIP. Each experimental point has been obtained from the average of five measurements and is represented by a gray point. The red line represents the second derivate of the electrical conductivity σ and its maximum represents the electrical percolation threshold $v_{pE} = 0.46$, which is shown as a green dashed line. A trend line corresponds to the fitting of a statistical-thermodynamic model (sigmoidal-Boltzmann curve) in accordance with the fitting proposed

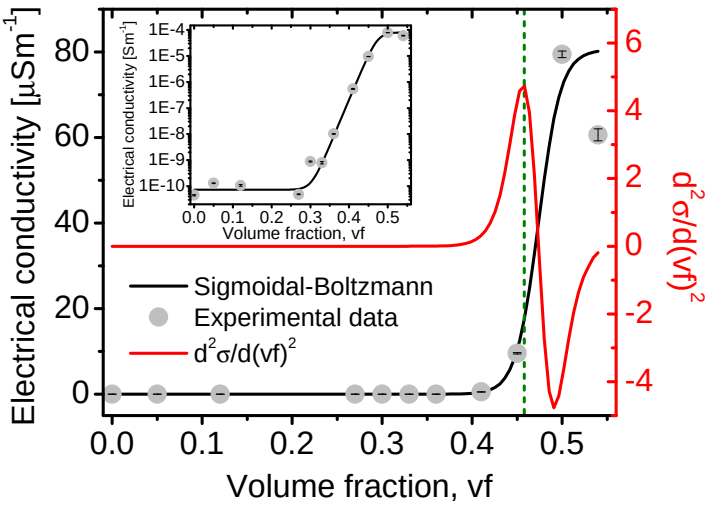

Figure 5.12: Electrical conductivity σ and its second derivate as functions of the volume fraction of fillers. The gray points represent the experimental data. The maximum of the second derivative stands for the electrical percolation threshold of σ.

by Rahaman [158] and Merzouki [159].

$$\sigma = \frac{A_1 - A_2}{1 + \exp[(\mathrm{vf} - v_{pE})/(\Delta x)]} + A_2. \tag{5.7}$$

The parameters $A_1 = 5.26 \times 10^{-11}\mathrm{Sm}^{-1}$, $A_2 = 8.09 \times 10^{-5}\mathrm{Sm}^{-1}$, $\Delta x = 0.012$ and $v_{pE} = 0.46$ are obtained by means of curve fitting. An inset in the figure 5.12 is added in order to show the changes on the electrical conductivity for all the concentrations. For volumetric fractions between 0 and 0.27 no appreciable changes on the electrical conductivity were observed. The average value for the electrical conductivity in this region was $8.2{\times}10^{-11}\mathrm{Sm}^{-1}$, which is a typical value for polyester resin [160, 161]. On the other hand, the electrical conductivity has a rapid increase for volumetric fractions above 0.27, reaching a value of $8{\times}10^{-5}\mathrm{Sm}^{-1}$ for a 0.5 vf, corresponding to an increase of 6 orders of magnitude respect to the matrix. Similar increments have been reported by Merzouki for polypropylene matrices with carbon black and acetylene black particles [159] and Genetti *et al.* for microparticles of nickel dispersed on low-density polyethylene (LDPE) [162]. The behavior of the electrical

conductivity presents the characteristic s-shape, showing the three characteristic regimes [163]: the insulator (0 to 0.27 vf), percolative (0.30 to 0.50 vf) and conductive (above 0.5 vf).

The ratio between the thermal conductivity and the electrical conductivity as a function of volume fraction are shown in figure 5.13. The experimental points are derived from the values of k and σ, and is represented by gray points. The red line is obtained by means of equations (5.6) and (5.7), with the parameters previously obtained. The behavior of the curve is mostly determined by the electrical conductivity, due to the high changes with respect to thermal conductivity. The Wiedemann-Franz law relates the thermal and electrical conductivity as follows [164]:

$$L = \frac{k}{\sigma T} = \frac{\pi^2}{3}\left(\frac{k_b}{e}\right)^2 = 2.45 \times 10^{-8} \mathrm{W\Omega K^{-2}}. \tag{5.8}$$

Where L is called the Lorentz number, T the absolute temperature, k_b the Boltzmann constant and e the electron charge. In our case, L can be obtained by means of the experimental data. This values are in the range of 64 to 4.21×10^7 $\mathrm{W\Omega K^{-2}}$, as is shown in figure 5.6. This difference is due to the fact that the Wiedemann-Franz law assumes a free electron gas model for the charge carriers and the transport mechanisms on the polymer filled with CIP involved molecular vibrations and electronic conduction.

An important aspect, is the shift between the thermal ($v_{pT} = 0.38$) and electrical percolation threshold ($v_{pT} = 0.46$), this difference is around of 20 % and these values differ from the value estimated by equation (5.1). This shift can be explained due to the differences in the transport mechanisms involved in the electrical and thermal conduction. On the electrical conductivity, the electron transport occurs principally through three mechanisms: resistive, quantum tunneling and percolative [165,166]. For low concentrations, the conductivity of the polymer is controlled only by the resistivity of the matrix, that is resistive. As the volumetric fraction increases, the separation between the conductive particles becomes smaller, and for separations less than 10 nm, the electrons can be transported between conductive particles by means of a mechanical tunnel effect, which in combination with the resistive mechanism

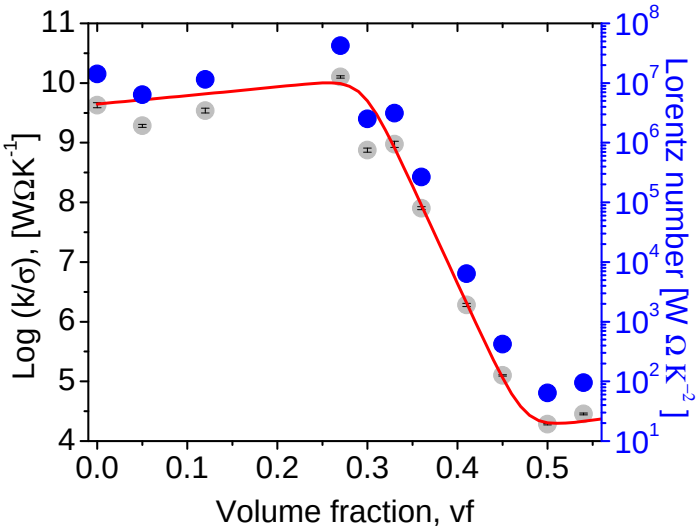

Figure 5.13: Ratio between the thermal conductivity and the electrical conductivity, and Lorentz number as a function of volume fraction. The gray points represent the experimental data and the red line is obtained by means of the equations (5.6) and (5.7).

increases the electrical conductivity. Finally, at high concentrations the percolative transport dominates. Macroscopic chains of conductive material are formed, facilitating the transport of electrons; when this mechanism occurs, the greatest changes in conductivity are observed. On the other hand, for the heat transfer, two mechanisms are considered: phononic and electronic conduction [146]. In the matrix, the thermal conductivity is determined by the vibrations of the phonons, but as the concentration of particles increases and the formation of networks occurs, the electronic contribution becomes important, due to the possibility of the electrons to move through these paths. This shift also is present in other ways of percolation, for example, Shi *et al.* reported differences between the percolation threshold of electromagnetic interference shielding and the percolation threshold of electrical conduction [167]. This kind of polymer presents favorable conditions for its application in electronic devices due to the fact that the electrical and thermal thresholds do not match, then an enhancement in heat dissipation is presented but electrical insulation remains so high to protect of a short circuit.

5.6 Summary

The thermal and electric percolation of composites made up of carbonyl iron microparticles embedded in polyester resin matrix has experimentally been observed. A clear thermal conductivity percolation threshold was observed at v_{pT}=0.38 and the electrical percolation threshold at v_{pE}=0.46. The shift between both thresholds is 20%, which can be explained due to the differences in the transport mechanisms involved in the electrical and thermal conduction. The behavior of thermal conductivity was satisfactorily modeled by Zhang's model. On the other hand, the increase on electrical conductivity tends to be sigmoidal, allowing it to be modeled by a logistic Boltzmann curve. The electrical conductivity presents the characteristic s-shape, showing the three typical regimes: the insulator, percolative and conductive. The Wiedemann-Franz law does not allow to obtain an adequate value of Lorentz number because the transport mechanisms considered in its formulation are different from those that exist on our composites. The obtained results could be useful for the development of the next generation of efficient thermal interface materials.

Conclusions

In the present work, the thermal characteristics of magnetorheological and polymeric fluids with inclusions of particles were studied, by means of the thermal wave resonance cavity (TWRC) and infrared thermography (IRT), respectively. On the other hand, the flash technique was extended to characterize fluids. After this work we can conclude:

Magnetorheological fluids: thermal conductivity and its relationship with the viscosity

- It has been shown that magnetorheological fluids can experience considerable increments in thermal conductivity when an uniform magnetic field is applied.
- The increase on thermal diffusivity and thermal conductivity in MR materials is due to the formation of chains that facilitate the transport of thermal energy.
- The viscosity plays an important role, since when the fluid is more viscous the formation of chains becomes slower, therefore the increases in the thermal properties are also slower.
- It has been shown that the induced alignment and its stability depend strongly on the viscosity in such a way that when the field is turned off the order and consequently the systems keeps its high thermal conductivity for hours.
- The dynamic viscosity increases with the concentration and with the magnetic field, however, this effect is reduced by the increase of the shear stress, because the chains that are being formed are continuously destroyed.

- The model for the thermal conductivity as a function as the dynamic viscosity proposed works properly with the experimental data obtained.

Thermal transport properties of liquids using the front-face flash method

- A simple and novel methodology for performing the complete thermal characterization of fluids using flash radiometry was developed.

- The results obtained for thermal diffusivity, thermal effusivity, and thermal conductivity are consistent with the values reported in the literature, which indicates that the one-dimensional model of the three-layer system and the considerations of non-convection and thermal resistance in the solid-liquid interface are the appropriate ones.

- The simulations established the limits of applicability of the technique for the characterization of common liquids, in our case of $\epsilon_2 \lesssim 500$ Ws $^{1/2}$ m $^{-2}$ K $^{-1}$. However, it is possible that changes on the slab (thermal properties or thickness) help to avoid this restriction.

- The frontal flash front-face technique compared with the traditional method (rear-face) is much faster, which significantly decreases the fluid characterization times.

Thermal percolation in random in microparticles composites

- The thermal and electric percolation of composites made up of carbonyl iron microparticles embedded in polyester resin matrix has experimentally been observed.

- A clear thermal conductivity percolation threshold was observed at v_{pT}=0.38 and the electrical percolation threshold at v_{pE}=0.46. The shift between both thresholds is 20%, which can be explained due to the differences in the transport mechanisms involved in the electrical and thermal conduction.

- The behavior of thermal conductivity was satisfactorily modeled by Zhang's model.

- The increase on electrical conductivity tends to be sigmoidal, allowing it to be modeled by a Boltzmann curve. The electrical conductivity presents the characteristic s-shape, showing the three typical regimes: the insulator, percolative and conductive.

Perspectives

According to the results obtained in this thesis, and from the experience gained, some works have been proposed to carry out in the future:

Study of the thermal properties of smart fluids by front-face method: The experimental system used for the complete characterization of the thermal properties of fluids presents the appropriate characteristics for use in controllable fluids under the influence of an electric field. However, certain modifications to the methodology must be included, because of an internal heat generation by Joule effect appears when the electric field acts.

Study of thermal and electrical properties with fillers of ionic solids: Some ionic solids shows ionic electrical conductivity, for example, the tetraiodomercurate due to an order-disorder transition (at 50°C) improves its electrical conductivity in addition to thermochromism. Its use as a filler in a polymer should improve the thermal and/or electrical properties of the matrix as a function of the temperature. Its proper characterization can be used to manufacture temperature sensors.

Study of the thermal resistance of contact between spherical particles as a function of the contact area: By sintering a system of spherical particles the border between the grains is modified, improving the heat transfer. The flash technique can be used to perform these studies, it is even possible to explore the dependence at different temperatures.

List of publications

The following journal publications are product of this thesis:

- Forero-Sandoval, I. Y., Vega-Flick, A., Alvarado-Gil, J. J., and Medina-Esquivel, R. A. (2017). Study of thermal conductivity of magnetorheological fluids using the thermal-wave resonant cavity and its relationship with the viscosity. Smart Materials and Structures, 26(2), 025010. doi: 10.1088/1361-665X/26/2/025010

- Forero-Sandoval, I. Y., Pech-May, N. W., and Alvarado-Gil, J. J. (2018). Measurement of the thermal transport properties of liquids using the front-face flash method. Infrared Physics and Technology, 93, 9–15. doi: 10.1016/J.INFRARED.2018.07.009

- Percolation threshold shift between thermal and electric conductivities of carbonyl-iron composites. Forero-Sandoval, I. Y., Cervantez-Alvarez, F., Ramirez-Rincon, J. A., Macias, J. D., Pech-May, N. W., Ordonez-Miranda J. E., and Alvarado-Gil, J. J. (submitted).

Also, the works developed in this thesis have been presented in the following international conferences:

- Forero-Sandoval, I. Y., Cervantez-Alvarez, F., Ramirez-Rincon, J. A., Macias, J. D., Pech-May, N. W., Ordonez-Miranda J. E., and Alvarado-Gil, J. J. "Thermal and electric percolation in random microparticles composites". 20th International Conference on Photoacoustic and Photothermal Phenomena. Moscow, Russia. July 7-12, 2019.

- I.Y. Forero-Sandoval, N.W. Pech-May and J.J. Alvarado-Gil, "Simultaneous Measurement Of The Thermal Diffusivity And Thermal Effusivity Of Liquids Using The Front-Face Flash Method". 19th International Conference on Photoacoustic and Photothermal Phenomena. Bilbao. July 16-20, 2017

- Ivan Yecid Forero-Sandoval, Ruben Medina-Esquivel, Alejandro Vega-Flick and Juan José Alvarado-Gil, "Study of Heat Transport in Magnetorheological Fluids Using the Thermal-Wave Resonant Cavity and Its Relationship with the Viscosity" 19th Symposium on Thermophysical Properties, Boulder, Colorado, June 21-26, 2015.

Appendix A

Theoretical models

In this section, the mathematical models used for the determination of thermal properties of solids and liquids are presented. The first part focus on the analysis of the signals in the thermal wave resonator cavity (TWRC), which was used for the determination of the thermal diffusivity of magnetorheological fluids. The second part presents the models, based on the thermal quadrupole approach, used in the flash front-face technique, which were used to determine the thermal diffusivity and thermal effusivity of solids and liquids.

A.1 Periodic heating

A.1.1 Periodic heating in a two-layer system (TWRC)

Broadly speaking, the TWRC [95,96,168] is a three-layer system composed of: a slab of silicon which is heated by a modulated laser beam, a fluid (or a gas) to be studied whose thickness L can be controlled and a pyroelectric detector that due to changes in temperature generates an electrical signal [169]. This signal can be decomposed on amplitude and phase by a lock-in amplifier (In chapter 3 the experimental system is presented in detail). The slab of silicon is heated by a monochromatic light beam with wavelength λ, modulated sinusoidally [170] with intensity given by,

$$I(t) = \frac{I_0}{2}(1 + \cos(\omega t)), \tag{A.1}$$

with $\omega = 2\pi f$ the frequency of the light source and I_0 the intensity of the incident radiation. Since the silicon is thermally thin for the frequency of 5 Hz that was used but opaque to the incident light, we can consider it as the generator of thermal waves. From this, and taking into account the configuration of the figure A.1, we propose the diffusion equations for a two-layer system, that is, liquid sample-pyroelectric detector.

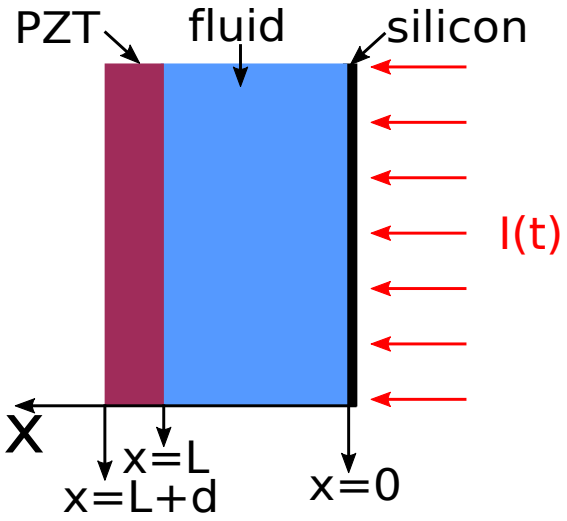

Figure A.1: Geometric representation of the layered system: silicon-sample-pyroelectric detector, employed to study the heat flux in the thermal wave resonant cavity.

$$\frac{d^2T_f}{dx^2} - \sigma_f^2 T_f = 0 \quad 0 \leq x \leq L, \tag{A.2}$$

$$\frac{d^2T_p}{dx^2} - \sigma_p^2 T_p = 0, \quad L \leq x \leq L + d, \tag{A.3}$$

with T_j the temperature, α_j the thermal diffusivity (where f is for the liquid sample and p for the pyroelectric), L the distance between the silicon and the pyroelectric detector and σ has been defined as the coefficient of thermal diffusion,

$$\sigma_j \equiv (1+i)\sqrt{\frac{\pi f}{\alpha_j}}. \tag{A.4}$$

In equations A.2 and A.3 it has been considered that both the thermal radiation and the convection are negligible, also that the pyroelectric detector is thermally thick and can be considered as semi-infinite. The solutions for these equations are

$$T_f = C_1 e^{-\sigma_f x} + C_2 e^{\sigma_f x} \quad 0 \leq x \leq L, \tag{A.5}$$

$$T_p = C_3 e^{-\sigma_p (x-L)} \quad L \leq x \leq L + d. \tag{A.6}$$

The heat transfer is unidirectional, whose direction is determined by the existence of a temperature gradient. The use of a reflected thermal wave is a mathematical tool that helps to describe the discontinuity in thermal effusivity in the pyroelectric sample-detector interface, which leads to a decrease in heat flow [95]. The coefficients, C_1, C_2, and C_3 are determined by the boundary conditions of the temperature (Equations A.7a and A.7b) and the continuity of the heat flow (Equation A.7c), that is,

$$T_f(0) = T_0, \tag{A.7a}$$

$$T_f(L) = T_p(L), \tag{A.7b}$$

$$-K_f \frac{dT_f}{dx}\bigg|_{x=L} = -K_p \frac{dT_p}{dx}\bigg|_{x=L}, \tag{A.7c}$$

with T_0 defined as the temperature amplitude of the thermal wave generator. Our interest focuses on the temperature in the pyroelectric sensor, that is, C_3

$$C_3 = \frac{2T_0 b_{fp} e^{-\sigma_f L}}{(1+b_{fp}) - (1+b_{fp}) e^{-2\sigma_f L}}, \tag{A.8}$$

where b_{fp} has been defined as

$$b_{fp} = \frac{k_f}{k_p}\frac{\sqrt{\alpha_p}}{\sqrt{\alpha_f}}. \tag{A.9}$$

The output voltage V due to harmonic heating of the pyroelectric sensor is given by [171]

$$V(\omega) = \frac{i\omega p \tau_e d T_\omega}{\epsilon_p (1 + i\omega\tau_e)} e^{i\omega t}, \tag{A.10}$$

where p is the pyroelectric constant, τ_e is the electronic time constant, ϵ_p is the permittivity and T_ω is the average temperature rise in the pyroelectric sensor [25] :

$$T_\omega =< T_p >= \frac{1}{d} \int_{x=L}^{x=L+d} T_p dx = \frac{C_3}{\sigma_p d}(1 - e^{-\sigma_p L_p}). \tag{A.11}$$

If we consider that the pyroelectric detector is thermally thick that is, $\sigma_p d \gg 1$, the pyroelectric detector voltage can be written:

$$V(\omega) = S(f)\frac{C_3}{\sigma_p}. \tag{A.12}$$

The S function depends on the frequency. The output voltage of the detector due to changes in the temperature can be written as

$$V(f) = \frac{2T_0 S(f) b_{fp} \sigma_p^{-1} e^{-\sigma_f L}}{(1 + b_{fp}) - (1 + b_{fp}) e^{-2\sigma_f L}}. \tag{A.13}$$

Equation A.13 can be simplified assuming that $b_{gp} \ll 1$ and L is large enough so that $e^{-2\sigma_g L} \ll 1$

$$V(f) \approx 2T_0 S(f) b_{fp} \sigma_p^{-1} e^{-\sigma_f L} = M(f) e^{-\sigma_f L}, \tag{A.14}$$

where $M(f)$ is a function that depends on the frequency f of the thermal wave. using A.4 we can rewrite equation A.14:

$$V(f) \approx M(f) e^{-a_f L} \Big[\cos\left(a_f L + \frac{\pi}{4}\right) - i \sin\left(a_f L + \frac{\pi}{4}\right) \Big]. \tag{A.15}$$

where a_f relates the thermal diffusivity α_f and the frequency f as follows:

$$a_f = \sqrt{\frac{\pi f}{\alpha_f}}. \tag{A.16}$$

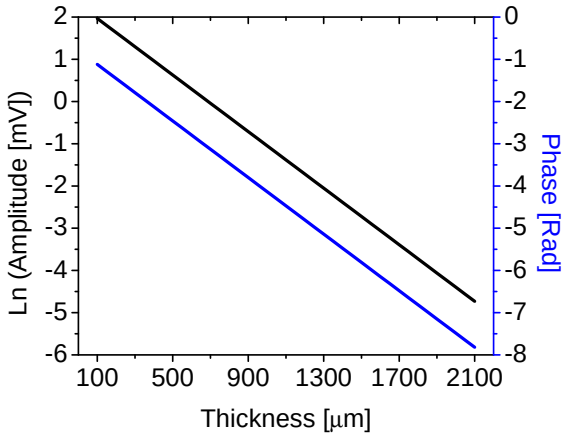

Figure A.2: Natural logarithm of the amplitude A and phase δ as a function of thickness L from the equation A.15. The black line represents $\ln(A)$ and the blue line represents δ.

From equation A.15, we can extract the amplitude $A = M(f)e^{-a_g L}$ and the phase $\delta = -a_g L + \frac{\pi}{4}$. Figure A.2 shows the natural logarithm of the amplitude A and the phase as a function of the sample thickness L, for a frequency of 5 Hz and thermal diffusivity 0.14 mm^2s^{-1}. In both cases the slope is $-a_g$, this means that if we decompose the signal of the pyroelectric detector in amplitude and phase and obtain the value of the slopes of the curves ln (A) vs L and δ vs L, we can obtain the thermal diffusivity by means of the equation A.16.

A.2 Pulsed heating

A.2.1 An introduction to thermal quadrupoles: temperature on an isolated slab

The method of thermal quadrupoles [172] in the case of heat transfer problems is based on 2x2 matrices that relate the temperature and flux on one surface of a medium with the same quantities in another surface. On the case of one-dimensional transient, the transformation refers to Laplace transforms. In order to observe how the matrices are constructed, consider the case of an opaque solid slab L, with thermal diffusivity α, thermal conductivity k, without

internal sources of energy, isolated and in thermal equilibrium at the initial time, which is heated by a light pulse Q in the front-face (z=0), as is shown in figure A.3. In the case of one-dimensional heat transfer, the heat equation and the initial conditions are given by:

$$\frac{\partial^2 T}{\partial z^2} = \frac{1}{\alpha}\frac{\partial T}{\partial t} \qquad \text{for} \qquad 0 < z < L, \tag{A.17a}$$

$$T(0) = T_0. \tag{A.17b}$$

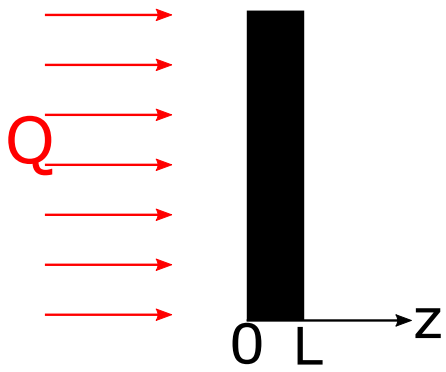

Figure A.3: Diagram representing a solid opaque slab of thickness L, isolated and heated by a short light pulse on $z = 0$.

Equation A.17a in the Laplace space can be written as follows:

$$\frac{\partial^2 \theta}{\partial z^2} = \frac{s}{\alpha}\theta, \tag{A.18}$$

where s is the Laplace parameter. The solution for he equation A.18 is as follows:

$$\theta(z, s) = K_1 \sinh(qz) + K_2 \cosh(qz), \tag{A.19}$$

with $q^2 = s/\alpha$. Let us remind that the flow of heat Φ on the axis z is associated with the temperature T by:

$$\Phi(z, t) = -kS\frac{\partial T(z, t)}{\partial z}, \tag{A.20}$$

where S is the surface area considered for heat transfer. The heat flux in the Laplace space has a solution as follows:

$$\phi(z,s) = -kS\frac{d\theta(z,s)}{dz} = -kSq(K1\cosh(qz) + K2\sinh(qz)). \tag{A.21}$$

Equations A.19 and A.21 can be written for the front-face ($z = 0$) and the rear-face ($z = L$), which allow us to obtain a system of equations that relate K_1, K_2, the Laplace transformation of temperatures and the heat fluxes, as follows,

$$\theta(0,s) = K_1, \tag{A.22a}$$

$$\phi(0,s) = -kSqK_2, \tag{A.22b}$$

$$\theta(L,s) = K1\cosh(qL) + K_2\sinh(qL), \tag{A.22c}$$

$$\phi(L,s) = -kSqK_1\sinh(qL) - kSqK_2\cosh(qL). \tag{A.22d}$$

The values of K_1 and K_2 can be obtained from the equations A.22a to A.22d, and we can write $[\theta(0,s), \phi(0,s)]$ as a function of $[\theta(L,s), \phi(L,s)]$, as follows:

$$\begin{bmatrix}\theta(0,s)\\ \phi(0,s)\end{bmatrix} = \begin{bmatrix}\cosh(qL) & \frac{1}{kSq}\sinh(qL)\\ kSq\sinh(qL) & \cosh(qL)\end{bmatrix}\begin{bmatrix}\theta(L,s)\\ \phi(L,s)\end{bmatrix}. \tag{A.23}$$

This matrix is equivalent to the heat equation and completely describe the proposed system, which can be written in a general way as follows,

$$\begin{bmatrix}\theta(0,s)\\ \phi(0,s)\end{bmatrix} = \begin{bmatrix}A & B\\ C & D\end{bmatrix}\begin{bmatrix}\theta(z,s)\\ \phi(z,s)\end{bmatrix}, \tag{A.24}$$

where A, B, C and D are called quadrupole coefficients and are given by

$$A = D = \cosh(qz), \tag{A.25a}$$

$$B = \frac{1}{kSq}\sinh(qz), \tag{A.25b}$$

$$C = kSq\sinh(qz). \tag{A.25c}$$

In order to calculate the temperatures in $T(z=0,t)$ and $T(z=L,t)$, we will use a Dirac light pulse of total energy Q [Jm^{-2}] on the face $z=0$ (Front-face) while the face $z=L$ (Rear-face) remains isolated:

$$\Phi(0,t) = QS\delta(t) \tag{A.26a}$$

$$\Phi(L,t) = 0 \tag{A.26b}$$

The heat flux expressions can be rewritten on the Laplace space as follows

$$\phi(0,s) = QS, \tag{A.27a}$$

$$\phi(L,s) = 0, \tag{A.27b}$$

Finally, using the conditions A.27a and A.27b on the equation A.23, the Laplace transform of the temperatures on each face is:

Front-Face:

$$\theta(0) = \frac{QS}{C} = \frac{Q}{k\sqrt{s/\alpha}\sinh(L\sqrt{s/\alpha})}, \tag{A.28}$$

Rear-Face:

$$\theta(L) = \frac{QSA}{C} = \frac{Q}{k\sqrt{s/\alpha}\tanh(L\sqrt{s/\alpha})}. \tag{A.29}$$

In most cases, it is not possible to find an analytical solution for the temperature. For this reason, numerical methods are used to find the temperature as a function of time. There are several algorithms like the Gaver-Stehfest and Euler one [126]. In this thesis the Euler algorithm was used.

A.2.2 The Euler algorithm

The Euler algorithm is an implementation of the Fourier-series method, using Euler summation to accelerate convergence of the final infinite series. If $F(s)$ is the Laplace transform of $f(t)$, namely $F(s) = L[f(t)]$, the inversion formula to numerically calculate $f(t)$ is given by,

$$f(t,M) = \frac{10^{M/3}}{t}\sum_{k=0}^{2M}\eta_k \Re\Big(F\Big(\frac{\beta_k}{t}\Big)\Big), \tag{A.30}$$

where

$$\beta_k = \frac{M\ln(10)}{3} + \pi i k, \quad \eta_k \equiv (-1)^k \xi_k \tag{A.31}$$

With $i = \sqrt{-1}$, and

$$\xi_0 = \frac{1}{2}, \quad \xi_k = 1, \quad 1 \leq k \leq M, \quad \xi_{2M} = \frac{1}{2^M} \tag{A.32a}$$

$$\xi_{2M-k} = \xi_{2M-k+1} + 2^{-M}\binom{M}{K}, \quad 0 < k < M, \tag{A.32b}$$

The algorithm of Euler (equation A.30), is used to invert the equations A.28 and A.29, with $M = 16$. Figure A.4 shows the temperatures on the front-face (red line) and rear-face (black line) as a function of time. These curves represent a 1.5 mm thick slab, with thermal diffusivity 0.1 mm^2/s and thermal conductivity of 0.2 $Wm^{-1}K^{-1}$ under a Dirac heating 1 kJm^{-2}.

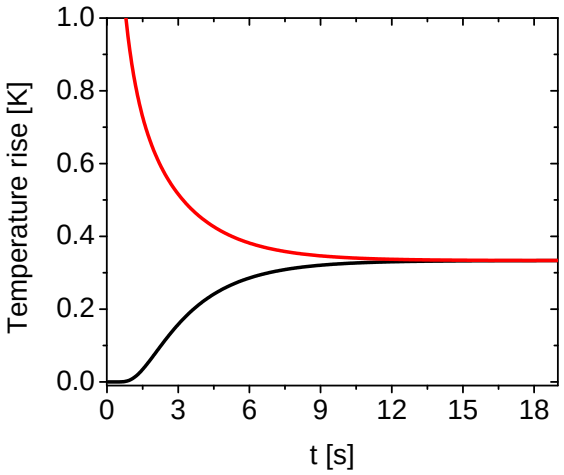

Figure A.4: Temperature as a function of time for an isolated slab heated by a Dirac heat pulse. The red line represents the temperature for the front-face ($z = 0$) and the black line represents the temperature for the rear-face ($z = L$).

A.2.3 Heat losses

Heat losses by convection and radiation are included in this method in a simple way if now considered in the boundary conditions these losses, the heat flux has to be written:

$$\Phi(0) = hS(T(0) - T_\infty) - \Phi_0(0). \tag{A.33}$$

This equation corresponds to the surface heat balance. The net flux $\Phi(0)$ on the surface at temperature $T(0)$ is the difference between the heat losses and the power of the heat source with the sample is excited. Taking $T_\infty = 0$, in the Laplace space the equation A.33, can be written as

$$\phi(0) = hS\theta(0) - \phi_0(0), \tag{A.34}$$

which can be written in matrix form,

$$\begin{bmatrix} \theta(0) \\ \phi(0) \end{bmatrix} = \begin{bmatrix} 1 & 0 \\ hS & 1 \end{bmatrix} \begin{bmatrix} \theta(0) \\ -\phi_0(0) \end{bmatrix}. \tag{A.35}$$

The mathematical models that were used for the determination of the thermal properties of liquids and solids studied in this thesis will be presented. Since the evolution of the temperature was studied in the face that was heated, only the models for the front-face configuration would be presented. The three systems used in this thesis for thermal characterization of materials are presented below:

- Heat pulse on a slab with convection heat losses. Used in chapter 5.
- Heat pulse on a two-layer system: slab with a semi-infinite liquid backing. Used in chapter 5.
- Heat pulse on a three-layer system with convection heat losses, used in chapter 4.

A.2.4 Heat pulse on a slab with convection heat losses

Consider an opaque slab of thickness L, illuminated by a uniform heating pulse Q for a short time (∼20 ms), with thermal diffusivity α and thermal effusivity e as shown in figure A.5. The Laplace temperatures and the heat fluxes are given by:

$$\begin{bmatrix} \theta(0,s) \\ \phi(0,s) \end{bmatrix} = \begin{bmatrix} 1 & 0 \\ hS & 1 \end{bmatrix} \begin{bmatrix} A & B \\ C & D \end{bmatrix} \begin{bmatrix} 1 & 0 \\ hS & 1 \end{bmatrix} \begin{bmatrix} \theta(L,s) \\ \phi(L,s) \end{bmatrix}. \tag{A.36}$$

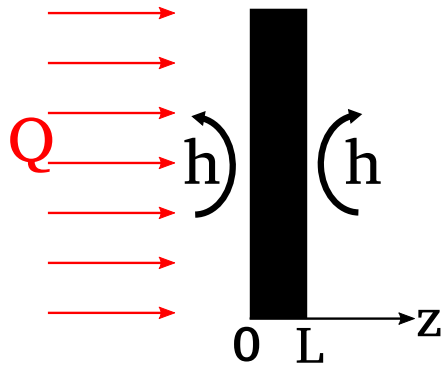

Figure A.5: Diagram representing a solid opaque slab of thickness L heated by a short light pulse on $z = 0$.

The heat transfer by convection from the solid surfaces in contact with the air is represented by the heat transfer coefficients h. Considering that the excitation occurs only on the front-face $\phi(0,s) = \bar{I}_0 \chi S$ and $\phi(L,s) = 0$, the Laplace temperature on the front-face is given by

$$\theta(0,s) = \frac{\bar{I}_0 S\,(A + BhS)}{C + (A+D)hS + Bh^2S^2}. \tag{A.37}$$

Substituting the values A, B, C and D given by the equation A.25 and the relationship between thermal conductivity, thermal effusivity and thermal diffusivity $k = \epsilon\sqrt{\alpha}$, we obtain

$$\theta(0,s) = \frac{\bar{I}_0 \chi}{e} \frac{\sqrt{s} + h_p \tanh(x\sqrt{s})}{2h_p\sqrt{s} + (s + h_p^2)\tanh(x\sqrt{s})}. \tag{A.38}$$

Where χ is the energy fraction absorbed by the front surface, s is the Laplace parameter, $x = L/\sqrt{\alpha}$ and $h_p = h/\epsilon_s$ and h is the heat transfer coefficient by convection from the solid surfaces in contact with air. $\bar{I}_0$ represents the Laplace transform of the light pulse. Its Laplace transform is $\bar{I}_0 = Q$, being Q the energy per unit area (Jm^{-2}) delivered by the pulse. Figure A.6 shows the temperature evolution for a sample with thermal diffusivity of 0.1 mm2/s, thermal effusivity 800 $Wm^{-2}s^{1/2}K^{-1}$, thickness of a 1 mm, a Dirac heating of 1 KJm^{-2} and a typical convection coefficient of 10 $Wm^{-2}K^{-1}$.

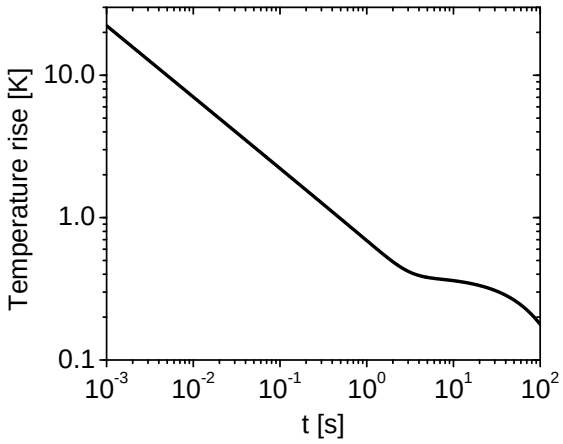

Figure A.6: Typical curve for temperature as a function of time for an slab heated by a Dirac heat pulse (equation A.38).

A.2.5 Heat pulse on a two-layer system: slab with a semi-infinite liquid backing

A wall of sufficiently large thickness so that a heat pulse applied to one face is not felt by the other face is known as a semi-infinite medium. Such a system represents the evolution of a wall of finite thickness for a sufficiently short time so that the disturbance created on one face has not reached the other side (true for the point in time that the temperature of the other face does not vary). For a semi-infinite medium, the solution of the equation A.18 takes the form,

$$\theta(z,s) = C\exp(-qz). \tag{A.39}$$

From the equation A.21, the value of the Laplace transform of the heat flux rate at a point of the semi-infinite medium as:

$$\phi(z,s) = kSqC\exp(-qz) = kSq\theta(z,s), \tag{A.40}$$

Which can be also written in terms of the thermal effusivity using the relationship $k = e\sqrt{\alpha}$,

$$\phi(z,s) = kSqC\exp(-qz) = eS\sqrt{s}\theta(z,s), \tag{A.41}$$

that is to say, $\theta(z,s) = \phi(z,s)/eS\sqrt{s}$, and the expressions for both can be written as a matrix form, as follows,

$$\begin{bmatrix}\theta(z,s)\\ \phi(z,s)\end{bmatrix} = \begin{bmatrix}1 & \frac{1}{eS\sqrt{s}}\\ 0 & 1\end{bmatrix}\begin{bmatrix}0\\ \phi(z,s)\end{bmatrix} = \begin{bmatrix}\theta(z,s)\\ eS\sqrt{s}\theta(z,s)\end{bmatrix}. \tag{A.42}$$

Consider the system shown in the figure A.7, which consists of an opaque solid of thickness L with a semi-infinite liquid backing. The solid face is heated by an uniform pulse Q for a short time. To find an increase in temperature on the front face, the corresponding Laplace transform of the temperature rise at that surface ($z = 0$) is calculated as follows:

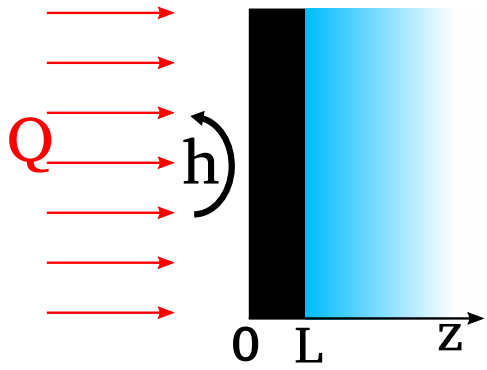

Figure A.7: Diagram representing an opaque solid of thickness L with a semi-infinite liquid backing.

$$\begin{bmatrix} \theta(0,s) \\ \phi(0,s) \end{bmatrix} = \begin{bmatrix} 1 & 0 \\ hS & 1 \end{bmatrix} \begin{bmatrix} A & B \\ C & D \end{bmatrix} \begin{bmatrix} \theta(z,s) \\ eS\sqrt{s}\theta(z,s) \end{bmatrix}. \tag{A.43}$$

The heat transfer by convection from the solid surfaces in contact with the air is represented by the heat transfer coefficients h. Considering that the excitation only occurs on the front-face $\phi(0,s) = \bar{I}_0\chi S$, the Laplace temperature on the front-face is given by,

$$\theta(0) = \frac{\bar{I}_0\chi}{e_s\sqrt{s}} \frac{\cosh(x\sqrt{s}) + b_{21}\sinh(x\sqrt{s})}{\left(b_{21} + \frac{h_p}{\sqrt{s}}\right)\cosh(x\sqrt{s}) + \left(1 + \frac{h_p b_{21}}{\sqrt{s}}\right)\sinh(x\sqrt{s})}, \tag{A.44}$$

where χ is the energy fraction absorbed by the front surface, s is the Laplace parameter, $x = L/\sqrt{\alpha}$, $h_p = h/e_s$, $b_{21} = e_f/e_s$, and h is the heat transfer coefficient by convection from the solid surfaces in contact with air. $\bar{I}_0$ represents the Laplace transform of the light pulse. Its Laplace transform is $\bar{I}_0 = Q$, being Q the energy per unit area ($\mathrm{Jm^{-2}}$) delivered by the pulse. Figure A.8 shows the temperature evolution for a solid sample with thermal diffusivity of 0.1 $\mathrm{mm^2/s}$, thermal effusivity of 600 $\mathrm{Wm^{-2}s^{1/2}K^{-1}}$ and 1 mm thickness with a liquid layer of thermal effusivity 1500 $\mathrm{Wm^{-2}s^{1/2}K^{-1}}$. The front-face is heated by a Dirac ligth pulse of 1 $\mathrm{KJm^{-2}}$ and we take in account a typical convection coefficient of 10 $\mathrm{Wm^{-2}K^{-1}}$.

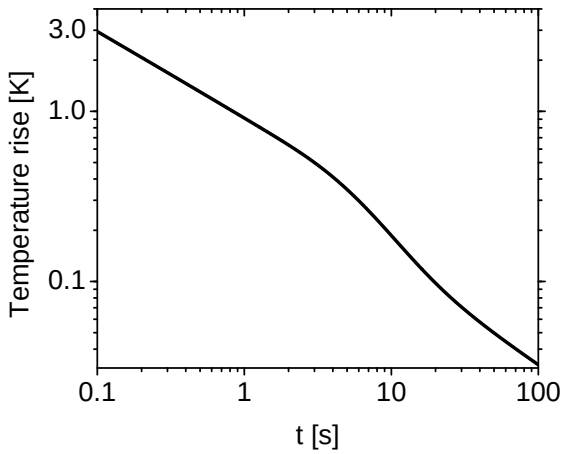

Figure A.8: Typical curve for temperature as a function of time for an opaque solid of thickness L with a semi-infinite liquid backing.

A.2.6 Heat pulse on a three-layer system with a convection heat losses

The two-layer system studied in the previous section allows us to obtain a complete thermal characterization of solids and in the case of liquids only thermal effusivity. By means of a three-layer system, it is possible to obtain a complete characterization of liquids as shown in this secction. Consider the three-layer system shown in the figure A.9, which consists of a layer of water of thickness L_2 between two solid plates of thickness L_1. One metallic surface $z = 0$ is illuminated uniformly by a uniform pulse and the corresponding Laplace transform of the temperature rise at that surface ($z = 0$) is calculated by:

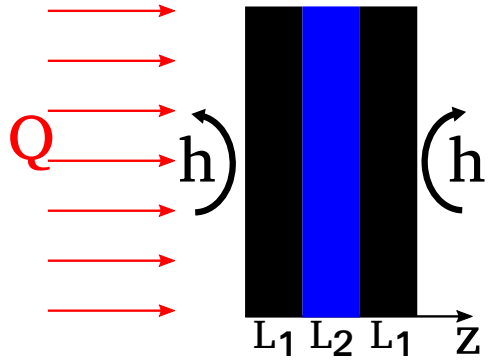

Figure A.9: Diagram representing an three-layer system.

$$\begin{bmatrix} \theta(0,s) \\ \phi(0,s) \end{bmatrix} = \begin{pmatrix} 1 & 0 \\ hS & 1 \end{pmatrix} \begin{pmatrix} A_{3L} & B_{3L} \\ C_{3L} & D_{3L} \end{pmatrix} \begin{pmatrix} 1 & 0 \\ hS & 1 \end{pmatrix} \begin{bmatrix} \theta(L,s) \\ \phi(L,s) \end{bmatrix}. \tag{A.45}$$

The heat transfer by convection from the solid surfaces, in contact with the surrounding atmosphere (air), is taken into account by the quadrupole matrices involving the heat transfer coefficient h. Here L is the total length of the three-layer system, i.e., $z = L$ is the rear-face of the system. Note that heat transfer by convection at the solid-liquid interfaces have been neglected since the temperature rise at both interfaces is small. The quadrupole matrix with coefficients A_{3L}, B_{3L}, C_{3L} and D_{3L} is obtained from the product of the transfer matrices corresponding to the three layers in the system:

$$\begin{pmatrix} A_{3L} & B_{3L} \\ C_{3L} & D_{3L} \end{pmatrix} = \begin{pmatrix} A_1 & B_1 \\ C_1 & A_1 \end{pmatrix} \begin{pmatrix} A_2 & B_2 \\ C_2 & A_2 \end{pmatrix} \begin{pmatrix} A_1 & B_1 \\ C_1 & A_1 \end{pmatrix}, \tag{A.46}$$

where the quadrupole coefficients of the i-th layer are given by:

$$A_i = \cosh\left(x_i\sqrt{s}\right), \tag{A.47a}$$

$$B_i = \frac{1}{\epsilon_i S\sqrt{s}} \sinh\left(x_i\sqrt{s}\right), \tag{A.47b}$$

$$C_i = \epsilon_i S\sqrt{s} \sinh\left(x_i\sqrt{s}\right). \tag{A.47c}$$

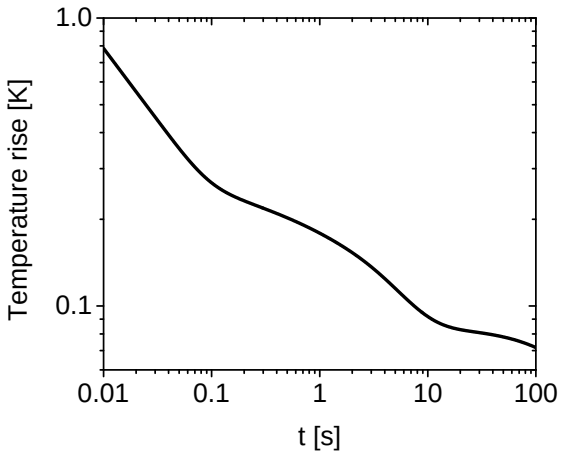

Figure A.10: Typical curve for temperature as a function of time for a three-layer system. The three layer system is composed by a two stainless steel slabs and the liquid layer is water.

Considering that excitation occurs only on the front-face $\phi(0, s) = \bar{I}_0\chi S$, the Laplace temperature on the front-face is given by,

$$\theta(0) = \frac{\bar{I}_0\chi S\left(A_{3L} + B_{3L}hS\right)}{C_{3L} + (A_{3L} + D_{3L})hS + B_{3L}h^2S^2}, \tag{A.48}$$

where χ is the energy fraction absorbed by the front surface, s is the Laplace parameter, h is the heat transfer coefficient by convection from the solid surfaces in contact with air. $\bar{I}_0$ represents the Laplace transform of the light pulse. Its Laplace transform is $\bar{I}_0 = Q$, being

Q the energy per unit area (Jm^{-2}) delivered by the pulse. The quadrupole coefficients given in Eqs. A.47 can be written in terms of the following five parameters: $Q\chi/\epsilon_1$, $x_1 = L_1/\sqrt{\alpha_1}$, $x_2 = L_2/\sqrt{\alpha_2}$, $b_{21} = \epsilon_2/\epsilon_1$ (the ratio between the thermal effusivity of the liquid to that of the solid), and h/ϵ_1.

Figure A.10 shows the temperature evolution of a metallic slab at $z = 0$. The metallic slab is a stainless steel plate of 1 mm thickness, with thermal diffusivity of 3.6 mm^2/s and thermal effusivity of 7188 $Wm^{-2}s^{1/2}K^{-1}$. The liquid layer is water of 1 mm of thickness, with thermal diffusivity of 0.14 mm^2/s and thermal effusivity 1576 $Wm^{-2}s^{1/2}K^{-1}$. The front-face is heated by Dirac ligth pulse of 1 KJm^{-2} and we take in account a typical convection coefficient of 10 $Wm^{-2}K^{-1}$.

References

[1] S. Mazumdar, *Composites Manufacturing*. CRC Press, dec 2001.

[2] F. C. Campbell, *Structural Composite Materials*. ASM International, 2010.

[3] M. A. Vadivelu, R. Kumar, G. M. Joshi, and C. R. Kumar, "Polymer composites for thermal management: a review," *Compos. Interface.*, vol. 23, no. 9, pp. 847–872, 2016.

[4] H. Chen, V. V. Ginzburg, J. Yang, Y. Yang, W. Liu, Y. Huang, L. Du, and B. Chen, "Thermal conductivity of polymer-based composites: Fundamentals and applications," *Prog. Polym. Sci.*, vol. 59, pp. 41–85, aug 2016.

[5] H. S. Kim, J. U. Jang, H. Lee, S. Y. Kim, S. H. Kim, J. Kim, Y. C. Jung, and B. J. Yang, "Thermal Management in Polymer Composites: A Review of Physical and Structural Parameters," *Adv. Eng. Mater.*, vol. 20, no. 10, p. 1800204, 2018.

[6] I. Bica, "Advances in Magnetorheological Suspension: Production and Properties," *J. Ind. Eng. Chem.*, vol. 12, no. 4, pp. 501–515, 2006.

[7] R. Stanway, "Smart fluids: current and future developments," *Mater. Sci. Technol.*, vol. 20, pp. 931–939, aug 2004.

[8] J. Rabinow, "The Magnetic Fluid Clutch," *Trans. Am. Inst. Electr. Eng.*, vol. 67, no. 2, pp. 1308–1315, 1948.

[9] G.-W. Lee, M. Park, J. Kim, J. I. Lee, and H. G. Yoon, "Enhanced thermal conductivity of polymer composites filled with hybrid filler," *Compos. Part. A-Appl. S.*, vol. 37, no. 5, pp. 727 – 734, 2006.

[10] J. Wang and G. Meng, "Magnetorheological fluid devices: principles, characteristics and applications in mechanical engineering," *Proceedings of the Institution of Mechanical Engineers, Part L: Journal of Materials: Design and Applications*, vol. 215, no. 3, pp. 165–174, 2001.

[11] V. Jain, "Magnetic field assisted abrasive based micro-/nano-finishing," *J. Mater. Process. Technol.*, vol. 209, no. 20, pp. 6022–6038, 2009.

[12] M. C. Heine, J. de Vicente, and D. J. Klingenberg, "Thermal transport in sheared electro- and magnetorheological fluids," *Phys. Fluids*, vol. 18, p. 023301, feb 2006.

[13] B. N. Reinecke, J. W. Shan, K. K. Suabedissen, and A. S. Cherkasova, "On the anisotropic thermal conductivity of magnetorheological suspensions," *J. Appl. Phys.*, vol. 104, p. 023507, jul 2008.

[14] G. Yildirim and S. Genc, "Experimental study on heat transfer of the magnetorheological fluids," *Smart Mater. Struct.*, vol. 22, p. 085001, aug 2013.

[15] Q. Li, Y. Xuan, and J. Wang, "Experimental investigations on transport properties of magnetic fluids," *Exp. Therm. Fluid Sci.*, vol. 30, pp. 109–116, nov 2005.

[16] C. Zweben, "Advances in composite materials for thermal management in electronic packaging," *JOM*, vol. 50, pp. 47–51, jun 1998.

[17] J. Kim, B.-S. Yim, J.-M. Kim, and J. Kim, "The effects of functionalized graphene nanosheets on the thermal and mechanical properties of epoxy composites for anisotropic conductive adhesives (ACAs)," *Microelectron. Reliab.*, vol. 52, pp. 595–602, 2012.

[18] C. Li, T. Liang, W. Lu, C. Tang, X. Hu, M. Cao, and J. Liang, "Improving the antistatic ability of polypropylene fibers by inner antistatic agent filled with carbon nanotubes," *Compos. Sci. Technol.*, vol. 64, no. 13-14, pp. 2089–2096, 2004.

[19] X. Zhang, Y. Ma, C. Zhao, and W. Yang, "High dielectric constant and low dielectric loss hybrid nanocomposites fabricated with ferroelectric polymer matrix and BaTiO 3 nanofibers modified with perfluoroalkylsilane," *Appl. Surf. Sci.*, vol. 305, pp. 531–538, jun 2014.

[20] Y. Wang, Y. Hou, and Y. Deng, "Effects of interfaces between adjacent layers on breakdown strength and energy density in sandwich-structured polymer composites," *Compos. Sci. Technol.*, vol. 145, pp. 71–77, 2017.

[21] H. Huang, C. Liu, Y. Wu, and S. Fan, "Aligned carbon nanotube composite films for thermal management," *Adv. Mater.*, vol. 17, no. 13, pp. 1652–1656, 2005.

[22] R. Prasher, "Thermal interface materials: Historical perspective, status, and future directions," *Proceedings of the IEEE*, vol. 94, pp. 1571–1586, Aug 2006.

[23] D. W. Hahn and M. N. Özişik, *Heat Conduction*. Hoboken, NJ, USA: John Wiley & Sons, 2012.

[24] T. L. Bergman, F. P. Incropera, D. P. DeWitt, and A. S. Lavine, *Fundamentals of heat and mass transfer*. John Wiley & Sons, 2011.

[25] D. Almond and P. Patel, *Photothermal Science and Techniques*. Chapman & Hall, 1996.

[26] A. Bejan, *Convection Heat Transfer*. John Wiley & Sons, 2013.

[27] J. H. Lienhard IV and J. H. Lienhard V, *A Heat Transfer Textbook, fourth edition*. Courier Corporation, 2012.

[28] J. Holman, *Heat transfer*. McGraw-Hill, 2002.

[29] H. S. Carslaw and J. C. Jaeger, *Conduction of Heat in Solids*. Oxford: Clarendon Press, 2nd ed., 1986.

[30] M. Vollmer and K.-P. Möllmann, *Infrared Thermal Imaging*. Weinheim, Germany: Wiley-VCH Verlag GmbH & Co. KGaA, 2010.

[31] C. Ibarra-Castanedo, J. R. Tarpani, and X. P. V. Maldague, "Nondestructive testing with thermography," *Eur. J. Phys.*, vol. 34, no. 6, pp. S91–S109, 2013.

[32] G. Gaussorgues, *Infrared Thermography*, vol. 43. Dordrecht: Springer Netherlands, 1994.

[33] W. Minkina and S. Dudzik, *Infrared Thermography, Errors and Uncertanties*. John Wiley & Sons, 2009.

[34] C. Meola and G. M. Carlomagno, "Recent advances in the use of infrared thermography," *Meas. Sci. Technol.*, vol. 15, pp. R27–R58, sep 2004.

[35] W. Sabuga and R. Todtenhaupt, "Effect of roughness on the emissivity of the precious metals silver, gold, palladium, platinum, rhodium, and iridium," *High Temp. - High Press.*, vol. 33, no. 3, pp. 261–269, 2001.

[36] G. C. Holst, *Common sense approach to thermal imaging*. SPIE Optical Engineering Press Washington, 2000.

[37] J. Psarouthakis, "Apparent Thermal Emissivity From Surfaces With Multiple V-Shaped Grooves," *AIAA J.*, vol. 1, pp. 1879–1882, aug 1963.

[38] Z. Zhimin, "A method for calculating the effective emissivity of a groove structure," in *Optical Systems for Space Applications* (H. Lutz and G. Otrio, eds.), SPIE, sep 1987.

[39] J. Cuenca and J. A. Sobrino, "Experimental measurements for studying angular and spectral variation of thermal infrared emissivity," *Appl. Opt.*, vol. 43, p. 4598, aug 2004.

[40] F. E. Nicodemus, "Directional Reflectance and Emissivity of an Opaque Surface," *Appl. Opt.*, vol. 4, no. 7, pp. 767–773, 1965.

[41] J. Labed and M. P. Stoll, "Spatial variability of land surface emissivity in the thermal infrared band: Spectral signature and effective surface temperature," *Remote Sens. Environ.*, vol. 38, no. 1, pp. 1–17, 1991.

[42] D. P. DeWitt and G. D. Nutter, *Theory and Practice of Radiation Thermometry*. Hoboken, NJ, USA: John Wiley & Sons, Inc., dec 1988.

[43] W. Herschel, "Experiments on the Solar, and on the Terrestrial Rays that Occasion Heat; With a Comparative View of the Laws to Which Light and Heat, or Rather the Rays Which Occasion Them, are Subject, in Order to Determine Whether They are the Same, or Different. Part," *Philos. Trans. R. Soc. London*, vol. 90, pp. 293–326, 1800.

[44] W. Herschel, "Investigation of the Powers of the Prismatic Colours to Heat and Illuminate Objects; with Remarks, That Prove the Different Refrangibility of Radiant Heat. To Which Is Added, an Inquiry into the Method of Viewing the Sun Advantageously, with Telescopes of," in *Proc. R. Soc. London*, vol. 1, 1800.

[45] T. J. Seebeck, "Ueber die magnetische Polarisation der Metalle und Erze durch Temperatur Differenz," *Ann. Phys.*, 1826.

[46] A. Rogalski, "History of infrared detectors," *Opto-Electronics Review*, vol. 20, no. 3, pp. 279–308, 2012.

[47] A. Rogalski, "Infrared detectors: an overview," *Infrared Phys. Technol.*, vol. 43, pp. 187–210, jun 2002.

[48] W. S. Boyle and G. E. Smith, "Charge Coupled Semiconductor Devices," *Bell Syst. Tech. J.*, 1970.

[49] P. G. Datskos and N. V. Lavrik, "Detectors—figures of merit," *Encyclopedia of Optical Engineering*, vol. 349, 2003.

[50] Hamamatsu, *Characteristic and use of infrared detectors*, March 2001.

[51] X. Maldague, *Nondestructive evaluation of materials by infrared thermography*, vol. 6. NDT and E International, 1996.

[52] X. P. Maldague, *Nondestructive evaluation of materials by infrared thermography*. Springer Science & Business Media, 2012.

[53] O. Breitenstein, W. Warta, and M. Langenkamp, *Lock-in Thermography*, vol. 10 of *Springer Series in Advanced Microelectronics*. Berlin, Heidelberg: Springer Berlin Heidelberg, 2010.

[54] FLIR, *7 Things to Know When Selecting an IR Camera for Research and Development*.

[55] X. Maldague and P. Moore, *Nondestructive Handbook, Infrared and Thermal Testing, vol. 3*. ASNT Press, Columbus, Ohio, USA,, 2001.

[56] N. Montinaro, D. Cerniglia, and G. Pitarresi, "Flying laser spot thermography technique for the NDE of fibre metal laminates disbonds," *Composite Structures*, vol. 171, pp. 63–76, 2017.

[57] A. Bedoya, J. González, A. Mendioroz, C. Pradere, A. Sommier, J. Batsale, and A. Salazar, "Flying-spot thermography: measuring the in-plane (an) isotropic thermal diffusivity of large and complex parts," in *Thermosense: Thermal Infrared Applications XLI*, vol. 11004, p. 110040J, International Society for Optics and Photonics, 2019.

[58] L. Bai, B. Gao, S. Tian, Y. Cheng, Y. Chen, G. Y. Tian, and W. L. Woo, "A comparative study of principal component analysis and independent component analysis in eddy current pulsed thermography data processing," *Rev. Sci. Instrum.*, vol. 84, p. 104901, oct 2013.

[59] G. Y. Tian, Y. Gao, K. Li, Y. Wang, B. Gao, and Y. He, "Eddy Current Pulsed Thermography with Different Excitation Configurations for Metallic Material and Defect Characterization.," *Sensors (Basel).*, vol. 16, no. 6, 2016.

[60] G. Carlomagno and P. G. Berardi, "Unsteady thermotopography in non-destructive testing," in *Proc. 3rd Biannual Exchange, St. Louis/USA*, vol. 24, p. 26, 1976.

[61] J. L. Beaudoin, E. Merienne, R. Danjoux, and M. Egee, "Numerical system for infrared scanners and application to the subsurface control of materials by photothermal radiometry," in *Infrared technology and applications*, vol. 590, pp. 285–293, International Society for Optics and Photonics, 1986.

[62] W. J. Parker, R. J. Jenkins, C. P. Butler, and G. L. Abbott, "Flash method of determining thermal diffusivity, heat capacity, and thermal conductivity," *J. Appl. Phys.*, vol. 32, no. 9, pp. 1679–1684, 1961.

[63] J. Cape and G. Lehman, "Temperature and finite pulse-time effects in the flash method for measuring thermal diffusivity," *Journal of applied physics*, vol. 34, no. 7, pp. 1909–1913, 1963.

[64] D. Sharath, M. Menaka, and B. Venkatraman, "Effect of defect size on defect depth quantification in pulsed thermography," *Measurement Science and Technology*, vol. 24, no. 12, p. 125205, 2013.

[65] D. L. Balageas, J. C. Krapez, and P. Cielo, "Pulsed photothermal modeling of layered materials," *J. Appl. Phys.*, vol. 59, no. 2, pp. 348–357, 1986.

[66] L. Clark III and R. Taylor, "Radiation loss in the flash method for thermal diffusivity," *Journal of Applied Physics*, vol. 46, no. 2, pp. 714–719, 1975.

[67] L. Fabbri and E. Scafè, "Nonuniform heating effects on thermal diffusivity measurements by the laser-pulse method: Influence of detector position," *Review of scientific instruments*, vol. 63, no. 3, pp. 2008–2013, 1992.

[68] J. McKay and J. Schriempf, "Corrections for nonuniform surface-heating errors in flash-method thermal-diffusivity measurements," *Journal of Applied Physics*, vol. 47, no. 4, pp. 1668–1671, 1976.

[69] A. Salazar, A. Mendioroz, E. Apiñaniz, C. Pradere, F. Noël, and J.-C. Batsale, "Extending the flash method to measure the thermal diffusivity of semitransparent solids," *Measurement Science and Technology*, vol. 25, no. 3, p. 035604, 2014.

[70] T. Baba and A. Ono, "Improvement of the laser flash method to reduce uncertainty in thermal diffusivity measurements," *Meas. Sci. Technol.*, vol. 12, no. 12, pp. 2046–2057, 2001.

[71] N. W. Pech-May, A. Mendioroz, and A. Salazar, "Simultaneous measurement of the in-plane and in-depth thermal diffusivity of solids using pulsed infrared thermography with focused illumination," *NDT & E International*, vol. 77, pp. 28–34, 2016.

[72] I. Y. Forero-Sandoval, N. W. Pech-May, and J. J. Alvarado-Gil, "Measurement of the thermal transport properties of liquids using the front-face flash method," *Infrared Phys. Techn.*, vol. 93, pp. 9–15, sep 2018.

[73] D. Zhao, X. Qian, X. Gu, S. A. Jajja, and R. Yang, "Measurement techniques for thermal conductivity and interfacial thermal conductance of bulk and thin film materials," *Journal of Electronic Packaging*, vol. 138, no. 4, p. 040802, 2016.

[74] N. W. Pech-May, C. Vales-Pinzón, A. Vega-Flick, Á. Cifuentes, A. Oleaga, A. Salazar, and J. J. Alvarado-Gil, "Study of the thermal properties of polyester composites loaded with oriented carbon nanofibers using the front-face flash method," *Polym. Test.*, vol. 50, pp. 255–261, 2016.

[75] A. Cezairliyan, T. Baba, and R. Taylor, "A high-temperature laser-pulse thermal diffusivity apparatus," *International journal of thermophysics*, vol. 15, no. 2, pp. 317–341, 1994.

[76] G. Carlomagno and P. G. Berardi, "Unsteady thermotopography in non-destructive testing," in *Proc. 3rd Biannual Exchange, St. Louis/USA*, vol. 24, p. 26, 1976.

[77] J. L. Beaudoin, E. Merienne, R. Danjoux, and M. Egee, "Numerical system for infrared scanners and application to the subsurface control of materials by photothermal radiometry," in *Infrared technology and applications*, vol. 590, pp. 285–293, International Society for Optics and Photonics, 1986.

[78] P. Kuo, Z. Feng, T. Ahmed, L. Favro, R. Thomas, and J. Hartikainen, "Parallel thermal wave imaging using a vector lock-in video technique," in *Photoacoustic and Photothermal Phenomena*, pp. 415–418, Springer, 1988.

[79] G. Busse, D. Wu, and W. Karpen, "Thermal wave imaging with phase sensitive modulated thermography," *Journal of Applied Physics*, vol. 71, no. 8, pp. 3962–3965, 1992.

[80] J. S. Oh and S. B. Choi, "State of the art of medical devices featuring smart electrorheological and magneto-rheological fluids," *J. King Saud Univ. - Sci.*, vol. 29, pp. 390–400, oct 2017.

[81] Q. Lu, W. Han, and H. Choi, "Smart and Functional Conducting Polymers: Application to Electrorheological Fluids," *Molecules*, vol. 23, p. 2854, nov 2018.

[82] M. R. Jolly, J. W. Bender, and J. D. Carlson, "Properties and applications of commercial magnetorheological fluids," *Journal of Intelligent Material Systems and Structures*, vol. 10, no. 1, pp. 5–13, 1999.

[83] W. M. Winslow, "Induced fibration of suspensions," *J. Appl. Phys.*, vol. 20, pp. 1137–1140, dec 1949.

[84] T. Kruse, H.-G. Krauthäuser, A. Spanoudaki, and R. Pelster, "Agglomeration and chain formation in ferrofluids: Two-dimensional x-ray scattering," *Phys. Rev. B*, vol. 67, p. 094206, Mar 2003.

[85] Z. Shulman, V. Kordonsky, and S. Demchuk, "The mechanism of heat transfer in magnetorheological systems," *Int. J. Heat Mass Transf.*, vol. 22, pp. 389–394, mar 1979.

[86] Y. Ding, H. Chen, Z. Musina, Y. Jin, T. Zhang, S. Witharana, and W. Yang, "Relationship between the thermal conductivity and shear viscosity of nanofluids," *Phys. Scr.*, vol. T139, p. 014078, may 2010.

[87] Y. Yang, E. A. Grulke, Z. G. Zhang, and G. Wu, "Thermal and rheological properties of carbon nanotube-in-oil dispersions," *J. Appl. Phys.*, vol. 99, p. 114307, jun 2006.

[88] L. Colla, L. Fedele, M. Scattolini, and S. Bobbo, "Water-based Fe_2O_3 nanofluid characterization: thermal conductivity and viscosity measurements and correlation," *Advances in Mechanical Engineering*, vol. 4, p. 674947, 2012.

[89] M. A. Zambrano-Arjona, R. Medina-Esquivel, and J. J. Alvarado-Gil, "Photothermal radiometry monitoring of light curing in resins," *J. Phys. D. Appl. Phys.*, vol. 40, pp. 6098–6104, oct 2007.

[90] P. Martínez-Torres, A. Mandelis, and J. J. Alvarado-Gil, "Photothermal determination of thermal diffusivity and polymerization depth profiles of polymerized dental resins," *J. Appl. Phys.*, vol. 106, p. 114906, dec 2009.

[91] M. R. Jolly, J. D. Carlson, and B. C. Muñoz, "A model of the behaviour of magnetorheological materials," *Smart Mater. Struct.*, vol. 5, pp. 607–614, oct 1996.

[92] J. E. Martin and R. A. Anderson, "Chain model of electrorheology," *J. Chem. Phys.*, vol. 104, p. 4814, jun 1998.

[93] M. Zimmer, X. Fan, J. Bao, R. Liang, B. Wang, C. Zhang, and J. Brooks, "Through-Thickness Thermal Conductivity Prediction Study on Nanocomposites and Multiscale Composites," *Mater. Sci. Appl.*, vol. 03, no. 03, pp. 131–138, 2012.

[94] K. Pietrak and T. S. Wiśniewski, "A review of models for effective thermal conductivity of composite materials," *Journal of Power Technologies*, vol. 95, no. 1, pp. 14–24, 2014.

[95] J. Shen and A. Mandelis, "Thermal-wave resonator cavity," *Rev. Sci. Instrum.*, vol. 66, no. 10, pp. 4999–5005, 1995.

[96] J. Shen, "Pyroelectric Thermal-Wave Resonant Cavity: A Precision Thermal Diffusivity Sensor for Gases and Vapors," *Int. J. Thermophys.*, vol. 19, no. 2, 1998.

[97] A. Mandelis, *Diffusion-Wave Fields*. New York, NY: Springer New York, 2001.

[98] R. Medina-Esquivel, J. M. Yáñez-Limón, and J. J. Alvarado-Gil, "Photothermal measurement of thermal diffusivity in carbonyl iron powder suspensions," *Eur. Phys. J. Spec. Top.*, vol. 153, pp. 75–77, jan 2008.

[99] P. Martínez-Torres, M. Zambrano-Arjona, G. Aguilar, and J. J. Alvarado-Gil, "Optical and thermal analysis of the time evolution of curing in resins by photothermal techniques," *Int. J. Thermophys.*, vol. 33, pp. 1892–1900, nov 2012.

[100] R. F. Brooks, A. T. Dinsdale, and P. N. Quested, "The measurement of viscosity of alloys—a review of methods, data and models," *Meas. Sci. Technol.*, vol. 16, pp. 354–362, feb 2005.

[101] W. Beens and W. de Jeu, "Flow-measurements of the viscosity coefficients of two nematic liquid crystalline azoxybenzenes," *J. Phys.*, vol. 44, pp. 129–136, feb 1983.

[102] D. J. Klingenberg, J. C. Ulicny, and M. A. Golden, "Mason numbers for magnetorheology," *J. Rheol. (N. Y. N. Y).*, vol. 51, pp. 883–893, sep 2007.

[103] H. Cheng, Y. Yeung, and H. Tong, "Viscosity behavior of magnetic suspensions in fluid-assisted finishing," *Prog. Nat. Sci.*, vol. 18, pp. 91–96, jan 2008.

[104] M. T. López-López, J. D. Durán, Á. V. Delgado, and F. González-Caballero, "Scaling between viscosity and hydrodynamic/magnetic forces in magnetic fluids," *Croatica Chemica Acta*, vol. 80, no. 3-4, pp. 445–451, 2007.

[105] K.-Q. Xia and S.-Q. Zhou, "Temperature power spectra and the viscous boundary layer in thermal turbulence: the role of Prandtl number," *Phys. A Stat. Mech. its Appl.*, vol. 288, pp. 308–314, dec 2000.

[106] J. R. Booker, "Thermal convection with strongly temperature-dependent viscosity," *J. Fluid Mech.*, vol. 76, p. 741, aug 1976.

[107] M. Hassan, M. Pathak, and M. K. Khan, "Rayleigh–Benard convection in Herschel–Bulkley fluid," *J. Nonnewton. Fluid Mech.*, vol. 226, pp. 32–45, dec 2015.

[108] A. Ghaffari, S. H. Hashemabadi, and M. Ashtiani, "A review on the simulation and modeling of magnetorheological fluids," *J. Intell. Mater. Syst. Struct.*, vol. 26, pp. 881–904, may 2015.

[109] Y. Ding, H. Alias, D. Wen, and R. A. Williams, "Heat transfer of aqueous suspensions of carbon nanotubes (CNT nanofluids)," *Int. J. Heat Mass Transf.*, vol. 49, pp. 240–250, Jan. 2006.

[110] Z. L. Wang, D. W. Tang, S. Liu, X. H. Zheng, and N. Araki, "Thermal-Conductivity and Thermal-Diffusivity Measurements of Nanofluids by 3ω Method and Mechanism Analysis of Heat Transport," *Int. J. Thermophys.*, vol. 28, pp. 1255–1268, Sept. 2007.

[111] B. Abad, D.-A. Borca-Tasciuc, and M. Martin-Gonzalez, "Non-contact methods for thermal properties measurement," *Renewable and Sustainable Energy Reviews*, vol. 76, pp. 1348–1370, 2017.

[112] C. Vales-Pinzon, A. Vega-Flick, N. W. Pech-May, J. J. Alvarado-Gil, R. A. Medina-Esquivel, M. A. Zambrano-Arjona, and J. A. Mendez-Gamboa, "Increasing the thermal conductivity of silicone based fluids using carbon nanofibers," *J. Appl. Phys.*, vol. 120, p. 205109, Nov. 2016.

[113] B. Azmi, M. Noroozi, Z. Rizwan, Z. Sulaiman, Z. Wahab, and M. Moksin, "Simple TWRC technique by using optical fiber," *Infrared Physics & Technology*, vol. 51, no. 3, pp. 270–275, 2008.

[114] D. Dadarlat, C. Neamtu, E. Surducan, A. H. Sahraoui, S. Longuemart, and D. Bicanic, "Accurate Photopyroelectric Measurements of Thermal Diffusivity of (semi)liquids," *Instrumen. Sci. Technol.*, vol. 30, pp. 387–396, Jan. 2002.

[115] J. A. P. Lima, E. Marín, O. Correa, M. G. d. Silva, S. L. Cardoso, C. Gatts, C. E. Rezende, H. Vargas, and L. C. M. Miranda, "Measurement of the thermal properties of liquids using a thermal wave interferometer," *Meas. Sci. Technol.*, vol. 11, no. 10, p. 1522, 2000.

[116] S. M. S. Murshed, K. C. Leong, and C. Yang, "Determination of the effective thermal diffusivity of nanofluids by the double hot-wire technique," *J. Phys. D: Appl. Phys.*, vol. 39, no. 24, p. 5316, 2006.

[117] B. Remy and A. Degiovanni, "Parameters estimation and measurement of thermophysical properties of liquids," *Int. J. Heat Mass Transf.*, vol. 48, pp. 4103–4120, Sept. 2005.

[118] A. Schmidt, M. Chiesa, X. Chen, and G. Chen, "An optical pump-probe technique for measuring the thermal conductivity of liquids," *Rev. Sci. Instrum.*, vol. 79, p. 064902, June 2008.

[119] Y. Tada, M. Harada, M. Tanigaki, and W. Eguchi, "Laser flash method for measuring thermal conductivity of liquids-application to low thermal conductivity liquids," *Rev. Sci. Instrum.*, vol. 49, pp. 1305–1314, Sept. 1978.

[120] D. Dadarlat and M. N. Pop, "Self-consistent photopyroelectric calorimetry for liquids," *Int. J. Therm. Sci.*, vol. 56, pp. 19–22, June 2012.

[121] E. Marín, A. García, G. Juárez, J. Bermejo-Arenas, A. Calderón, R. Ivanov, and A. Cruz-Orea, "On the heating modulation frequency dependence of the photopyroelectric signal in experiments for liquid thermal characterization," *Infrared Physics & Technology*, vol. 54, no. 6, pp. 449–453, 2011.

[122] W. J. Parker, R. J. Jenkins, C. P. Butler, and G. L. Abbott, "Flash Method of Determining Thermal Diffusivity, Heat Capacity, and Thermal Conductivity," *J. Appl. Phys.*, vol. 32, pp. 1679–1684, Sept. 1961.

[123] R. Coquard and B. Panel, "Adaptation of the FLASH method to the measurement of the thermal conductivity of liquids or pasty materials," *Int. J. Therm. Sci.*, vol. 48, pp. 747–760, Apr. 2009.

[124] D. L. Balageas, "Thermal diffusivity measurement by pulsed methods," *High Temp.-High Press.*, vol. 21, pp. 85–96, 1989.

[125] X. Zhou and H. Lin, *Local Sensitivity Analysis*. Cham: Springer International Publishing, 2017.

[126] J. Abate and W. Whitt, "A Unified Framework for Numerically Inverting Laplace Transforms," *INFORMS J. Comput.*, vol. 18, pp. 408–421, Nov. 2006.

[127] A. Salazar, A. Mendioroz, E. Apinaniz, C. Pradere, F. Noël, and J.-C. Batsale, "Extending the flash method to measure the thermal diffusivity of semitransparent solids," *Meas. Sci. Technol.*, vol. 25, p. 035604, Mar. 2014.

[128] N. W. Pech-May, A. Cifuentes, A. Mendioroz, A. Oleaga, and A. Salazar, "Simultaneous measurement of thermal diffusivity and effusivity of solids using the flash technique in the front-face configuration," *Meas. Sci. Technol.*, vol. 26, p. 085017, Aug. 2015.

[129] J. V. Beck and K. J. Arnold, *Parameter Estimation in Engineering and Science*. John Wiley & Sons, 1977.

[130] W. Minkina and S. Dudzik, *Infrared Thermography: Errors and Uncertainties*. United Kingdom: John Wiley & Sons, 2009.

[131] E. Apinaniz, A. Mendioroz, N. Madariaga, A. Oleaga, R. Celorrio, and A. Salazar, "Thermal characterization of rods, tubes and spheres using pulsed infrared thermography," *J. Phys. D: Appl. Phys.*, vol. 41, no. 1, p. 015403, 2008.

[132] K. Levenberg, "A Method for the Solution of Certain Non-Linear Problems in Least Squares," *Quart. Appl. Math.*, vol. 2, no. 2, pp. 164–168, 1944.

[133] D. W. Marquardt, "An Algorithm for Least-Squares Estimation of Nonlinear Parameters," *J. Soc. Ind. Appl. Math.*, vol. 11, pp. 431–441, June 1963.

[134] L. M. Cervantes-Espinosa, F. d. L. Castillo-Alvarado, G. Lara-Hernández, A. Cruz-Orea, J. G. Mendoza-Alvarez, J. P. Valcárcel, and A. García-Quiroz, "Thermal Characterization, Using the Photopyroelectric Technique, of Liquids Used in the Automobile Industry," *Int. J. Thermophys.*, vol. 33, pp. 1916–1923, Nov. 2012.

[135] M. Kaviany, *Essentials of Heat Transfer: Principles, Materials, and Applications*. Cambridge University Press, Aug. 2011.

[136] D. Dadarlat, H. Visser, and D. Bicanic, "An improved inverse photopyroelectric cell for measurement of thermal effusivity: application to fatty acids and triglycerides," *Meas. Sci. Technol.*, vol. 6, no. 8, p. 1215, 1995.

[137] D. Bicanic, M. Chirtoc, I. Chirtoc, B. v. Veldhuizen, J. P. Favier, and P. Helander, "New Technique for Measuring Absorption Coefficients of Strongly Absorbing Liquids: Optothermal Study of Sunflower Oil, Oleic Acid and its Chloroform Solutions at 3.39 Microns," *Spectros. Lett.*, vol. 28, pp. 101–110, Jan. 1995.

[138] D. Dadarlat, J. Gibkes, D. Bicanic, and A. Pasca, "Photopyroelectric (PPE) measurement of thermal parameters in food products," *J. Food Eng.*, vol. 30, no. 1-2, pp. 155–162, 1996.

[139] P. Bevington and D. K. Robinson, *Data Reduction and Error Analysis for the Physical Sciences*. New York: McGraw-Hill Higher Education, 3 ed., 2002.

[140] Clerc, J.P., Giraud, G., Roussenq, J., Blanc, R., Carton, J. P., Guyon, E., Ottavi, H., and Stauffer, D., "La percolation - modèles, simulations analogiques et numériques," *Ann. Phys.*, vol. 8, pp. 3–105, 1983.

[141] B. Vigolo, C. Coulon, M. Maugey, C. Zakri, and P. Poulin, "An experimental approach to the percolation of sticky nanotubes," *Science*, vol. 309, no. 5736, pp. 920–923, 2005.

[142] F. Kargar, Z. Barani, R. Salgado, B. Debnath, J. S. Lewis, E. Aytan, R. K. Lake, and A. A. Balandin, "Thermal Percolation Threshold and Thermal Properties of Composites with High Loading of Graphene and Boron Nitride Fillers," *ACS Appl. Mater. Interfaces*, vol. 10, pp. 37555–37565, oct 2018.

[143] R. Yin, Y. Zhang, W. Zhao, X. Huang, X. Li, and L. Qian, "Graphene platelets/aluminium nitride metacomposites with double percolation property of thermal and electrical conductivity," *J. Eur. Ceram. Soc.*, vol. 38, no. 14, pp. 4701–4706, 2018.

[144] B. W. Kim, S. Pfeifer, S. H. Park, and P. R. Bandaru, "The experimental determination of the onset of electrical and thermal conductivity percolation thresholds in carbon nanotube-polymer composites," *Mater. Res. Soc. Symp. Proc.*, vol. 1312, pp. 281–286, 2011.

[145] S. Y. Kwon, I. M. Kwon, Y.-G. , S. Lee, and Y.-S. Seo, "A large increase in the thermal conductivity of carbon nanotube/polymer composites produced by percolation phenomena," *Carbon N. Y.*, vol. 55, pp. 285–290, apr 2013.

[146] K. Sun, Z. D. Zhang, L. Qian, F. Dang, X. H. Zhang, and R. H. Fan, "Dual percolation behaviors of electrical and thermal conductivity in metal-ceramic composites," *Appl. Phys. Lett.*, vol. 108, p. 061903, feb 2016.

[147] N. Shenogina, S. Shenogin, L. Xue, and P. Keblinski, "On the lack of thermal percolation in carbon nanotube composites," *Appl. Phys. Lett.*, vol. 87, no. 13, pp. 1–3, 2005.

[148] M. J. Biercuk, M. C. Llaguno, M. Radosavljevic, J. K. Hyun, A. T. Johnson, and J. E. Fischer, "Carbon nanotube composites for thermal management," *Appl. Phys. Lett.*, vol. 80, pp. 2767–2769, apr 2002.

[149] I. Balberg, C. H. Anderson, S. Alexander, and N. Wagner, "Excluded volume and its relation to the onset of percolation," *Phys. Rev. B*, vol. 30, pp. 3933–3943, oct 1984.

[150] B. W. Kim, S. H. Park, R. S. Kapadia, and P. R. Bandaru, "Evidence of percolation related power law behavior in the thermal conductivity of nanotube/polymer composites," *Appl. Phys. Lett.*, vol. 102, no. 24, p. 243105, 2013.

[151] J. Abate and W. Whitt, "A unified framework for numerically inverting laplace transforms," *Informs. J. Comput.*, vol. 18, no. 4, pp. 408–421, 2006.

[152] N. M. Sofian, M. Rusu, R. Neagu, and E. Neagu, "Metal powder-filled polyethylene composites. V. Thermal properties," *J. Thermoplast. Compos.*, vol. 14, pp. 20–33, aug 2001.

[153] M. Rusu, N. Sofian, D. Rusu, E. Neagu, and R. Neagu, "Properties of Iron Powder Filled High Density Polyethylene," *J. Polym. Eng.*, vol. 21, no. 5, pp. 469–487, 2001.

[154] N. W. Pech-May, C. Vales-Pinzon, A. Vega-Flick, A. Oleaga, A. Salazar, J. M. Yanez-Limon, and J. J. Alvarado-Gil, "Heat transport in epoxy and polyester carbonyl iron microcomposites: The effect of concentration and temperature," *J. Compos. Mater.*, vol. 52, pp. 1331–1338, aug 2018.

[155] G. Zhang, Y. Xia, H. Wang, Y. Tao, G. Tao, S. Tu, and H. Wu, "A Percolation Model of Thermal Conductivity for Filled Polymer Composites," *J. Compos. Mater.*, vol. 44, pp. 963–970, apr 2010.

[156] Z. Elimat, F. Al-Aqrabawi, T. A. Hazeem, Y. Ramadin, and A. Zihlif, "Effect of Iron Particle Size and Concentration on Thermal Conductivity of Iron/Polystyrene Composites," *Int. J. Thermophys.*, vol. 34, pp. 2009–2018, 2013.

[157] A. Boudenne, L. Ibos, M. Fois, E. Gehin, and J. C. Majeste, "Thermophysical properties of polypropylene/aluminum composites," *J. Polym. Sci. Pol. Phys.*, vol. 42, no. 4, pp. 722–732, 2004.

[158] M. Rahaman, A. Aldalbahi, P. Govindasami, N. Khanam, S. Bhandari, P. Feng, and T. Altalhi, "A New Insight in Determining the Percolation Threshold of Electrical Conductivity for Extrinsically Conducting Polymer Composites through Different Sigmoidal Models," *Polymers*, vol. 9, p. 527, oct 2017.

[159] A. Merzouki and N. Haddaoui, "Electrical Conductivity Modeling of Polypropylene Composites Filled with Carbon Black and Acetylene Black," *ISRN Polym. Sci.*, vol. 2012, pp. 1–7, 2012.

[160] J. Vilcakova, P. Saha, and O. Quadrat, "Electrical conductivity of carbon fibres/polyester resin composites in the percolation threshold region," *Eur. Polym. J.*, vol. 38, no. 12, pp. 2343–2347, 2002.

[161] K. Yaman and Ö. Taga, "Thermal and Electrical Conductivity of Unsaturated Polyester Resin Filled with Copper Filler Composites," *Int. J. Polym. Sci.*, vol. 2018, pp. 1–10, 2018.

[162] W. B. Genetti, W. L. Yuan, B. P. Grady, E. A. O'Rear, C. L. Lai, and D. T. Glatzhofer, "Polymer matrix composites: Conductivity enhancement through polypyrrole coating of nickel flake," *J. Mater. Sci.*, vol. 33, no. 12, pp. 3085–3093, 1998.

[163] A. J. Marsden, D. G. Papageorgiou, C. Vallés, A. Liscio, V. Palermo, M. A. Bissett, R. J. Young, and I. A. Kinloch, "Electrical percolation in graphene–polymer composites," *2D Materials*, vol. 5, p. 032003, jun 2018.

[164] G. Chen, *Nanoscale energy transport and conversion: a parallel treatment of electrons, molecules, phonons, and photons*. Oxford University Press, 2005.

[165] R. D. Sherman, L. M. Middleman, and S. M. Jacobs, "Electron transport processes in conductor-filled polymers," *Polym. Eng. Sci.*, vol. 23, no. 1, pp. 36–46, 1983.

[166] W. M. Albers, M. Karttunen, L. Wikström, and T. Vilkman, "Effects of compression and filler particle coating on the electrical conductivity of thermoplastic elastomer composites," *J. Electron. Mater.*, vol. 42, no. 10, pp. 2983–2989, 2013.

[167] Y. D. Shi, J. Li, Y. J. Tan, Y. F. Chen, and M. Wang, "Percolation behavior of electromagnetic interference shielding in polymer/multi-walled carbon nanotube nanocomposites," *Compos. Sci. Technol.*, vol. 170, no. November 2018, pp. 70–76, 2019.

[168] A. Mandelis, J. Vanniasinkam, S. Budhudu, A. Othonos, and M. Kokta, "Absolute nonradiative energy-conversion-efficiency spectra in Ti:A1203 crystals measured by noncontact quadrature photopyroelectric spectroscopy," *Phys. Rev. B*, vol. 48, no. 10, 1993.

[169] J. G. Webster, *The measurement, instrumentation and sensors handbook*. CRC press, 1998.

[170] A. Rosencwaig and A. Gersho, "Theory of the photoacoustic effect with solids," *Journal of Applied Physics*, vol. 47, no. 1, pp. 64–69, 2008.

[171] E. Putley, "The Pyroelectric Detector," *Semicond. Semimetals*, vol. 5, p. 264, 1970.

[172] D. Maillet, S. André, J. C. Batsale, A. Degiovanni, and C. Moyne, *Thermal quadrupoles: solving the heat equation through integral transforms*. Chichester; New York: Wiley, 2000.